Biochemical and Structural Studies on Amyloid Aggregation in C. elegans

Sarah Townend

Submitted in accordance with the requirements for the degree of Doctor of Philosophy

The University of Leeds

School of Molecular & Cellular Biology

October 2023

The candidate confirms that the work submitted is their own, except where work which has formed part of jointly authored publications has been included. The contribution of the candidate and the other authors to this work has been explicitly indicated below. The candidate confirms that appropriate credit has been given within the thesis where reference has been made to the work of others.

Some of the work shown in **Chapter 5** of the thesis has appeared in publication as follows: Miles J, Townend S, Milonaitytė D, Smith W, Hodge F, Westhead DR, and van Oosten-Hawle P (2023) Transcellular chaperone signalling is an intercellular stress-response distinct from the HSF-1–mediated heat shock response. *PLoS Biol* 21(2): e3001605. https://doi.org/10.1371/journal.pbio.3001605.

My contribution to this work was to perform thermotolerance assays, and qPCR of *hsp-70* mRNA and associated data analysis in the hsp-90int hp-RNAi strain. Jay Miles contributed the tissue-specific RNAi screen and related bioinformatics and data analysis of the hsp-90int hp-RNAi strain. Patricija van Oosten-Hawle, Jay Miles, and I worked collaboratively on the writing, reviewing, and editing the article.

Acknowledgements

I would like to thank the Medical Research Council for funding this research in the form of a Discovery Medicine North (DiMeN) Doctoral Training Programme scholarship, and Dr Emily Goodall as the DiMeN DTP co-ordinator. I would also like to thank Professor Janine Kirstein (University of Bremen, Germany) for kindly gifting the JMK $A\beta_{1-42}$, JMK control, and HPS-90::GFP *C. elegans* strains.

I would like to thank my supervisor Professor Neil Ranson for his guidance and encouragement throughout this project which helped to develop my research and wider skills. Over the course of the past four years, I have been fortunate to have his supervision, and I am incredibly thankful for it.

To my fellow *C. elegans* researchers, for providing scientific insights, motivation, and friendship especially in the final year of this project. I would particularly like to thank Sarah Good for teaching me everything *C. elegans*, and Francesca Hodge, for her enduring words of support, insightful fun facts, and the ability to make even the most challenging days enjoyable. Thanks also to the other members of Garstang Level 9, especially Anya Mottram, with whom a 'quick chat' always lasted an hour and brightened my day. To the members of the EM facility, especially Maddie Gilbert, Dr Yehuda Haflon, and Dr Tom O'Sullivan. Tom continuously went above and beyond in supporting me and this project, without him this project would not have been possible, and I would likely have given up.

I'd also like to thank my incredible friends especially Annie Mellings, Laura Atkinson, Becky Wells, Maddy Knight and Mel Coxhead, for their unwavering

belief in me and supporting me during the good and the bad. To my parents who always reminded me that a PhD would not complete itself and encouraged me to focus on what was within my control. Finally, to Frankie, my best friend, for listening to me vent about worms for four consecutive years. I will forever cherish his support and patience during this journey.

Abstract

Organismal proteostasis is dependent on communication mechanisms such as stress responses. These multicellular organisms require intercellular stress responses which can act beyond the confines of individual cells to activate the proteostasis network (PN) across tissues to protect organismal health. One such mechanism is transcellular chaperone signalling (TCS). When proteostasis is compromised, misfolded proteins can accumulate, giving rise to detrimental conditions such as Alzheimer's disease, characterized by the aggregation of extracellular $A\beta_{1-42}$ plaques in the human brain.

TCS can be triggered by the tissue-specific over-expression or depletion of HSP-90, which in turn activates distinct cell-non-autonomous signalling pathways. These pathways are instrumental in safeguarding entire organisms, such as the model organism *C. elegans*. The means by which this tissue-to-tissue communication enhances systemic chaperone expression and its potential to defend organisms against protein misfolding diseases remain unresolved questions.

To shed light on this, *C. elegans* were used to investigate the mechanisms by which HSP-90 over-expression or depletion initiates TCS. This research revealed that over-expressing HSP-90 induces inter-tissue signalling from the intestine to neurons, thereby protecting against $A\beta_{1-42}$ aggregation. Conversely, HSP-90 depletion in the intestine triggers TCS signalling to muscle cells, leading to the activation of HSP-70 expression, and aiding in TCS-mediated heat stress resistance and lifespan extension. The pathway identified highlights the role of

TXT-1 and CEH-58, a PDZ-domain guanylate cyclase and a homeobox transcription factor respectively, as peptides which stimulate extracellular peptides TXT-4 and TXT-8 to serve as trans-tissue signals to increase the HSP-90 levels in distal tissues.

To further explore $A\beta_{1-42}$ aggregation in *C. elegans*, a workflow was developed to elucidate the in-tissue architecture of $A\beta_{1-42}$ fibrils. This was achieved using advanced techniques such as cryogenic correlative light electron microscopy (cryo-CLEM) and cryogenic electron tomography (cryo-ET). Ultra-thin cryo-sections of adult *C. elegans* tissue were collected on cryo-EM grids, and cryo-CLEM was employed to accurately map the location of $A\beta_{1-42}$ fibrils, providing precise guidance for the collection of cryo-ET data. The resulting 3D reconstructions unveiled the macromolecular features of adult *C. elegans* tissue and offered insights into the molecular architecture of $A\beta_{1-42}$ fibrils. These fibrils were found to be organized into parallel bundles, in proximity to ribosomes and microtubules.

Table of Contents

CHAPTER 1. INTRODUCTION **17**

1.1 Protein Folding and Misfolding 17

1.2 Proteostasis 19

1.3 Molecular Chaperones 20

1.3.1 The HSP90 Family *21*

1.4 Cell Autonomous Stress Responses 23

1.4.1 Heat Shock Response *23*

1.4.2 The Unfolded Protein Response of the Endoplasmic Reticulum (UPR^{ER}) *25*

1.4.3 Unfolded Protein Response of the Mitochondria (UPR^{mito}) *28*

1.4.4 Transcellular Chaperone Signalling *29*

1.5 Amyloid 30

1.6 Alzheimer's Disease 33

1.6.1 The Social Impact of Alzheimer's Disease *33*

1.6.2 Alzheimer's Disease Aβ Pathology *34*

1.7 The Potential of Caenorhabditis elegans (C. elegans) 37

1.7.1 The History of C. elegans *38*

1.7.2 The Morphology of C. elegans *38*

1.7.3 The Lifecycle of C. elegans *40*

1.7.4 The Advantages and Disadvantages of the C. elegans model *41*

1.7.5 C. elegans as a model for Alzheimer's Disease *44*

1.8 Methods of Characterising Protein Structure 47

1.8.1 Advances in Microscopy *49*

1.8.2 An Introduction to CryoEM *50*

1.8.3 Methods in Cryo-ET *52*

1.8.4 The structure of Aβ *53*

CHAPTER 2. MATERIALS AND GENERAL METHODS **57**

2.1 PREPARATION OF NGM, NGM-FUDR, AND NGM-RNAI AGAR PLATES 57
2.1.1 Preparation and Seeding of Bacterial Cultures *58*
2.1.2 Preparation of liquid culture *59*
2.2 *C. ELEGANS* STRAINS AND MAINTENANCE 60
2.2.1 C. elegans Strains and Genotypes *60*
2.2.2 Strain Maintenance and Storage *64*
2.2.3 Population Synchronisation and Aging *65*
2.2.4 Crossing Strains and Generating Males *67*
2.2.5 Avoiding Cryptic Mutations *68*
CHAPTER 3. TRANSCELLULAR CHAPERONE SIGNALLING REGULATES ORGANISMAL PROTEOSTASIS AND PROTECTS AGAINST AB1-42 PROTEIN TOXICITY IN MUSCLE AND NEURONES 69
3.1 INTRODUCTION 69
3.1.1 Proteostasis and Amyloid in C. elegans *69*
3.1.2 TCS Activated by Tissue-Specific HSP-90 Over-expression *71*
3.2 Overview of Aims *74*
3.2 MATERIALS AND METHODS 75
3.2.1 Motility Assays *75*
3.2.2 Chemotaxis Assay *76*
3.2.4 Offspring Assay *77*
3.2.3 Lifespan Assay *77*
3.2.5 X-34 Staining and Confocal Microscopy *78*
3.2.6 C. elegans strains and genotypes *75*
3.3 RESULTS 78
3.3.1 Untagged Amyloid Aggregation *79*
3.3.2 Tagged Amyloid Aggregation *85*
3.4 DISCUSSION 98
3.4.1 Temperature Permissive Strains *98*
3.4.2 The Challenges of Staining C. elegans tissues *99*

3.4.3 Intracellular or Extracellular Aβ1-42 Aggregation *99*

3.4.4 Mechanisms of HSP-90 Over-expression Induced TCS *101*

CHAPTER 4. NATIVE IN-TISSUE STRUCTURES OF AMYLOID-B IN A *C. ELEGANS* MODEL OF AD BY CRYO-ET **105**

4.1 INTRODUCTION 105

4.2 METHODOLOGY 110

4.2.1 High Pressure Freezing *110*

4.2.2 Cryo-Sectioning *111*

4.2.3 Cryogenic Fluorescent Microscopy *113*

4.2.5 Cryo-Tomography Data Collection and Reconstruction *115*

4.2.6 Amyloid purification from C. elegans *114*

4.2.8 C. elegans strains and genotypes *115*

4.3 RESULTS 115

4.3.1 Optimising High Pressure Freezing C. elegans *115*

4.3.2 Optimising Carrier and Grid cryo-fluorescent screening *119*

4.3.3 Optimising Cryo-Sectioning *123*

4.3.5 In situ Tomography of the Adult MAβ1-42 C. elegans Model *128*

4.4 DISCUSSION 131

4.4.1 CEMOVIS Method Development *131*

4.4.2 Qualitative Tomogram Assessments *135*

CHAPTER 5. TCS IS AN INTERCELLULAR STRESS-RESPONSE DISTINCT FROM THE HSF-1-MEDIATED HSR **137**

5.1 INTRODUCTION 137

5.1.1 HSP70 ..... *137*

5.1.2 Systemic and Tissue-Specific HSP-90 Depletion *138*

5.1.3 TCS activated by Tissue-Specific hsp-90 Knock Down *140*

5.2 METHODS 141

5.2.1 hsp-90 Knock Down C. elegans Strains Maintenance *141*

5.2.2 Gene Knock Down by RNAi *142*

5.2.3 Thermotolerance Assay *143*

5.2.4 RNA Extraction, cDNA Synthesis, and quantitative PCR (qPCR) *143*

5.2.5 Primers Used for qPCR *144*

5.2.6 C. elegans Strains and Genotypes *145*

5.3 RESULTS 145

5.3.1 HSP-90 Knock Down Induces TCS-mediated hsp-70 upregulation *145*

5.3.2 TCS is not Dependent on HSF-1 ..... *147*

5.3.3 txt-1 is required for TCS-mediated hsp-70 ..... *149*

5.3.4 Extracellular Peptides are Involved in TCS Signalling *153*

5.4 DISCUSSION 158

FINAL DISCUSSION 164

REFERENCES 170

List of Figures

Figure 1	The Protein Folding Funnel Hypothesis.
Figure 2	Schematic of the ATPase cycle of HSP-90.
Figure 3	The Heat Shock Response
Figure 4	The Unfolded Protein Response of the ER (UPR^{ER}).
Figure 5	The Unfolded Protein Response of the Mitochondria (UPR^{mito}).
Figure 6	The Amyloid Fibril Structure.
Figure 7	The Steric Zipper Interfaces Which Stabilise Amyloid Fibrils
Figure 8	Schematic of Amyloid Formation
Figure 9	The Tissues of *C. elegans*
Figure 10	The Life Cycle of *C. elegans*
Figure 11	Deposited $A\beta_{1-42}$ Fibril Structures.
Figure 12	PQM-1 Mediated TCS
Figure 13	The Experimental Set Up for Chemotaxis Assays.
Figure 14	Over-expressing HSP-90 in distal tissues is protective against $A\beta_{3-42}$ and $A\beta_{1-42}$ in the body wall muscle of *C. elegans*.
Figure 15	Over-expressing HSP-90 in the intestine initiates TCS to the neurones to protect against $A\beta_{1-42}$ toxicity.
Figure 17	The localisation of fluorescently tagged $A\beta_{1-42}$ in *C. elegans*
Figure 18	Over-expressing HSP-90 in the distal tissues of $MA\beta_{1-42}$ and $NA\beta_{1-42}$ animals ameliorates toxic $A\beta_{1-42}$ activity.
Figure 19	Over-expressing HSP-90 in the same or distal tissues as muscular Aβ1-42 improves organismal fitness.

Figure 20	Over-expressing HSP-90 in the same or distal tissues as neuronal Aβ$_{1-42}$ improves organismal fitness.
Figure 21	Over-expressing HSP-90 in the same or distal tissues rescues reduced fecundity in NAβ$_{1-42}$ and MAβ$_{1-42}$ animals.
Figure 22	Bagging in MAβ$_{1-42}$ Day 5 adults
Figure 23	Over-expressing HSP-90 in the same or distal tissues as neuronal Aβ$_{1-42}$ rescues chemotaxis impairment
Figure 24	Diagram of High Pressure Freezing Adult *C. elegans*
Figure 25	Schematic of a Sample Pyramid for CEMOVIS.
Figure 26	Diagram of Carrier and Grid Cryo-FM Screening for adult MAβ$_{1-42}$ *C. elegans*.
Figure 27	Adult *C. elegans* tissue devitrification during CEMOVIS.
Figure 28	High Pressure Frozen *C. elegans* Samples During the Optimisation Process
Figure 29	Reducing Frost Accumulation on CEMOVIS grids during cryo-FM screening
Figure 30	Alexa Fluor™ 647-labeled dextran used as a cryoprotectant for the CEMOVIS of adult MAβ$_{1-42}$ *C. elegans*.
Figure 31	Cryo-FM of MAβ$_{1-42}$ *C. elegans* at Day 10 of adulthood
Figure 32	Improving the quality of ribbons produced from adult *C. elegans* tissue.
Figure 33	Poor vs High Quality Tomograms
Figure 34	Tissue ribbons from different depth HPF carriers
Figure 35	Tomographic slice through a cryo-ET reconstruction of the cellular ultrastructure within adult *C. elegans*.

Figure 36	Tomographic slices through cryo-ET reconstruction of Aß$_{1-42}$ pathology within adult *C. elegans*.
Figure 37	TCS induces *hsp-70* cell-non-autonomously in muscle cells and increases lifespan and stress resistance
Figure 38	TCS-induced hsp-70 expression is regulated independently of *hsf-1*.
Figure 39	*txt-1* is required for TCS-mediated *hsp-70* induction during HS independent of HSF-1.
Figure 40	Extracellular peptides are involved in TCS signalling from the intestine to the muscle
Figure 41	A schematic outlining the suggested mechanism for opposing HSP-70 regulation by HSR or TCS
Figure 42	Potential convergence of opposing HSP-90 TCS pathways

List of Tables

Table 1	List of *C. elegans* strains used throughout this thesis and their corresponding genotypes.
Table 2	Quantifying the MAß$_{1-42}$ animal lifespan data.
Table 3	Quantifying the NAß$_{1-42}$ animal lifespan data.

Abbreviations

Aβ	Amyloid-ß
AD	Alzheimer's disease
ADP	Adenosine diphosphate

AFM	Atomic Force Microscopy
APOE	Apolipoprotein E
APP	Amyloid Precursor Protein
αSyn	α-Synuclein
ATP	Adenosine triphosphate
BiP	Binding immunoglobulin protein
Bwm	Body Wall Muscle
CAA	Cerebral Amyloid Angiopathy
CD	Circular Dichroism
C. elegans	Caenorhabditis elegans
CEMOVIS	Cryo-electron Microscopy of Vitreous Sections
CNS	Central Nervous System
CRYAB	αB-crystallin
cryo-CLEM	Cryogenic Correlative Light Electron Microscopy
cryo-EM	Cryogenic Electron Microscopy
cryo-ET	Cryogenic Electron Tomography
cryo-FM	Cryogenic Fluorescent Microscopy
EM	Electron Microscopy
eo-AD	Early Onset Alzheimer's Disease
ER	Endoplasmic Reticulum
ERSEs	ER stress elements
FIB	Focused Ion Beam
FIB-SEM	Focused Ion Beam Scanning Electron Microscopy
FUdR	Floxuridine
GFP	Green Fluorescent Protein
HPF	High Pressure Freezer

HSE	Heat Shock Elements
HSP	Heat Shock Protein
HSPs	Heat Shock Proteins
HSR	Heat Shock Response
Int	Intestine
L1	First stage larvae
L2	Second stage larvae
L3	Third stage larvae
L4	Fourth stage larvae
lo-AD	Late Onset Alzheimer's Disease
Neu	Neurone
NFT	Neurofibrillary Tangles
NGM	Nutrient Growth Medium
NMR	Nuclear Magnetic Resonance
PALM	Photo-activated localization microscopy
PCR	Polymerase chain reaction
PERK	Protein kinase-like ER kinase
PN	Proteostasis Network
polyQ	Polyglutamine
PSEN	Presenilin
qPCR	Quantitative PCR
RNAi	RNA interference
sHSPs	Small heat shock proteins
SNR	Signal to Noise Ratio
SPA	Single Particle Analysis
STED	Stimulated emission depletion microscopy

STORM	Stochastic optical reconstruction microscopy
TEM	Transmission Electron Microscopy
UPR	Unfolded Protein Response
UPR^{ER}	Unfolded Protein Response of the Endoplasmic Reticulum
UPR^{mito}	Unfolded Protein Response of the Mitochondria
WT	Wild-type

Chapter 1. Introduction

1.1 Protein Folding and Misfolding

Proteins are ubiquitous molecules present in all living organisms and play a role in almost every chemical process in the human body. Proteins are linear polymers that fold into a 3D shape known as a proteins structure. Structures are differentiated between each other from by a primary amino acid sequence. Amino acids are usually composed of a carbon and hydrogen atom, a carboxyl and amino group and a variable group. The variable group changes the characteristics of amino acids which can be grouped as positively charged, negatively charged, and hydrophobic and special cases. Proteins fold to bury hydrophobic residues inside the protein to form a hydrophobic core, wherein the hydrophobic variable groups are shielded from the water thus underpinning the final protein 3D structure (Dobson, 2004). The unique structure of a protein dictates function, thus reaching the correct structure is essential to delivering the multitude of functions required for cellular and organismal health. The early understanding of the protein folding hypothesis theorised that the amino acid sequence of a polypeptide chain is the only information required for correct protein folding. After it was shown that proteins can fold into their native states independent of assisting molecules and pathways (Anfinsen *et al.*, 1961).

On an intramolecular level the native, folded state of a protein is the most stable and accessible state, and to reach this point, proteins pass through several conformations stochastically via different pathways controlled by kinetic local interactions (Englander and Mayne, 2017). While many mechanisms have been

theorised, the protein folding funnel hypothesis is the most widely accepted (Figure 1) (Dobson, 2004).

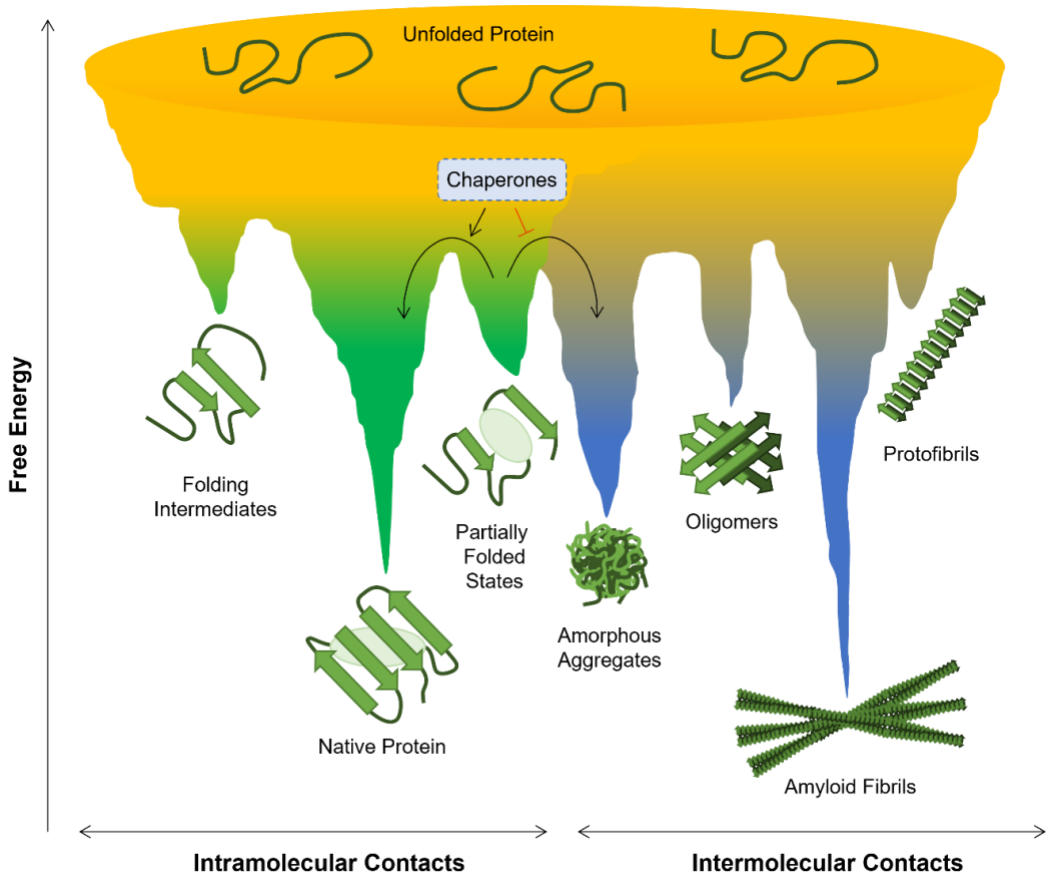

Figure 1. The Protein Folding Funnel Hypothesis. Schematic showing the funnel-shaped energy landscape theory of protein folding and aggregation. The intramolecular contacts within a protein (green), and the intramolecular contacts between proteins (blue) and the energy. The interplay of intermolecular interactions among partially folded states can lead to the formation of amorphous aggregates, oligomers, and amyloid fibrils. Chaperone proteins can assist in folding proteins in a partially folded state to a native state, and prevent the formation of amorphous aggregates by refolding misfolded proteins (Figure adapted from: Hartl, Bracher and Hayer-Hartl, 2011).

The model relates the Gibbs free energy concept to protein folding. Unfolded proteins traverse a funnel-shaped energy landscape where the unfolded protein in an unstable conformation travels down a free energy trajectory, losing conformational entropy, towards more stable lower energy conformations such as non-native intermediates and partially folded states (Englander and Mayne, 2017). Many proteins achieve their native states, however misfolding can occur when folding intermediates form intramolecular non-native interactions, or collapse into disorganised globular conformations (Hartl, Bracher and Hayer-Hartl, 2011). Misfolded protein can exhibit exposed hydrophobic residues increasing the propensity of the protein to aggregate into relatively stable amorphous aggregates and potentially amyloid fibrils (Eichner *et al.*, 2011).

1.2 Proteostasis

Mammalian cells express tens of thousands of proteins, the function of which is driven by their native folded states. Cells have evolved to develop a complex network of components to steer proteins to achieve and stay in their native conformation and maintain protein homeostasis (proteostasis). While proteins can fold spontaneously into their native states, research shows a group of proteins called chaperones can assist in the folding, refolding, unfolding, and assembly or disassembly of macromolecular structures (Hipp, Park and Hartl, 2014). The proteostasis network (PN) employs chaperones, their regulators, and machineries of proteolytic degradation to refold misfolded intermediates into the native states or degrade, or export misfolded protein from the cell to prevent the formation of amorphous aggregates and higher order fibrils (Figure 8) (Labbadia and Morimoto, 2015).

Aging or cellular stress can cause the cause the decline of organismal health and reduce the performance of the proteostasis network (López-Otín *et al.*, 2023). A non-functional PN is less effective at assisting in the assembly of macromolecules or preventing the build-up of misfolded proteins and aggregates. Left unfolded, proteins are unable to function causing a breakdown in cellular mechanisms and pathways (Hipp, Kasturi and Hartl, 2019). Furthermore, the accumulation of aggregates such as Amyloid-ß (Aß) and α-synuclein (αSyn) is linked to cytotoxicity and ultimately cell death linked to disease (Iadanza *et al.*, 2018), giving rise to the importance of studying maintenance of organismal health by regulating the PN.

1.3 Molecular Chaperones

Molecular chaperones are the central coordinators of the PN regulating protein folding and conformational maintenance. Chaperones are highly conserved across all kingdoms, highly conserved in eukaryotes ranging from simple microscopic yeast cells to complex multicellular organisms (Tittelmeier, Nachman and Nussbaum-Krammer, 2020). Chaperones or stress proteins are an umbrella term for a huge selection of proteins, the most common group being classified as heat-shock proteins (HSPs) (Dubey *et al.*, 2015). They are usually grouped into six 'families' by molecular weight, HSP-90, HSP-70, HSP-60, HSP-40, HSP-100 and small HSP (sHSPs) (Mogk, Kummer and Bukau, 2015). The HSP families play different roles in the PN, the chaperones HSP-70, HSP-90, and HSP-60 facilitate *de novo* folding/refolding by identifying exposed hydrophobic residues and acting through kinetic partitioning (Tyedmers, Mogk and Bukau, 2010). Chaperones often cooperate in multiple stress responses and pathways to

maintain proteostasis within individual cells and whole organisms (Nillegoda, Wentink and Bukau, 2018).

1.3.1 The HSP90 Family

The HSP-90 family functions to control signalling pathways in eukaryotic cells, including apoptosis, cell-cycle progression, mitotic signal transduction, innate immunity and protein degradation (van Oosten-Hawle, 2023). HSP-90 activity is driven by the hydrolysis of ATP at the N-terminal domain of the chaperone, to initiate a conformational cycle wherein the two N-terminal domains dimerise. The middle domains twist together, exposing a catalytic loop for client protein interaction. To separate, ATP is hydrolysed, and the N-terminal domains dissociate allowing the release of the reaction products and returning HSP-90 to an open conformation state (Figure 2) (Lackie *et al.*, 2017). Co-chaperones assist in this conformational cycle including AHA1 which stimulates ATP hydrolysis and HOP which inhibits N-terminal dimerization (Gaiser *et al.*, 2011). Normally, HSP-90 functions downstream of HSP-70 with co-chaperones which bind to the tetratricopeptide repeat domain of HSP-90 to facilitate conformational changes of macromolecules (Morán Luengo, Mayer and Rüdiger, 2019).

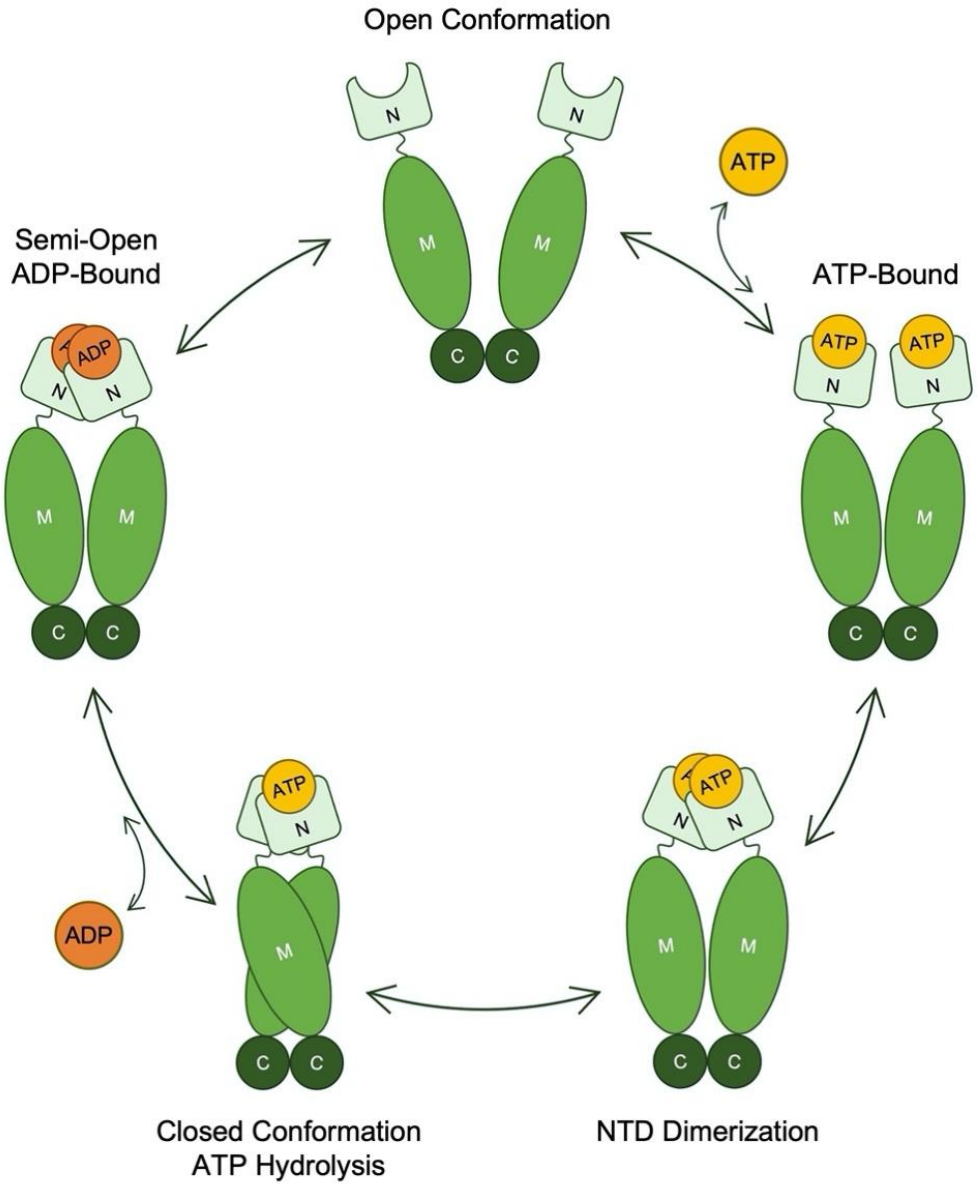

Figure 2. Schematic of the ATPase cycle of HSP-90. The HSP-90 assumes open conformation, until ATP binds to the ATPase domain at the N-terminal, initiating HSP-90 to undergo a conformational change where the N-terminal domains (N) dimerise. The middle domain (M) is employed for ATP hydrolysis, wherein HSP-90 is in a closed conformation Following ADP hydrolysis, the HSP-90 transitions into a semi-open intermediate state, while ADP is still bound. The release of ADP allows the N-terminal domains to dissociate, enabling the ATPase cycle to restart (Figure adapted from: Lackie *et al.*, 2017).

1.4 Cell Autonomous Stress Responses

1.4.1 Heat Shock Response

Temperature has a significant impact on protein structure and increasing an organism's internal temperature above optimal can result in protein misfolding (Frauenfelder, Sligar and Wolynes, 1991). While protein structure underpins function, misfolding can also expose hydrophobic residues, a prerequisite to aggregation and the breakdown of proteostasis (Chiti and Dobson, 2009). To counteract this, the heat shock response (HSR) upregulates chaperone expression at high temperatures, regulated under the transcription factor Heat Shock Factor 1 (HSF-1) (Figure 3) (Ritossa, 1962; Lindquist, 1986).

Under non-stress conditions, an HSF-1 monomer is sequestered within a chaperone complex containing HSP-90 (Satyal *et al.*, 1998). HSP-90 is thought to repress HSF-1 activity by binding directly to HSF-1, preventing its trimerisation (Shi, Mosser and Morimoto, 1998) and thus the DNA binding action of the transcription factor (Zou *et al.*, 1998). When temperatures increase beyond the optimal range, cells and organisms undergo heat stress or shock, the multi-chaperone complex dissociates allowing the chaperones to assist in protein refolding (Figure 3) (Ananthan, Goldberg and Voellmy, 1986).

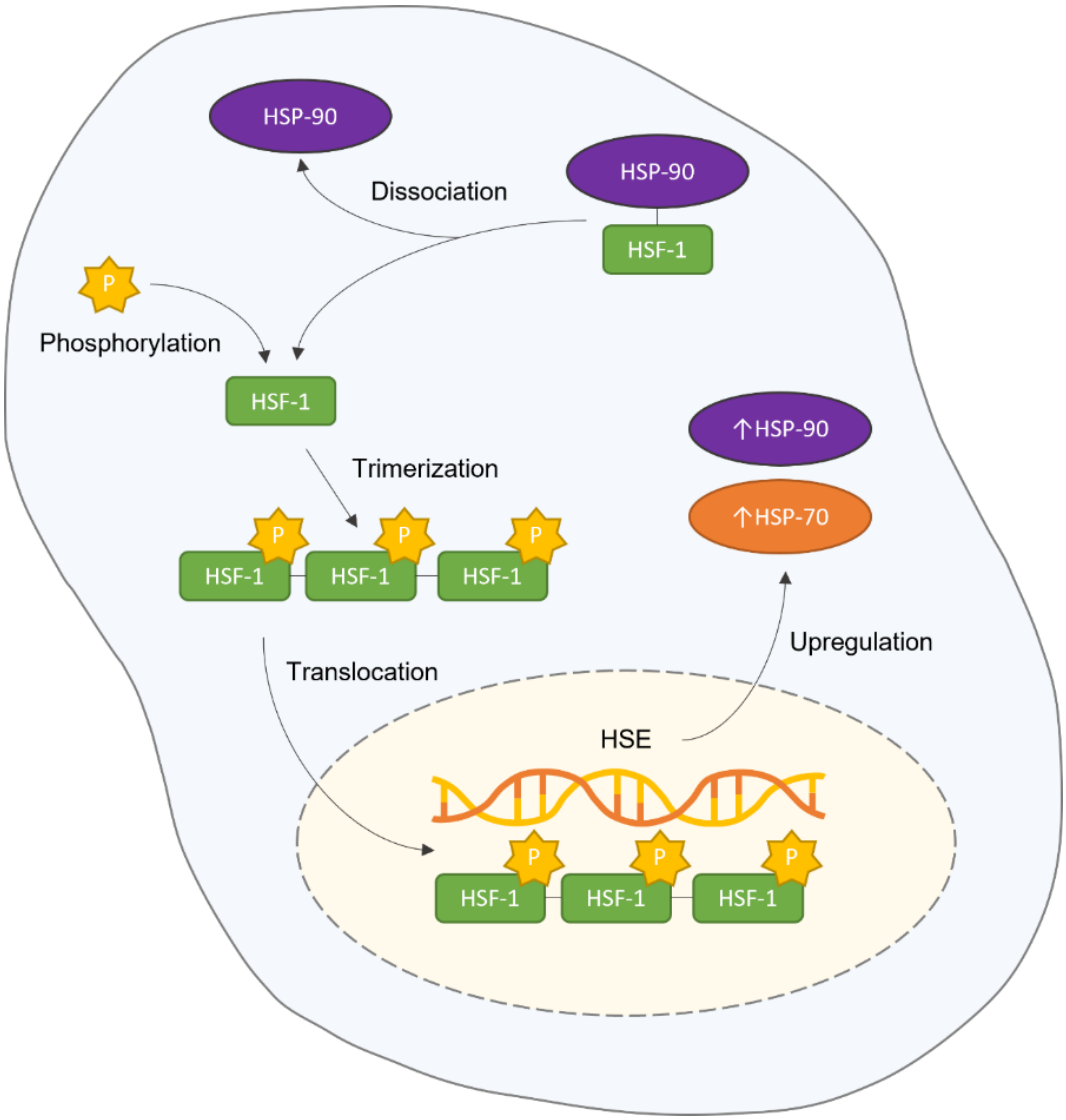

Figure 3. The Heat Shock Response. Under non-stress conditions, the transcription factor HSF-1 is localised in the cytosol, sequestered in a multi-chaperone complex with HSP-90. When misfolded proteins are present, HSP-90 dissociates from the complex to facilitate their refolding. Subsequently, HSF-1 undergoes trimerization, translocates to the nucleus, and associates with heat shock elements within the promoters of genes responsible for the heat shock response. This, in turn, stimulates the heightened expression of chaperones like HSP-70 (Figure adapted from: Le Breton and Mayer, 2016).

Heat stress can induce hyperphosphorylation of HSF-1 which sustains the activity of the transcription factor at increased temperature. Phosphorylation is not essential for HSF-1 activation and does not occur during acute heat shock (Xu *et al.*, 2012). With or without phosphorylation, release from the multi-chaperone complex enables HSF-1 to trimerise and become an active transcription factor. Once active, HSF-1 translocates to the nucleus, where it binds to heat shock elements (HSEs), highly conserved DNA sequences, in the heat shock response genes to upregulate heat shock protein expression (Lindquist, 1986). Upregulated expression of chaperones such as HSP-70 and HSP-90 and small HSPs assists in the refolding of proteins to regulate the proteostasis network (Figure 3) (Prodromou, 2016).

1.4.2 The Unfolded Protein Response of the Endoplasmic Reticulum (UPR^{ER})

The rough endoplasmic reticulum (ER) is studded with ribosomes and is the site of protein processing and quality control for proteins that possess a signal sequence and thus are destined to either reside within the secretory pathway or be secreted. Prior to entering the secretory pathway, these proteins undergo co-translational translocation into the ER for chaperone-assisted folding. The ER has a folding capacity, which once surpassed causes stress that activates the unfolded protein response of the ER (UPR^{ER}), simultaneously causing the upregulation of ER chaperones and suppression of protein synthesis (Read and Schröder, 2021). Under non-stressful conditions the ER resident HSP-70 family chaperone BiP is bound to the ER luminal domains of three transmembrane proteins PEK-1, IRE-1, and AFT-6 (Taylor, 2016). During ER stress, BiP

dissociates from the effector proteins to assist in protein refolding, resulting in the three key complimentary pathways of the UPR^{ER} response (Figure 4) (Schröder and Kaufman, 2005; Hetz and Papa, 2018).

The kinase PEK-1 becomes active following trans-autophosphorylation and phosphorylates and consequently inhibits the translation initiation factor eIF2a. The global translation of proteins is thus inhibited, reducing the workload of chaperone proteins (Harding *et al.*, 2000). Like PEK-1, the endonuclease and kinase IRE-1 becomes active through trans-autophosphorylation to mediate cytoplasmic alternative splicing of *xbp-1* mRNA to *xbp-1s*, which is translated to produce the active transcription factor XBP-1s (Sidrauski and Walter, 1997). Once active, XBP-1s translocates to the nucleus, where it binds to the UPR element (UPRE) of UPR^{ER} target genes to upregulate chaperones such as BiP to increase the ER folding capacity (Yamamoto *et al.*, 2005). Finally, upon dissociation of BiP, ATF-6 translocates to the Golgi body and cleaved to produce the active transcription factor ATF-6f, which binds to ER stress elements (ERSEs) of stress response genes upregulating the expression of chaperones such as BiP and XBP-1 (Figure 4).

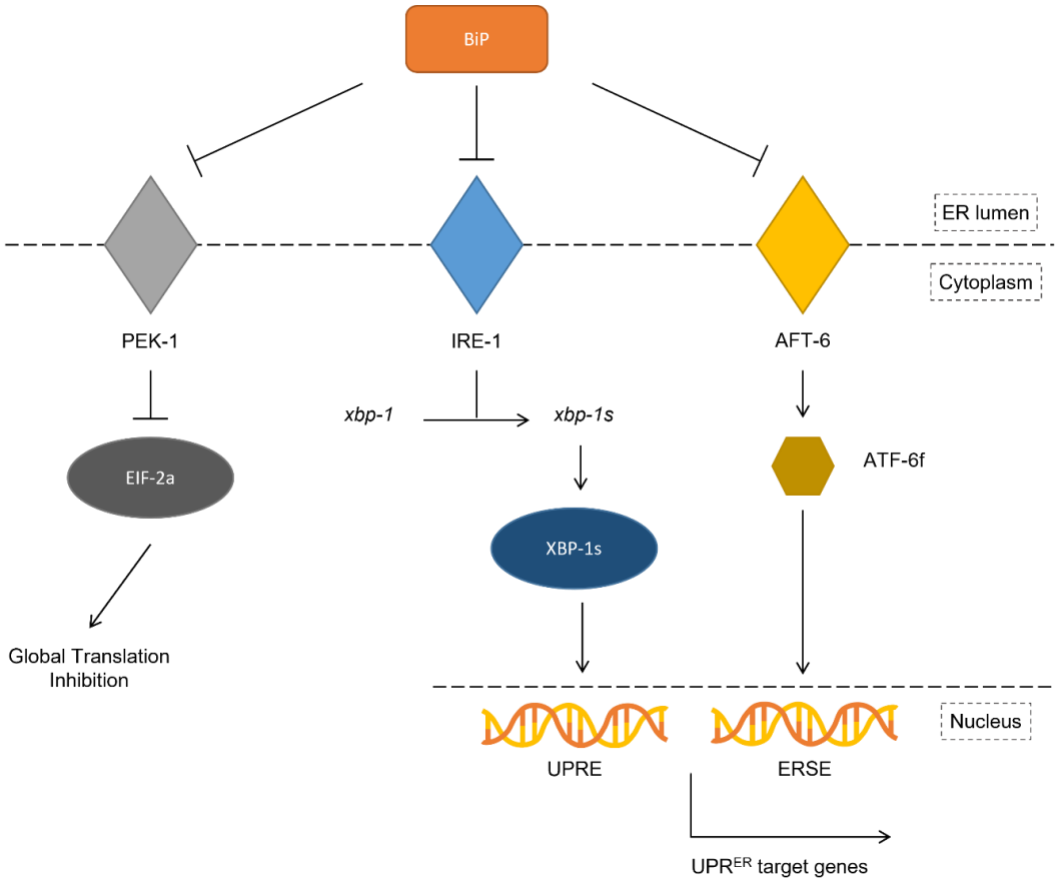

Figure 4. The Unfolded Protein Response of the ER (UPR^{ER}). The ER chaperone BiP renders the UPR^{ER} effectors IRE-1, PEK-1, and ATF-6 inactive. When the demand for ER folding increases, BiP is sequestered elsewhere, leading to the activation of these effectors. PEK-1 facilitates the phosphorylation of the translation initiation factor eIF2a, causing inhibited global translation. IRE-1, catalyses the splicing of *xbp-1* mRNA, generating *xbp-1s*, producing the transcription factor XBP-1s which binds to UPR elements (UPREs), initiating the upregulation of UPR^{ER} target genes. ATF-6 undergoes cleavage, producing the cytosolic fragment ATF-6f, which binds to ER stress elements (ERSEs) and consequently upregulates UPR^{ER} target genes (Figure adapted from: Read and Schröder, 2021).

1.4.3 Unfolded Protein Response of the Mitochondria (UPR^{mito})

Like the UPR^{ER}, the mitochondrial unfolded protein response (UPR^{mito}) is a mechanism which re-establishes a balance when the folding capacity of the mitochondria is overloaded (Jovaisaite, Mouchiroud and Auwerx, 2014). This response is mediated by chaperones in the mitochondrial matrix such as the mitochondrial HSP-70 family chaperone HSP-6, Hsp60 and Hsp10 (Neupert and Herrmann, 2007).

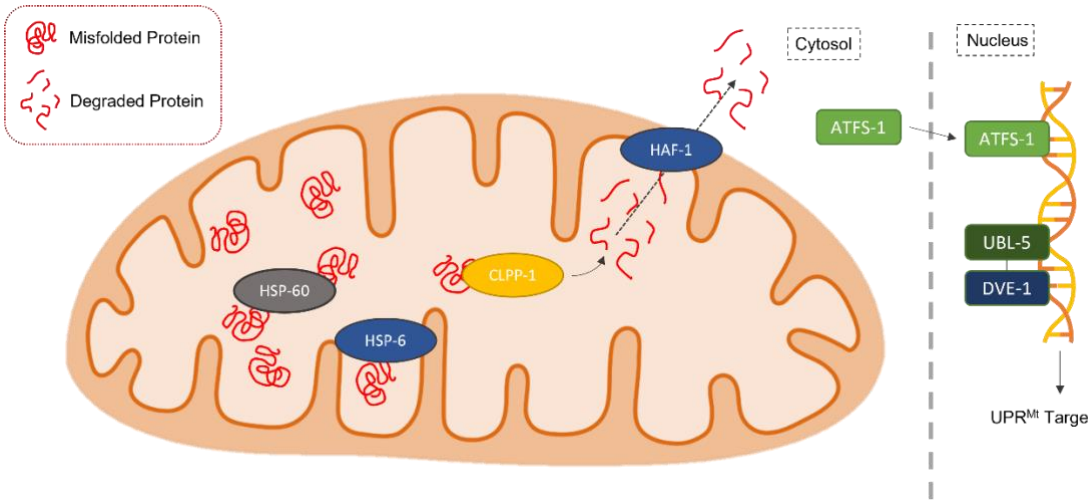

Figure 5. The Unfolded Protein Response of the Mitochondria (UPR^{mito}). When the folding capabilities of mitochondrial chaperones are exceeded, the protease CLPP-1 works to degrade the surplus misfolded proteins. Peptide fragments are then transported to the cytosol through the action of HAF-1, triggering translocation of the transcription factor ATFS-1 into the nucleus. ATFS-1 and a UBL-5/DVE-1 complex, facilitates the upregulation of UPR^{mito} target gene expression (Figure adapted from: Muñoz-Carvajal and Sanhueza, 2020).

Under stressful conditions, the protease CLPP-1 degrades excess proteins into short peptides which are transported into the cytosol via the transporter HAF-1 (Haynes *et al.*, 2010). The presence of degraded protein in the cytosol activates the transcription factor ATFS-1 and translocation to the nucleus. Nuclear ATFS-1 and the UBL-5/DVE-1 complex binds in the promoters of mitochondrial chaperone genes to upregulate their expression, aiding in the restoration of mitochondria proteostasis (Figure 5) (Muñoz-Carvajal and Sanhueza, 2020).

1.4.4 Transcellular Chaperone Signalling

Cell-autonomous stress responses involve intracellular responses to maintain proteostasis, however in multicellular organisms, inter-cell and inter-tissue stress responses are critical to organismal health. Cell-non-autonomous responses regulate protein folding, degradation, and clearance across tissues and organs by endo- and paracrine signalling pathways (van Oosten-Hawle, Porter and Morimoto, 2013). *C. elegans* has been the most common model organism for the study of cell-non-autonomous stress responses (van Oosten-Hawle, Porter and Morimoto, 2013; O'Brien *et al.*, 2018; Miles *et al.*, 2023); however, these responses have also been described in other invertebrates such as *Drosophila melanogaster* (Owusu-Ansah, Song and Perrimon, 2013), and in vertebrates such as mice (Williams *et al.*, 2014; Mu, Wang and Zhao, 2017). Transcellular chaperone signalling (TCS) is a noncanonical systemic stress response which is activated by tissue-specific changes in the expression levels of HSP-90, leading to activation of chaperones in other tissues (van Oosten-Hawle, Porter and Morimoto, 2013). In *C. elegans*, four key genes have previously been implicated in the regulation of TCS, namely *pha-4, pqm-1, asp-12,* and *clec-4* (O'Brien *et al.*, 2018). Notably,

prior research has demonstrated the essential role of *pha-4* in driving the upregulation of the hsp-70p::mCherry reporter in animals subjected to tissue-specific *hsp-90* knockdown. This showed that systemic *pha-4* knockdown, initiated after the L1 developmental stage, significantly diminishes reporter expression in adult *C. elegans* (Miles *et al.*, 2023). TCS has been further demonstrated in *C. elegans* when HSP-90 is over-expressed in the intestine or the neurones. In such circumstances there is a resulting upregulation of HSP-90 in the body wall muscle, under the control of the zinc finger transcription factor PQM-1 and its downstream effectors *clec-41* and *asp-12* (O'Brien *et al.*, 2018). Interestingly, these genes exert their influence in a context-specific manner. The activation of TCS through neuron-specific HSP-90 over-expression hinges on the involvement of neuronal *pqm-1* and *clec-41*. Conversely, TCS triggered by intestine-specific HSP-90 over-expression is dependent on *pqm-1* and *asp-12* (O'Brien *et al.*, 2018).

1.5 Amyloid

Amyloid is an umbrella term for precursor proteins which stack to form protofilaments, the key structural component of an amyloid fibril (Iadanza *et al.*, 2018). Originally referred to as lardaceous liver and in 1639, the term "amyloid" was introduced approximately two centuries later by Virchow. Originally, amyloid was mistaken for starch, after Virchow observed that the deposits displayed positive staining with iodine (Virchow, 1854; Sipe and Cohen, 2000). Thus, the name amyloid was coined from "amylum" and "amylon," the Latin and Greek words for starch. After 5 years, Friedrich and Kekulé clarified that amyloid primarily comprises proteins (Friedreich and Kekulé, 1859), and advancements

in microscopy, coupled with the discovery that amyloid deposits stain positive with Congo red, unveiled the organized nature of amyloid, which comprises highly structured protein subunits (Puchtler, Sweat and Levine, 1962).

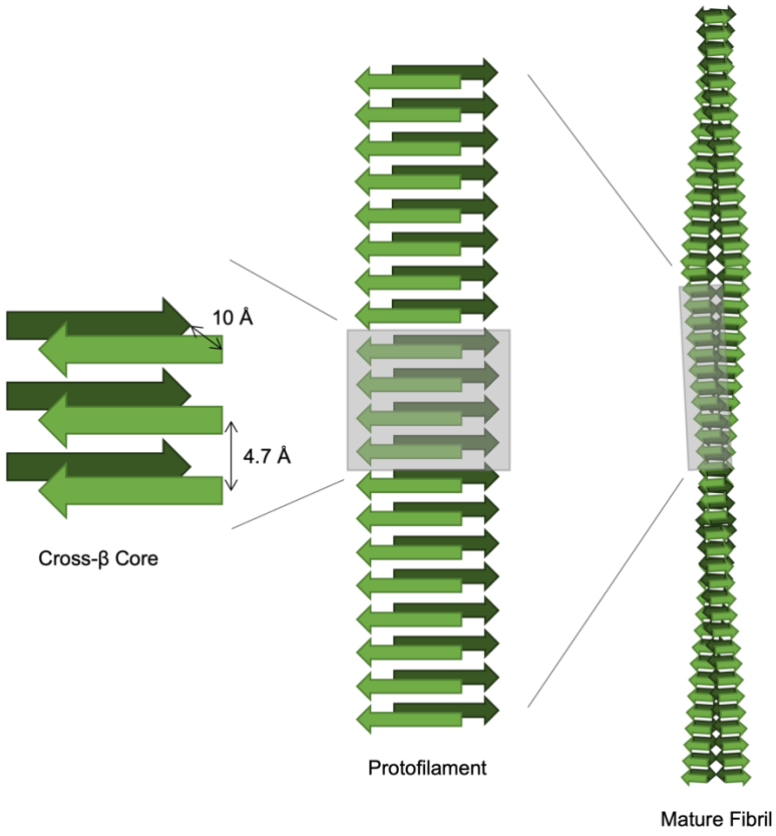

Figure 6. The Amyloid Fibril Structure. The cross-ß architecture of the amyloid protofilament core, with a ~4.7 Å repeat running down the fibril axis. One or more protofilaments self-assemble into mature fibrils by twisting together, with the common cross-ß core (Geddes *et al.*, 1968).

Over nearly 400 years, the progression of amyloid structure research has resulted in the first atomic structures of amyloid fibrils and known characteristics to identify amyloid fibrils. The β-strands of the protofibrils align perpendicular to the long axis of the fibrils termed the cross-β amyloid fold. Each β-strand is separated by a 4.7 Å space resulting from a hydrogen bond between the carbonyl

and amide groups in adjacent ß-strands (Figure 6) (Geddes *et al.*, 1968; Almeida and Brito, 2020).

Single protofilament fibrils can occur (Wasmer *et al.*, 2008), but more commonly at least two protofibrils twist together to form an amyloid fibril (Dearborn *et al.*, 2016; Leistner *et al.*, 2023; Wilkinson *et al.*, 2023) which are stabilized by dry 'steric zippers', where the hydrophobic amino acids of adjacent b-sheets pack together to exclude water (Figure 7) (Gremer *et al.*, 2017). The internal steric zippers and inter-protofilament steric zippers are unique to amyloid fibrils, as the structural motifs have not been observed in any globular proteins currently characterised.

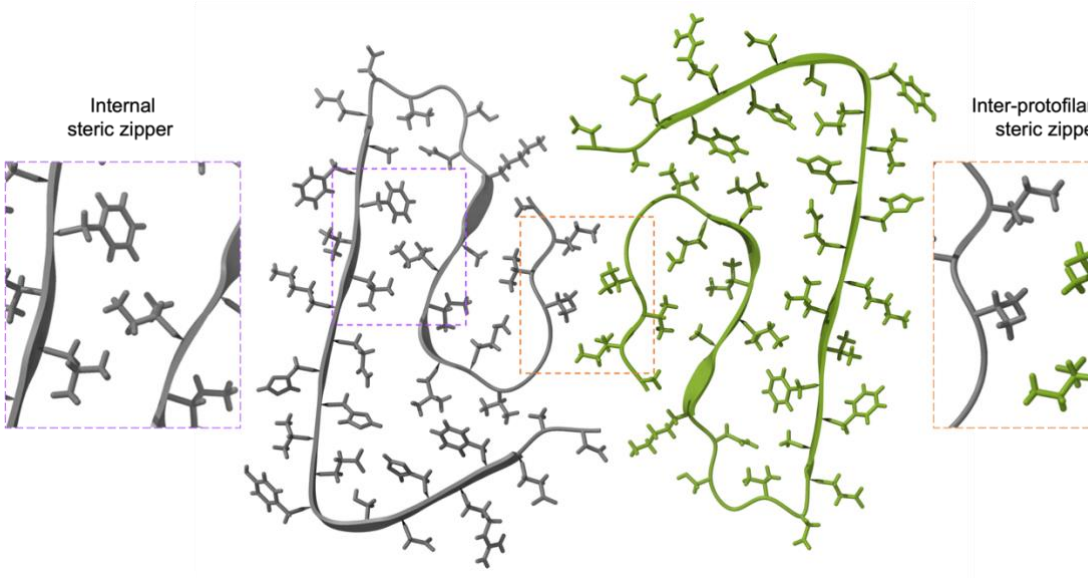

Figure 7. The Steric Zipper Interfaces Which Stabilise Amyloid Fibrils. The structure Aß$_{1-42}$ fibrils (PDB accession number 5oqv) showing how individual protofilaments are stabilised by internal steric zippers (purple box), and how the interface between protofilaments is stabilised by inter-protofilament steric zippers (orange box) (Gremer et al., 2017).

Approximately 50 different proteins or peptides are known to form amyloid fibrils linked with human disease, often associated with neurodegeneration but occasionally systemic disorders. The steric zipper interface has been observed in amyloid fibril structures from various precursor proteins including Beta-2-microglobulin linked to haemodialysis-related amyloidosis, α-synuclein associated with Parkinson disease, and Amyloid-ß (Aß) a key contributor to Alzheimer's Disease (Iadanza *et al.*, 2018).

1.6 Alzheimer's Disease

1.6.1 The Social Impact of Alzheimer's Disease

Dementia is an umbrella term for several diseases linked to cognitive decline and is the leading cause of death in the UK, accounting for 12% of all deaths. Alzheimer's disease (AD) makes up 60-70% of dementia cases, and the most common symptom associated with AD is memory loss. However, the disease can present as changes in behaviour, confusion and disorientation, or delusions and hallucinations.

In 2020, GOV.UK reported that 438,149 patients had been formally diagnosed with dementia in England, with 15,176 of these patients being under the age of 65. At this time, the estimated diagnosis rate for dementia in the UK was 62.4%, therefore, it was estimated that 858,000 people were living with dementia in the UK in 2020 (GOV.UK). Due to Covid-19, current prevalence data is not available, due to inconclusive data following lack of access to healthcare and an increased mortality date in people over 65 and those living in care (Pyne and Brickman,

2021). However, based on previous yearly incidence (118,000) and mortality rate (90,000), the prevalence of dementia in the UK is estimated to be 942,000 in 2023. Dementia and AD impacts patients, and caregivers both emotionally and practically, but on a community level dementia has a huge economic impact and is projected to be the costliest disease, currently incurring a £25 billion cost 50% of which falls under social care (Shore *et al.*, 2023).

1.6.2 Alzheimer's Disease Aβ Pathology

First described by Alois Alzheimer in 1901, AD was determined to be an amyloidosis following the observation of Congo-red positive plaques in the brain (Alzheimer, 1906). The pathophysiology of AD is characterised as a hypothetical model wherein amyloid beta (Aß) accumulates extracellularly in the brain aggregating to form neocortical neuritic plaques preceded by the spreading of tau neurofibrillary tangles (NTFs) (Cras *et al.*, 1991). The Aß plaques and NTFs were first observed by Alois Alzheimer by silver stain in 1907 (Alzheimer, 1907). The Aß peptide originates from the amyloid precursor protein (APP), which is synthesised in the neurones, blood cells, and astrocytes (Hampel *et al.*, 2021). The majority of APP is processed via the α-secretase pathway, which produces a small fragment called p3. The p3 peptide's function, and if it plays a role in AD, is unknown. The Aß peptide is produced when APP is cleaved at its N-terminal end, by the enzyme ß-secretase. This produces C99, a peptide which is subsequently cleaved at its the C-terminus by γ-secretase to release Aß from the cell (Chow *et al.*, 2010). Several isoforms exist, but the predominant species are $Aß_{1-40}$ and $Aß_{1-42}$, the latter of which is regarded as the more toxic of the two (Younkin, 1995; Duff *et al.*, 1996; Lambert *et al.*, 1998).

There are several types of AD, characterised by the age of onset, disease duration, and the region of the brain affected. The most common form is late-onset AD (lo-AD), affecting patients over the age of 65. While lo-AD has no confirmed associated genetic mutation, genetic risk factors have been identified through large-scale genomic studies (European Alzheimer's Disease Initiative (EADI) *et al.*, 2013). Mutations in the apolipoprotein E (APOE) ε4 allele pose a significant risk to developing both lo-AD and early onset AD (eo-AD) (Liu *et al.*, 2013). The APOE protein functions to transport lipids and support synaptic homeostasis, cerebrovascular function, and glucose metabolism and is known to bind soluble Aß. The APOE ε4 allele is associated with an increased processing of Aß from APP, intracellular misfolding, and plaque formation. Further risk factor genes for lo-AD are linked to Aß expression, trafficking, and degradation including several genes associated with ubiquitination, a process essential to cellular protein clearance. While the aetiology of lo-AD is unclear, the mechanism seems to be underpinned by an imbalance between production of Aß by neurones and its extracellular clearance. The fractional production and clearance rates of Aß in the central nervous system (CNS) are 7.6% and 8.3% per hour, respectively. Small reductions in Aß clearance results in the dysfunction of the proteostasis network, causing Aß accumulation and neurotoxicity (Mawuenyega *et al.*, 2010).

Early onset AD (eo-AD) is a rare form of AD which affects patients under the age of 65 and is primarily caused by a genetically-driven imbalance resulting in overproduction of Aß. Mutations in three key genes, the APP gene, and the presenilin 1 and 2 (PSEN1 and PSEN2) genes are key contributors in some cases of genetic eo-AD (Jansen *et al.*, 2019). PSEN1 mutations are the most reported

autosomal dominant transmitted link to eo-AD, followed by mutations in the APP gene. APP mutations cluster around the domain containing Aß cleavage sites and cause increased substrate affinity resulting in either a larger pool of Aß, or an imbalanced ratio of the more toxic $Aß_{1-42}$ over $Aß_{1-40}$, which is theorised to promote self-aggregation (Wisniewski *et al.*, 1985; St George-Hyslop *et al.*, 1987; Cruts, Theuns and Van Broeckhoven, 2012; Hooli *et al.*, 2012). Unlike PSEN1 mutations, PSEN2 mutations are uncommon and are observed in both lo-AD and eo-AD patients, moreover PSEN2 mutations are reported in other amyloidoses including dementia with Lewy bodies and frontotemporal dementia.

Aß is released from the cell as a soluble monomer and is found in an intrinsically disordered. The monomeric species $Aß_{1-42}$ is less soluble in contrast to $Aß_{1-40}$ and has a higher propensity to aggregate. Unfolded or intermediate folded states commonly initiate oligomer formation during the nucleation phase of fibril formation (Figure 8). Soluble oligomeric species form higher-order oligomers, eventually forming the crucial oligomeric nuclei required for rapid polymerisation and recruitment of monomers for fibril assembly during the elongation phase. During this phase, fibrils can fragment producing a new nucleation point for fibril assembly. Fibrils will grow exponentially until all free monomer has been recruited into a fibrillar form, wherein fibrils enter the stationary phase, and associate with each other to form amyloid plaques characteristic to AD (Figure 8).

Despite their apparent stability, fibrils are dynamic and can release oligomers, assemblies which *in vitro* and *in vivo* studies indicate are toxic (Tipping *et al.*, 2015). Post-mortem extraction of Aß oligomers from AD patient brains suggest oligomers form protein complexes ranging from dimers to dodecamers. Injecting

soluble low-number oligomers into the hippocampus of rats results in interrupted synaptic plasticity, while high-number oligomers promote reduced expression of memory-related receptors and synaptic deterioration resulting in significant neurotoxicity (Selkoe, 2008; Bernstein *et al.*, 2009).

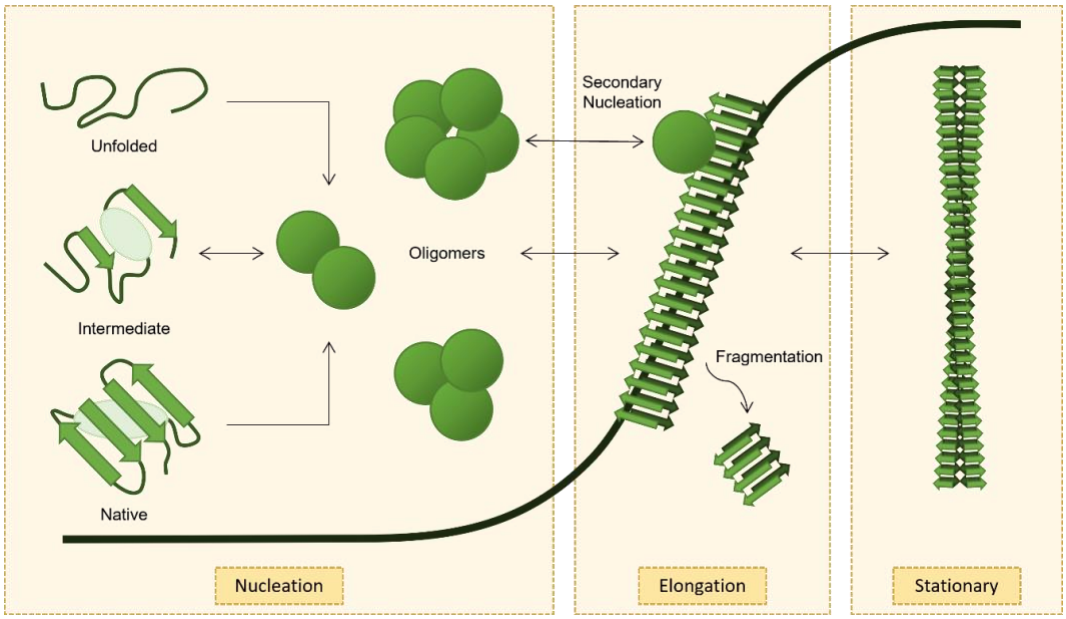

Figure 8. Schematic of Amyloid Formation. Proteins known to form fibrils exist in unfolded, partially folded, or native states, and one or more of these states assemble into oligomers. During the nucleation phase, oligomeric species then assemble into high-number oligomers, which can become a fibril nucleus. This nucleation site rapidly recruits monomer to form protofilaments, the ends of which can fragment offering a new nucleation site for elongation. During the elongation phase, oligomer formation can be catalysed on the surface of a pre-existing fibril allowing for fibril growth. One or multiple protofilaments twist together to form a stable, amyloid fibril, which can associate with each other to form amyloid plaques (Figure adapted from: Iadanza *et al.*, 2018).

1.7 The Potential of Caenorhabditis elegans (C. elegans)

1.7.1 The History of *C. elegans*

Caenorhabditis elegans (*C. elegans*), is a microscopic roundworm which has been extensively studied in biology since 1963 as a result of Sydney Brenner's hunt for a novel animal model (Fatt and Dougherty, 1963; Brenner, 1974). The goal was to uncover a simple metazoan model in which to study cellular biology, genetics, and development. Brenner recognized the potential of *C. elegans* as a model organism due to its simplicity, short lifespan, and ease of cultivation. His work with *C. elegans* paved the way for major breakthroughs in understanding the organism's biology and its broader implications.

Brenner identified several key characteristics of *C. elegans* that made it particularly amenable to genetic analysis, such as its well-defined cell lineage and invariant number of cells. Brenner's most significant contributions was the establishment of *C. elegans* as the first animal to have its entire genome sequenced (Brenner, 1988).

1.7.2 The Morphology of *C. elegans*

C. elegans are non-parasitic, transparent nematodes with cylindrical bodies and distinct head and tail regions. The body consists of an inner tube holding the intestine, pharynx, and gonad, and an outer tube containing the cuticle, muscles, and neurons (Figure 9). Healthy adult hermaphrodites have a diameter of ~ 50 μm and measure ~ 1 mm in length. They have 959 somatic cells, and 302 neurons

that are organized in several ganglia in the head and tail and into a spinal cord-like ventral nerve cord (Eisenmann, 2005).

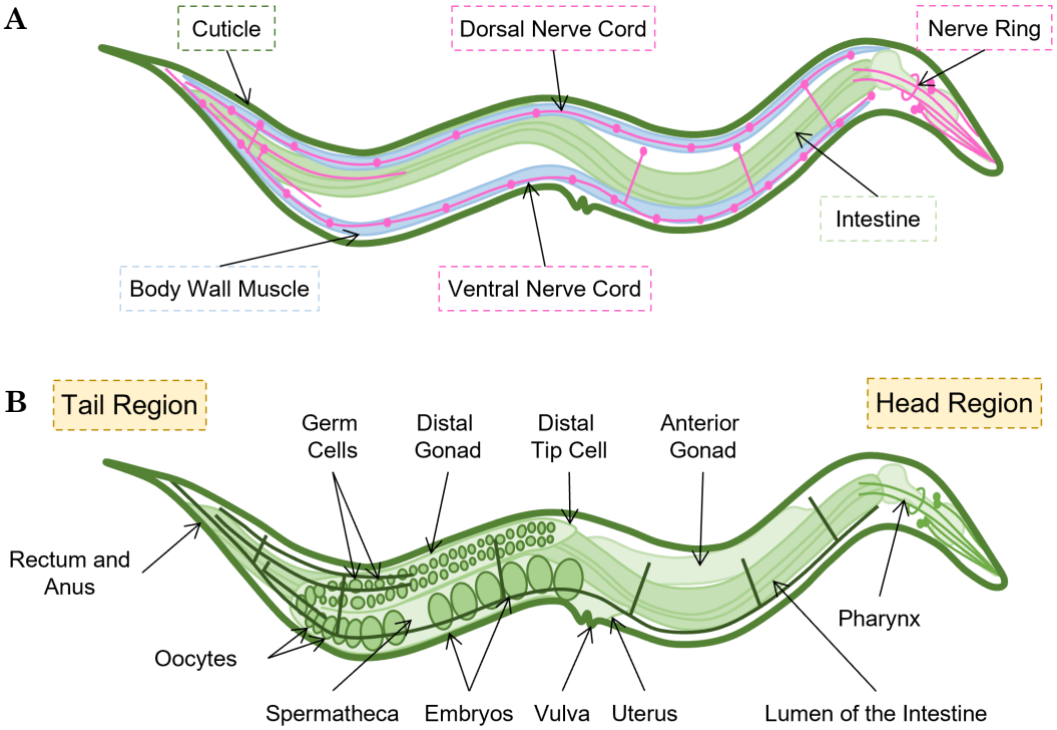

Figure 9. The Tissues of *Caenorhabditis elegans*. (A) Diagram of an adult hermaphrodite *C. elegans* with selected tissues focused on during this work. Pink represents the nervous system, blue indicates the body wall muscle, and light green indicates the intestine. (B) Diagram of adult hermaphrodite *C. elegans* with anatomical features highlighted (Eisenmann, 2005).

C. elegans have two sexes, hermaphrodite (XX) and male (XO). Males are essential for producing cross-strains. However, males are rare and arise naturally in ~ 0.1% of the population due to spontaneous nondisjunction in the hermaphrodite germ line or more commonly through heat shock mutation or mating (50%) (Walsh, Boivin and Barr, 2020).

When the *C. elegans* genome was completed, it showed a compact genome of roughly 100 million base pairs (Brenner, 1988). Furthermore, it is predicted that approximately 38% of C. elegans genes have a human ortholog. A strong understanding of *C. elegans* genetics means that manipulations such as rapid mutation mapping, generating transgenic animals, forward genetic screens and reverse genetic RNAi screens, can be performed with ease (Berkowitz *et al.*, 2008; Conte *et al.*, 2015; Kawamura and Maruyama, 2019).

1.7.3 The Lifecycle of *C. elegans*

Following the embryonic stage, *C. elegans* undergo four larval stages, L1 to L4, before reaching adulthood (Figure 10). The timespan with which this happens differs depending on the temperature at which animals are cultured. This is lab and strain dependent, but is commonly 15ºC, 20ºC, or 25ºC. The most efficient maximal egg-laying rate is observed at 20ºC, at 9.1/hour, compared to 5.4/hour and 8.1/hour at 15ºC and 25ºC respectively (Gómez-Orte *et al.*, 2018). This suggests that 20ºC is the optimal growth temperature. This life cycle is genetically predetermined; the only deviation occurs when L1 larvae are exposed to an overcrowded environment with too little food. This setting is not conducive for reproduction and population growth; therefore, an alternative developmental pathway is selected. This results in L1s entering diapause, developing to the L2d stage, and finally arrested development as Dauer larvae (Golden and Riddle, 1984). The Dauer stage is an alternative developmental phase in which the larvae enter a form of stasis, allowing them to live up to 4 months without food. This is beneficial in research as it allows for short-term storage on solid agar plates.

When Dauer animals are reintroduced to food, they re-enter the conventional development cycle as L4 animals (Figure 10) (Raizen *et al.*, 2008).

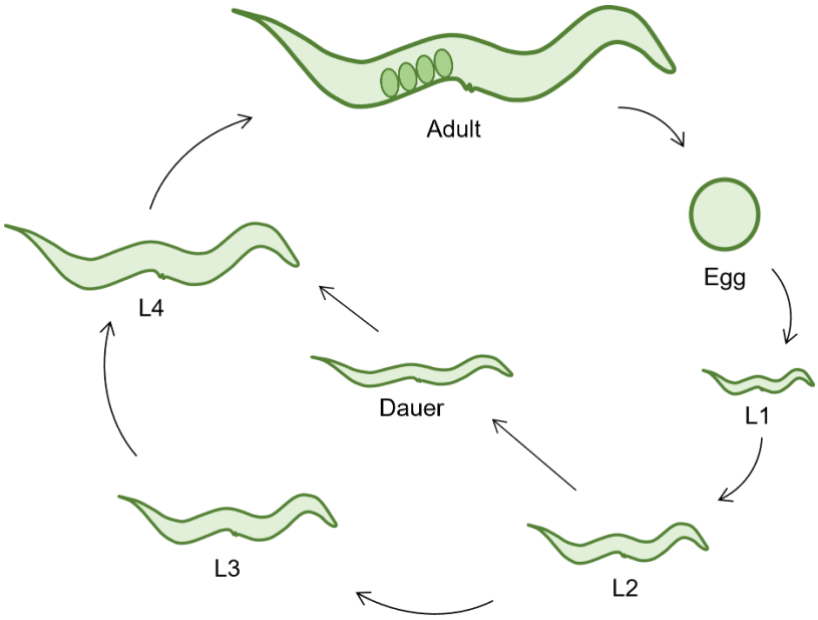

Figure 10. The Life Cycle of *Caenorhabditis elegans*. Life cycle of the self-fertilising *C. elegans* hermaphrodite. Adult animals lay eggs, L1 stage hatch from these eggs progressing onto the L2 stage of development. If conditions are favourable, the larvae continue through developmental stages into reproductive adults. In starved and overcrowded conditions, animals enter the dauer stage, an alternative L3 stage. Upon feeding, dauer animals can progress into L4 animals and onto become reproductive adults.

1.7.4 The Advantages and Disadvantages of the *C. elegans* model

C. elegans is a simple organism, with a relatively small number of cells permitting researchers to understand and study the complete cellular development and differentiation of the organism with ease. However, this simplicity can be a disadvantage owing to the organism lacking complex physiological attributes found in higher organisms. *C. elegans* are not useful for studying certain pathways, organ systems or specialized cell types, for example the animals lack an adaptive immune system, and the significant difference between *C. elegans* innate immune responses and those found in mammals make *C. elegans* unsuitable for immunological studies (Pukkila-Worley and Ausubel, 2012). Conversely, in 1988 *C. elegans* was the first animal to have its entire genome sequenced allowing for decades of genetic information to accumulate and providing researchers with a strong understanding of the models' genes, their functions, and interactions (Brenner, 1988). Fundamental genetic pathways are conserved in *C. elegans* and higher organisms, including humans. When applied to the correct studies, such as investigating gene regulation, genetic pathways, and disease, *C. elegans* are a powerful model.

The short lifespan of C. elegans allows researchers to study the complete life cycle and observe the effects of genetic and environmental manipulations on aging and lifespan. Furthermore, the fast reproductive rate, allows for many offspring to be generated in a short period, facilitating genetic studies and experiments on tractable timescales (Zhang *et al.*, 2020).

In a laboratory environment, *C. elegans* are usually very easy to maintain and handle. They are inexpensive to both purchase and maintain, grown on agar plates or liquid cultures and fed OP-50 *E. coli*. Due to self-replication, the animals can be grown in large quantities, frozen and kept at -80ºC for long term storage (Eisenmann, 2005).

As it is an invertebrate, there are no ethical considerations in working with *C. elegans*, increasing the research potential of the model compared to vertebrate models. However, there is debate regarding experiments involving pain perception, due to the possible distress to the model (Ha *et al.*, 2022).

C. elegans exhibit basic sensory and motor functions, which can be exploited in research as behavioural readouts. Some examples of this include thrashing assays, wherein the number of body bends a single nematode suspended in liquid completes are counted to measure muscle deterioration (Buckingham and Sattelle, 2009). However, in contrast to higher organisms, behavioural repertoire of *C. elegans* is limited making it a challenge to study complex cognitive functions and behaviours in this model.

C. elegans possess a flexible exoskeleton called the cuticle, which attaches to the body wall muscle of the animal assisting with movement and acting as a protective barrier from the environment (Johnstone, 1994). While the cuticle benefits the worm, it can interfere with research by preventing the uptake and distributions of drugs and stains. Pharmacologically, drug metabolism in *C. elegans* differs from higher organisms, and oral drug intake can vary animal to

animal causing an array of results (Njume *et al.*, 2022). This limits the use of *C. elegans* in therapeutic investigations.

The advantages stated make *C. elegans* a valuable model organism for a wide range of research. The model has contributed significantly to our understanding of basic biological processes and while disadvantages are present *C. elegans* is an instrumental model organism especially when used in tandem with other model organisms or cell culture.

1.7.5 *C. elegans* as a model for Alzheimer's Disease

While *in vitro* studies have much to offer when studying amyloid aggregation, they cannot accurately recreate the complexity of a whole organism, *in vivo* environment. Despite limitations, *C. elegans* offer compelling advantages for studying age related diseases to their short lifespan (Zhang *et al.*, 2020). However, despite retaining an APP-related gene (*apl-1*), Aβ is not endogenously expressed in *C. elegans* due to a lack of BACE sites and β-secretase (Hornsten *et al.*, 2007). To overcome this, the first *C. elegans* AD amyloid model was generated by expressing human $A\beta_{1-42}$ in the body wall muscle of the animal ($MA\beta_{3-42}$) (Link, 1995). These animals displayed muscle-specific, anti-β immunoreactive deposits, indicative of Aβ aggregation in the muscle cells. However, mass spectrometry could not detect the expression of $A\beta_{1–42}$ but rather detected a major species that had an *m*/*z* consistent with $A\beta_{3–42}$; presumably due to an undetermined cleavage event of the Aβ transgene (McColl *et al.*, 2009). Specific truncations can affect the activity of Aβ, and different isoforms show varying levels of neurotoxicity. Comparing the motility and chemotaxis of animals expressing $A\beta_{1-42}$ to $A\beta_{3-42}$ has

shown N-terminal truncations of Aß cause higher aggregation propensity and increased neurotoxicity. While varying isoforms of Aß are present in AD, a model expressing $Aß_{1-42}$ is a more medically relevant disease model (McColl *et al.*, 2012). Following this discovery, an improved Aß model was generated expressing the full length $Aß_{1-42}$ via gonad micro-injection, confirmed by mass spectrometry. Moreover, $Aß_{1-42}$ aggregation in this strain presented with an age-dependent paralysis phenotype at 20°C, which can be exacerbated by upshifting the temperature to 25°C (McColl *et al.*, 2012).

The phenotypes observed in muscle strains can be exploited for screening approaches. Investigating the effect on neurons is not possible using these strains. Expressing $Aß_{1-42}$ in the neurones comes with limitations, but higher clinical relevance (Wu *et al.*, 2006; Gallrein *et al.*, 2021). Over-expressing amyloid from a young age can affect the progeny and development of the strain. There are two methods of combatting this, temperature inducible strains or lower the level of protein expression, both of which have advantages and disadvantages.

A temperature-inducible transgenic $MAß_{1-42}$ strain was generated to establish a correlation between amyloid deposits and the paralysis phenotype. This was achieved using the mRNA Smg surveillance system in *C. elegans*. This system uses an unusually long 3' UTR which produces unstable mRNA from the transgenic gene, and the temperature-sensitive smg-1 mutation. At non-permissive temperatures, the extended 3' untranslated region degrades the mRNA in a wild type (Smg+) genetic background, resulting in poor transgene expression. In contrast, at permissive temperatures in an Smg- background, such

as the smg-1 mutation, the mRNA surveillance will fail, resulting in the translation of the mRNA (Pulak and Anderson, 1993).

This system is utilised in the iNAß$_{1-42}$ strain, to drive inducible pan-neuronal expression of Aß$_{1–42}$ upon temperature upshift to 25°C. This strain exhibits aggregation alongside impaired chemotaxis, decreased lifespan, and experience-dependent and associative learning, forming a link between aggregation and neurodegeneration (Wu *et al.*, 2006). The success of iNAß$_{1-42}$ led to increased interest in generating strains expressing Aß$_{1-42}$ in a subset of neurons, such as in the glutamatergic neurons, ASE or BAG neurons (Treusch *et al.*, 2011; Cotella *et al.*, 2012; Sinnige *et al.*, 2019).

Selectively expressing Aß$_{1-42}$ by temperature upshift at a specific timepoint in adulthood rather than throughout the whole lifespan of the worm has more clinical relevance as, despite Aß being produced constantly, the effectiveness of misfolded protein clearance reduces with age giving rise to protein aggregation and disease (Cuanalo-Contreras *et al.*, 2023). Additionally, studying the heat shock response in temperature inducible strains can skew results and cloud interpretations of the data.

Additionally, until recently, the Aß$_{1-42}$ peptides in *C. elegans* AD models were not fluorescently tagged. Owing to the transparency of C. elegans, the kinetics and mechanisms of oligomer and amyloid fibril formation can be followed by fluorescently tagging amyloid or using anti-amyloid antibodies. There has been moderate success with *in vivo* staining, meaning amyloid deposition in individual animals can be observed over time. Fluorescent labelling of the Aß$_{1-42}$ peptide is

technically challenging (Link *et al.*, 2001). If GFP is fused at the C-terminal tail, Aß aggregation causes GFP to fold incorrectly preventing the chromophore from forming (Ochiishi *et al.*, 2016). In previous attempts to mitigate this, the hydrophobic region of $Aß_{1-42}$ was mutated to increase solubility, however upon observation oligomers of various size were detected, but no fibrilization (Ochiishi *et al.*, 2016).

A new system was developed to overcome the challenge of fluorescently tagged $Aß_{1-42}$ in *C. elegans* utilizing a sub-stoichiometric labelling model (Gallrein *et al.*, 2021). In this model, tagged and untagged $Aß_{1-42}$ are simultaneously translated from one bicistronic mRNA resulting in a lower proportion of tagged $Aß_{1-42}$ being translated compared to untagged; in a ratio of approximately 1:10. This is achieved using the differential efficacies of cap-dependent and cap-independent, IRES-driven translation of mRNAs (Li and Wang, 2012). The higher efficiency of the cap-dependent translation results in a larger proportion of untagged $Aß_{1–42}$ peptides, which allows for unperturbed fibril growth of untagged $Aß_{1-42}$ with random integration of tagged $Aß_{1-42}$ (Gallrein *et al.*, 2021).

Following on from the success of *C. elegans* AD models, additional strains expressing a range of amyloid precursor proteins have been generated including transthyretin (Madhivanan *et al.*, 2018), α-synuclein (Van Ham *et al.*, 2008), b2-microglobulin (Diomede *et al.*, 2012), and polyglutamine (Morley *et al.*, 2002) amongst others. These disease models have aided in furthering our understanding of amyloid aggregation and disease progression *in vivo*.

1.8 Methods of Characterising Protein Structure

Characterising protein structure is essential to understanding functions underpinning mechanisms and signalling pathways. Elucidating protein structure provides information such as protein size, conformation, folding, protein-protein interactions, and conformational changes upon environmental change or ligand binding. Different levels of protein structure can be assessed using different techniques, the atomic structure by X-ray crystallography and nuclear magnetic resonance (NMR), macromolecular assemblies by atomic force microscopy (AFM), or secondary structure by circular dichroism (CD). Additionally, near atomic resolution, macromolecular assemblies, and organelle or cellular structures can be characterised by electron microscopy and fluorescent methodologies.

Early successes in X-ray crystallography saw the characterisation of the atomic structure of sodium chloride in 1913 {Citation}. This work expanded to myoglobin, the first protein structure to be solved in the 1959's by John Kendrew. Due to the high resolution achieved through X-ray crystallography, it has been the preferred method of solving protein structures, and generating models with high confidence in atom positioning, a feature essential for understanding protein complexes. X-rays are photons with wavelengths between 0.1 – 5 Å with interact with the electrons orbiting each atom in a structure to produce a diffraction pattern. Macromolecules are crystalised to amplify this diffracted signal, which is collected and used to determine atomic structure. Crystallization is often the bottleneck when characterising proteins by X-ray crystallography as not all proteins will crystalise (Divan and Royds, 2013).

Solution-state NMR is the only method of protein characterisation wherein the sample remains in an aqueous solution. The concept is the nuclei of an atom spins when a strong magnetic field is applied shifting from a lower energy state (α) to a higher energy state (ß). The amount of energy required to shift between the two states is different for different atoms and the resonant frequencies of the nuclei is recorded as an NMR peak. Spectral data is used to assign peaks to amino acid residues at specific positions and secondary structure (Divan and Royds, 2013).

Lower resolution methods are still valuable when studying macromolecules. AFM offers a method for gaining structural information at an intermediate resolution (1 – 100 nm) is useful for studying sample topography and the mechanical properties of single molecules. Topography is measured using a mechanical probe which is moved along the surface of the sample and measures changes in contour height. CD spectroscopy can be used to study how secondary protein structure changes in response to stimuli by measuring the interaction of circularly polarised light with chiral molecules. The spectropolarimeter light source switches between left and right polarised light, both signals are measured, and the difference between the absorbances or ellipticity is recorded. A CD spectra of mean residue ellipticity is used to characterise secondary structure, using known characteristic spectra for ß-sheets, α-helices, and intrinsically disordered protein (Divan and Royds, 2013).

1.8.1 Advances in Microscopy

In simple light microscopy, light passes through a sample uniformly, and in thicker samples light from above and below the focal plane will be detected out of focus, reducing the resolution of the image. This is circumvented using a confocal microscope which reduces the out-of-focus light from the detector using a spatial pinhole which offers the ability to image into thick tissues with high resolution (Webb, 1996).

Other available microscopy methods include 2 Photon Microscopy, a more suitable method for live cell imaging as fluorophores are excited with 2 photons at a lower intensity, reducing the result of bleaching, tissue damage and scattering (Theer *et al.*, 2006). For improved resolution at higher magnification, super resolution systems have been developed to examine the morphology structures smaller than 200 nm. There are two methods of super resolution, deterministic super resolution includes methods such as stimulated emission depletion (STED) (Hell and Wichmann, 1994), and stochastic super resolution with systems such as stochastic optical reconstruction microscopy (STORM) (Rust, Bates and Zhuang, 2006), and photoactivation localisation microscopy (PALM) (Betzig *et al.*, 2006).

1.8.2 An Introduction to CryoEM

Many methods of structural characterisation dehydrate or remove biological specimens from their native, aqueous environment, potentially affecting protein structure. This can be avoided using cryogenic electron microscopy (cryoEM), wherein 3D information can be reconstructed from 2D information (Thompson *et al.*, 2016). In cryoEM, samples are rapidly frozen (~10^6 °C/s) to produce vitreous

ice, an amorphous solid form of water which lacks a crystal lattice observed in common, crystalline ice (Dubochet *et al.*, 1988). Once cryogenically immobilised, samples can be imaged by EM, and reconstructed to produce the near atomic structure of proteins and complexes (Bai *et al.*, 2013). Additionally, cryoEM can be employed to study large macromolecular assemblies, such as protein complexes often unsuitable for characterisation by X-ray crystallography or NMR.

CryoEM was first successful in characterising the native structure of the membrane protein bacteriorhodopsin to a near atomic resolution of 3.5Å (Henderson *et al.*, 1990). Since then, electron microscopy has undergone a 'resolution revolution', with many high-resolution structures being characterised owing to improvements in imaging hardware, image processing software, and methods of sample preparation. There are several methods of determining structure with cryoEM, selected depending on the properties of the sample being analysed including single particle analysis (SPA) (Lau and Rubinstein, 2013), helical reconstruction (Egelman, 2015), 2D crystallography (Schenk *et al.*, 2010) and electron tomography (cryo-ET) (Lučić, Förster and Baumeister, 2005; Briggs, 2013).

Single particle analysis (SPA) is the most common and favourable for purified homogenous proteins and complexes. The sample is frozen and 2D projection images are collected using a limited exposure of electrons to reduce radiation damage, resulting in images with a low signal to noise ratio (SNR) (Zhang *et al.*, 2008). The 2D projection images contain many 'single particles' at different orientations, and if the SNR is high enough the angular relationships between the orientation of each particle can be coherently averaged. If all possible views

of the specimen are recorded, these can be combined to generate 3D information (Lau and Rubinstein, 2013).

Helical reconstruction is used for specimens with helical symmetry such as microtubules and amyloid fibrils (Egelman, 2015). Many helical structures have been characterised to near atomic resolution using cryoEM. Such projects exploit the fact that a projection image of a helix captures many different views of identical subunits (Ge and Zhou, 2011). Cryo-ET and 2D crystallography employ an alternate strategy to generate 3D information, wherein the specimen is tilted around a fixed axis, usually between ±65° in 2° increments, to obtain the different angular views required for 3D reconstruction (Briggs, 2013). The tilt increment is used to calculate the angular relationship between each image and reconstruct 3D information. 2D crystallography for proteins, significantly smaller than 150 kDa that form ordered 2D arrays. Cryo-ET stands as the sole option for unique assemblies such as organelles and proteins *in situ* (Callaway, 2020).

1.8.3 Methods in Cryo-ET

Cryo-ET is suitable for samples of varying size, from pleomorphic viruses to thick samples such as cells or organisms like *C. elegans* (Schaffer *et al.*, 2019; Hover *et al.*, 2023). Depending on the sample, the method of freezing differs wherein thinner samples such as heterogenous protein or viruses, fractionated tissue homogenates, or cells grown on grids can be plunge frozen and either imaged or FIB-milled to produce ultra-thin lamella (Sibert *et al.*, 2021). Thicker samples are high pressure frozen, prior to cryo-sectioning or freeze substitution for room temperature sectioning (Leistner *et al.*, 2023). Cryo-sectioning methods of high

pressure frozen samples include cryo-lift out (Parmenter and Nizamudeen, 2021) or cryo-EM of vitreous sections (CEMOVIS) (Al-Amoudi *et al.*, 2004), which produce ultra-thin vitreous tissue sections, which are adhered to grids and imaged by cryo-ET and reconstructed to produce tomograms (Briggs, 2013). The resolution of tomograms is less than 10 nm, however with subtomogram averaging reconstructions can reach a resolution of 10 Å. Subtomogram averaging combines tomography with single particle analysis, where copies of the same structure can be reconstructed to a higher resolution within the tomogram (Schur *et al.*, 2015).

Tomograms are only valuable if you can identify features with certainty. Some cellular structures are clear, such as mitochondria and ribosomes, however many smaller features are often difficult to recognise at lower resolution, notably finding protein complexes in situ. Cryogenic correlative light electron microscopy (cryo-CLEM) is a method that has been developed to combine fluorescent microscopy with fluorescent markers to track proteins and cellular components simultaneously in cryo-ET (Jun *et al.*, 2019).

1.8.4 The structure of Aβ

Numerous instances of Aß polymorphism have been observed, where a single polypeptide sequence leads to diverse protein folding structures. Strands align parallel in register, where the strand orientation is consistent, and the same amino acids are stacked directly above each other. In certain structural configurations, fibril cores display parallel ß-sheets that are in register, although the N-terminus and C-terminus may exhibit disorder (Ghosh *et al.*, 2021).

Typically, fibrils are formed by the association of two Aß protofilaments, creating a helical twist that is stabilised by salt bridges or hydrogen bonds. This twist demonstrates either C2 symmetry or pseudo-2_1 symmetry (Kollmer *et al.*, 2019; Al Adem and Lee, 2023), with C2 symmetry occurring when subunits are precisely packed in register and exhibit a 180° helical twist. Within pseudo-2_1 screw symmetry, strands precisely out of register, causing one subunit to shift 2.4 Å further along the axis of the fibril (Kollmer *et al.*, 2019; Al Adem and Lee, 2023).

CryoEM was used to build a 4.0 Å resolution *de novo* atomic model of an $Aß_{1-42}$ fibril (Gremer *et al.*, 2017). This is the highest resolution complete $Aß_{1-42}$ fibril accomplished by cryoEM. The resolution was high enough to observe two twisted protofilaments, and all 42 amino acids. Single subunits of recombinantly expressed human $Aß_{1-42}$ adopt an LS-shaped configuration, wherein the N terminus assumes an L-shape while the C terminus is S-shaped (Figure 11A) (Gremer *et al.*, 2017). When compared to a different Aß polymorph characterised by solid-state NMR (Figure 11B) (Wälti *et al.*, 2016), the C termini share structure similarities however in contrast to the NMR-derived structure, the N-terminal region was integrated into the cross-ß structure of the Aß fibril.

Recently, $Aß_{1-42}$ fibrils were purified from murine brain tissue and from the brain tissue of humans suffering from sporadic AD (type I) and familial AD (type II) and characterised for the first time by cryoEM. Human type I (Figure 11D) and type II (Figure 11E) share some similarities, such as both fibril structures have ordered cores and disordered N-terminal tails, and the protofilaments form an S-shape configuration between residues 19 – 42 and 20 – 42 respectively (Yang *et al.*, 2022).

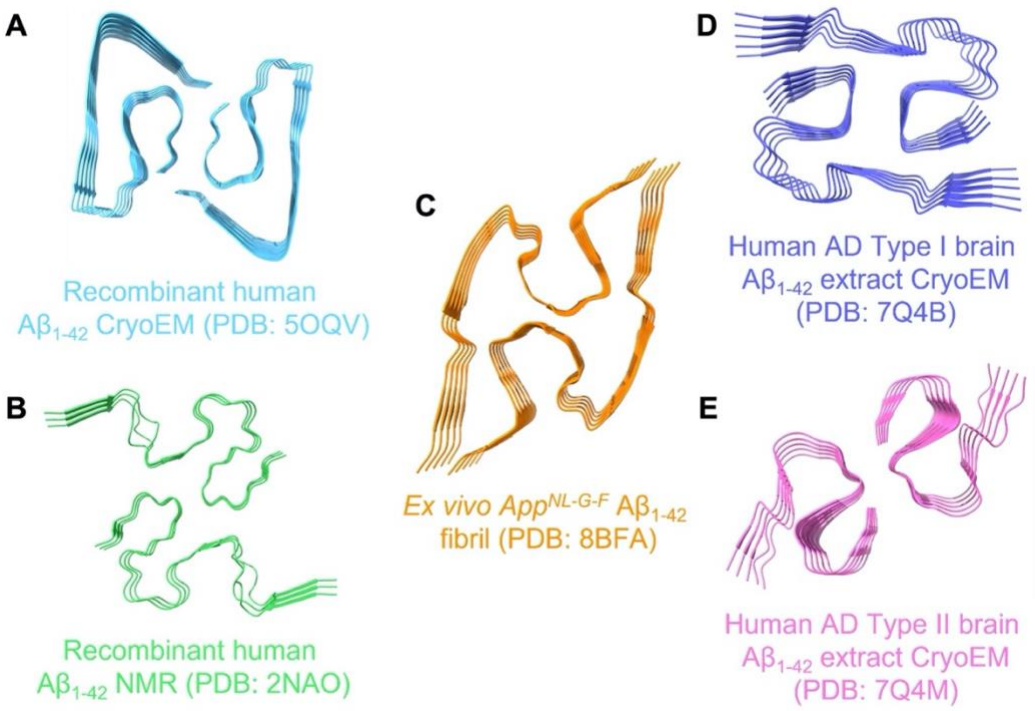

Figure 11. Deposited Aβ1-42 Fibril Structures. The structures of recombinant human Aß1-42 purified from *E. coli* cells and characterised using (A) CryoEM (Gremer *et al.*, 2017) and (B) NMR (Wälti *et al.*, 2016) show distinct differences in fibril structure. The structure of Aß1-42 fibrils purified from (C) *App*$^{NL-G-F}$ mouse brains, (D) the brain of a human with sporadic AD (Type I) (Yang *et al.*, 2022), and (E) the brain of a human with familial AD (Type II) by single particle cryoEM (Leistner *et al.*, 2023).

App^{NL-F} knock-in mice express humanised Aß and possess the Swedish double mutation (KM670/671NL), and the Beyreuther/Iberian mutation (I716F) in APP. They develop age-dependent aggregates of human Aß1-42, and display neuroinflammation and memory impairment. The Aß1-42 fibrils purified from *App*$^{NL-F}$ (Figure 11C), shared structural similarities with the human type II structure (Figure 11E) (Yang *et al.*, 2022; Leistner *et al.*, 2023). It is also key to note that the method of protein purification and structural characterisation may

play a role in changes in fibril conformation resulting in structural polymorphs as observed in Figure 11. Thus, observing protein structure in its native environment, such as *in situ* using cryo-ET, may be paramount to understanding the mechanism of fibril growth and play a role in rational drug design

Chapter 2. Materials and General Methods

2.1 Preparation of NGM, NGM-FUdR, and NGM-RNAi Agar Plates

Nematode growth medium (NGM) agar plates were prepared as recommended by WormBook (Eisenmann, 2005). Liquid agar was prepared as 2% agar, 50 mM NaCl and 0.25% peptone and sterilised by autoclaving at 120˚C for 20 minutes. The agar was allowed to cool to approximately 50˚C before being supplemented with sterilised 25 mM KPO4 pH 6.0, 1 mM $CaCl_2$, 1 mM MgSO4, 5 mg/mL cholesterol, and 200 µg/mL streptomycin (Chaudhuri, Parihar and Pires-daSilva, 2011).

NGM-FUdR plates have the addition of 5'-fluorodeoxyuridine (FUdR) to a final concentration of 50 µM which blocks reproduction in *C. elegans,* allowing for synchronised populations during aging experiments. NMG-RNAi plates are prepared using a similar method, except 200 µg/mL streptomycin is replaced by 100 µg/mL ampicillin, and 1 mM isopropyl ß-d-1-thiogalactopyranoside (IPTG) is added (Conte *et al.*, 2015).

Plates were dispensed using a peristaltic pump (INTEGRA Biosciences) the quantity of liquid per plates were 3.5 mL per 3.5 mm, 10 mL per 60 mm, 30 mL 90 mm. For 24 well plates, 1.5 mL of liquid agar was dispensed per well. NGM plates were allowed to set and dry for two days before being seeded with bacteria,

NGM-RNAi plates were loosely covered with tin foil to protect from light degradation.

2.1.1 Preparation and Seeding of Bacterial Cultures

A starter culture of *E. coli* OP50-1 was obtained from the Caenorhabditis Genetics Center (CGC). RNAi clones were obtained from a C. elegans RNAi clone library, RNAi in the library consists of an *E. coli* HT115 (Kamath & Ahringer, 2003). Glycerol stocks were prepared by combining 600 µL bacterial stock with 300 µL filter-sterilised 60% Glycerol, the stock was mixed well and stored at -80°C.

Lysogeny broth (LB) was prepared by diluting 1% w/v tryptone, 0.5% w/v yeast extract, and 1% NaCl in ddH2O, and sterilising by autoclaving at 120˚C for 20 minutes. Glycerol stocks were transferred from -80°C storage on ice to prevent the stock thawing. A chunk of frozen stock was transferred into the required volume of LB using a sterile pipette tip and supplemented with antibiotics; 1 mg/mL streptomycin for *E. coli* OP50-1 cultures, and 1 mg/mL ampicillin for RNAi *E. coli* HT115 cultures under Bunsen burner. *E. coli* OP50-1 cultures were incubated for 16 hours at 37°C shaking at 180 rpm before being seeded onto NGM plates, 1 mM IPTG was added to RNAi *E. coli* HT115 cultures 3 hours before seeding to induce RNAi expression. The 35 mm plates were seeded with 80 µL of culture, 60 mm plates with 200 µL of culture, and 90 mm plates with five 200 µL lawns of culture. 24 well plates were seeded with 50 µL of culture per well. Once seeded, plates dried for 2-3 days before being transferred to 4°C for long term storage.

2.1.2 Preparation of liquid culture

For experiments where large quantities of *C. elegans* were required, the animals were cultured in liquid medium. This method requires highly concentrated OP50-1 *E. coli*, obtained by growing 500 mL of OP50-1 *E. coli* bacterial culture in LB for 16 hours at 37°C shaking at 180 rpm. Subsequently, 50 mL aliquots of culture were centrifuged at 4000 X G and the supernatant was disposed of. The falcon tube containing the pellet was inverted on a paper towel to remove any excess liquid, before being stored at -80°C and freeze thawed three times. Once complete, the pellet was resuspended in M9 buffer (22 mM KH_2PO_4, 42 mM Na_2HPO_4, 85 mM NaCl, 1 mM $MgSO_4$) in a volume equal to that of the pellet and stored at -20°C.

To set up the liquid cultures, 50 mL of sterilised M9 buffer was transferred to a 200 mL conical flask and supplemented with 50 µL 5 mg/mL cholesterol, 150 µL 1 M $MgSO_4$, 500 µL Nystatin, and 500 µL Penicillin Streptomycin Neomycin (PSN) under Bunsen flame. Three highly populated 90 mm plates of gravid adults were bleach synchronised (see 2.2.3). The resulting the axenized eggs were aseptically added to the liquid medium, with 3 mL of concentrated OP50-1 *E. coli*. The conical flask was covered with tin foil and incubated at 20°C shaking at 150 rpm.

For aging experiments, once the animals reach L4 stage, FUdR was added to the liquid culture at a final concentration of 50 µM to prevent reproduction. Liquid cultures were monitored daily for starvation by observing dauer stage animals and the opacity of a 10 µL drop of culture under a microscope. Food supplies were

replenished until the desired age was achieved, and animals were ready to be harvested.

To harvest liquid cultures, the 50 mL cultures were transferred to falcon tubes of the same volume and incubated on ice for 15 minutes, followed by 3-minute centrifugation at 900 xg at 4°C. The pellet was resuspended in 7 mL of M9 buffer and transferred to a 15 mL falcon tube. To separate *C. elegans* from bacteria, 7 mL of 50% sucrose was added to the culture and the centrifugation step was repeated. The top 3 mL layer of *C. elegans* was transferred to 11 mL of M9 buffer, and the pellet was washed 3 times in M9 buffer.

2.2 *C. elegans* strains and maintenance

2.2.1 *C. elegans* Strains and Genotypes

Some strains were provided by the CGC, which is funded by NIH Office of Research Infrastructure Programs (P40 OD010440). The JMK strains were kindly gifted by Janine Kirstein (The University of Bremen, Germany). Strains denoted PVH were generated by myself or other members of the van Oosten Hawle lab.

Strain Code	**Abbreviation in text**	**Genotype**
N2	N2	Wild-type
CL2006	MAβ$_{3-42}$	dvIs2 [pCL12(unc-54/human Abeta peptide 1-42 minigene) + pRF4]

		(Link, 1995)
i90	HSP-90^{int}	rmIs346[vha-6p::DAF-21::GFP] (van Oosten-Hawle, Porter and Morimoto, 2013)
n90	HSP-90^{neu}	rmIs345[F25B3.3p::DAF-21::GFP] (van Oosten-Hawle, Porter and Morimoto, 2013)
m90	HSP-90^{bwm}	rmIs347[unc-54p::DAF-21::GFP] (van Oosten-Hawle, Porter and Morimoto, 2013)
PVH50	MAβ$_{3-42}$::HSP-90^{bwm}	CL2006 x m90 (O'Brien *et al.*, 2018)
PVH85	MAβ$_{3-42}$::HSP-90^{neu}	CL2006 x n90 (O'Brien *et al.*, 2018)
PVH86	MAβ$_{3-42}$::HSP-90^{int}	CL2006 x i90 (O'Brien *et al.*, 2018)
GMC101	iMAβ$_{1-42}$	dvIs100 [unc-54p::A-beta-1-42::unc-54 3'-UTR + mtl-2p::GFP] (McColl *et al.*, 2012)
PVH217	iMAβ$_{1-42}$::HSP-90^{neu}	GMC101 x n90
PVH218	iMAβ$_{1-42}$::HSP-90^{int}	GMC101 x i90
PVH219	iMAβ$_{1-42}$::HSP-90^{bwm}	GMC101 x m90
CL2355	iNAβ$_{1-42}$	dvIs50 [pCL45 (snb-1::Abeta 1-42::3' UTR(long) + mtl-2::GFP] (Wu, 1995)
PVH164	iNAβ$_{1-42}$::HSP-90^{neu}	CL2355 x n90

JKM2	MAβ$_{1-42}$	*Is* [*rgef-1*p::Signalpeptide-Abeta(1−42)::*hsp-3*(IRES)::wrmScarlet-Abeta(1−42)::*unc-54*(3'UTR) + *rps-0*p::HygroR] (Gallrein *et al.*, 2021)
JKM3	MC	*Is* [*rgef-1*p::wrmScarlet::*unc-54*(3'UTR) + *rps-0*p::HygroR] (Gallrein *et al.*, 2021)
JKM7	NAβ$_{1-42}$	Is [myo-3p::Signalpeptide-Abeta(1−42)::hsp-3(IRES)::wrmScarlet-Abeta(1−42)::unc-54(3'UTR) + rps-0p::HygroR] (Gallrein *et al.*, 2021)
JKM8	NC	Is [myo-3p::wrmScarlet-Abeta::unc-54(3'UTR) + rps-0p::HygroR] (Gallrein *et al.*, 2021)
PVH255	MAβ$_{1-42}$::HSP-90^{bwm}	JMK2 x m90
PVH256	MAβ$_{1-42}$::HSP-90^{neu}	JMK2 x n90
PVH257	MAβ$_{1-42}$::HSP-90^{int}	JMK2 x i90
PVH258	MC::HSP-90^{bwm}	JMK3 x m90
PVH259	MC::HSP-90^{neu}	JMK3 x n90
PVH260	MC::HSP-90^{int}	JMK3 x i90
PVH261	NAβ$_{1-42}$::HSP-90^{bwm}	JMK7 x m90
PVH262	NAβ$_{1-42}$:: HSP-90^{neu}	JMK7 x n90
PVH263	NAβ$_{1-42}$::HSP-90^{int}	JMK7 x i90
PVH264	NC::HSP-90^{bwm}	JMK8 x m90
PVH265	NC:: HSP-90^{neu}	JMK8 x n90
PVH266	NC::HSP-90^{int}	JMK8 x i90

NL3321	sid-1	sid-1 (pk3321) (Winston, Molodowitch and Hunter, 2002)
PS3551	hsf-1 (sy441)	hsf-1 (sy441) (Hajdu-Cronin, Chen and Sternberg, 2004)
AM994	hsp-90^{control}	sid-1 (pk3321); rmIs288 (myo-2p::CFP; C12C8.1p::mCherry) (van Oosten-Hawle, Porter and Morimoto, 2013)
PVH1	hsp-90^{neu}	sid-1 (pk3321); rmIs288 (myo-2p::CFP; C12C8.1p::mCherry); pccIs001 (rgef-1p::daf-21 RNAi::unc-54 3'-UTR) (Miles *et al.*, 2023)
PVH2	hsp-90^{int}	sid-1 (pk3321); rmIs288 (myo-2p::CFP; C12C8.1p::mCherry); pccIs002 (vha-6p::daf-21 RNAi::unc-54 3'-UTR) (Miles *et al.*, 2023)
PVH184	hsf-1::hsp-90^{control}	hsf-1 (sy441) x AM994 (Miles *et al.*, 2023)
PVH190	hsf-1::hsp-90^{int}	hsf-1 (sy441) x PVH2 (Miles *et al.*, 2023)
PVH192	hsf-1::hsp-90^{neu}	hsf-1 (sy441) x PVH1 (Miles *et al.*, 2023)
AM722	Systemic Control	rmIs288 (myo-2p::CFP; C12C8.1p::mCherry) (Miles *et al.*, 2023)

PVH171	Muscle Specific RNAi	sid-1 (pk3321); rmIs288 (myo-2p::CFP; C12C8.1p::mCherry); pccIs002 (vha-6p::daf-21 RNAi::unc-54 3'-UTR); pccIs005 (myo-3p::SID-1::unc-54 3'UTR; myo-2p::RFP) (Miles *et al.*, 2023)
PVH172	Intestine Specific RNAi	sid-1 (pk3321); rmIs288 (myo-2p::CFP; C12C8.1p::mCherry); pccIs002 (vha-6p::daf-21 RNAi::unc-54 3'-UTR); pccIs004 (vha-6p::SID-1::unc-54 3'UTR; myo-2p::RFP) (Miles *et al.*, 2023)

Table 1. List of C. elegans strains used throughout this thesis and their corresponding genotypes.

2.2.2 Strain Maintenance and Storage

Strains were maintained in a temperature-controlled room at 20ºC, prior to opening plates, the microscope and working area were cleaned with 70% ethanol, and strains were maintained under Bunsen flame. Plates were viewed using a Microtec light microscope or a Leica MDG41 fluorescence microscope. For maintenance plates, 5-10 L1 animals possessing the desired phenotype were moved onto a fresh 60 mm NGM agar plate seeded with OP50-1 *E. coli*, and sealed with parafilm to avoid contamination. Strains were stored in a 20°C incubator, for no longer than 3 months to avoid cryptic suppressor mutations.

For long term storage, strains were stored in duplicate at -80°C. The strain to be frozen was allowed to populate two 90 mm plates, until the plate is occupied with freshly starved L1-L2 stage animals. The worms are washed off the plates using M9 into 1.8 ml cryotube vials and centrifuged for 1-minute at 1000 rpm at 4°C. The washing step is repeated two more times to remove all bacteria from the stock. Freezing solution is made up of 1 M NaCl, 50 mM KH_2PO_4 pH 6.0, 30% glycerol and sterilized by autoclaving at 120°C for 20 minutes. Subsequently, 30 µL of sterilized 1 M $MgSO_4$ is added per 100 mL of freezing solution. Once pelleted, the supernatant is disposed of, and 1 mL of freezing solution is added to each cryotube vial. The tube is gently inverted, and 500 µL is transferred into a clean cryotube vial. Subsequently, the tubes are sealed and wrapped in multiple layers of paper roll and stored in the -80°C freezer. The paper roll provides insulation to gradually decrease the temperature allowing for maximum survival. One vial is test thawed to measure survival.

2.2.3 Population Synchronisation and Aging

Every experiment in this work required *C. elegans* of a specific or known age. Population synchronisation was accomplished by one of two methods, bleaching or egg lay (Porta-de-la-Riva *et al.*, 2012). Bleach solution (0.3 M NaOH, 5% solution of sodium hypochlorite) was made fresh each time. One healthy young gravid adult can store 10-15 eggs in its uterus at any given time. This was used as a rough calculation as to how many worms were needed to produce enough worms for the planned experiment. Plates populated with non-starved young gravid adults, were washed off using sterile M9 into 15 mL falcon tubes. *C.*

elegans were pelleted at 1000 xg for 1 minute. The supernatant was disposed of, and 10 mL of bleach solution was added to each falcon tube. Subsequently, the tubes were shaken vigorously for approximately 5 minutes. During this time, the tubes were checked under a microscope periodically to monitor breakdown of the adult carcasses. Once breakdown began, the eggs were centrifuged at 1000 xg for 2 minutes. The bleach solution supernatant was disposed of, and 14 mL of M9 was immediately added to each falcon tube. This washing step was repeated 3 times, and in the final step 4 mL of M9 was added to each tube. The contents of each tube were transferred to separate wells of a 6-well plate, and moved to an orbital shaker at 20°C and 90 RPM overnight. The following morning, the 6-well plates were checked under a microscope to assess if eggs have hatched. If successful, the number of L1-stage animals per 1 μL was calculated and the intended number of worms was pipetted onto each NGM agar plate under a Bunsen burner; the date and stage were noted on the plate.

Strains with HSP-90 knock-down genotype (utilised in Chapter 5) and extrachromosomal intestinal HSP-90 over-expression strains (i90, PVH257, PVH260, PVH263, and PVH266) (utilised in Chapter 1), were sensitive to bleaching; therefore egg laying synchronisation was used for these strains. An appropriate number of young gravid adults were moved to a new NGM agar plate and left to lay eggs for 4-6 hours. Once the correct number of eggs were laid, the mothers were removed from the plate. The eggs were left to hatch for 12 hours and checked under a microscope, and the stage and date were noted on the plate.

2.2.4 Crossing Strains and Generating Males

Crossing is achieved by mating two strains together. Males are required to mate with hermaphrodite *C. elegans*, but only appear spontaneously in 0.2% of the population (Rose and Baillie, 1979). To generate males at a higher incidence three 60mm plates of ten L4 hermaphrodites were subjected to heat shock at 35˚C for 3.5 hours. Males were generated from the strain least sensitive to heat stress. The subsequent progeny were checked daily for males. If the incidence of males is too low, a self-cross was set up with the available males and a low number of hermaphrodites of the same strain. Eggs fertilised by mating with a male have an equal probability of being hermaphrodite or male, quickly increasing the male population.

To start a cross, two-four L4 hermaphrodites and seven-ten males were allowed to mate on a 35mm plate. Males were removed before the progeny reach L4 stage to prevent cross breeding. Hermaphrodite progeny were selected by marker mutations for both parent strains. In this work fluorescent co-injection markers were used exclusively, except for Maß$_{3\text{-}42}$ animals which uses the *rol-6* marker and displays a Roller phenotype. Wild-type animals move in a sinusoidal wave pattern, the roller phenotype effects organismal morphology causing animals to twist into a right-handed helix around their long axis (Kramer *et al.*, 1990). Five L4 hermaphrodite F1 progeny were selected and isolated into individual wells of 24-well plates. The F_1 progeny were allowed to self-fertilise until the F_2 progeny reached L4-stage. At this point, forty-four L4-stage F_2 progeny were selected and isolated into individual wells of 24-well plates and allowed to self-fertilise. Three

days later, the resulting progeny were checked for phenotype homozygosity. Homozygous F_3 progeny were monitored for multiple generations, once confirmed multiple vials of the new strain were frozen at -80˚C.

2.2.5 Avoiding Cryptic Mutations

The knockdown of *hsp-90* gene diminishes the buffering capacity against cryptic mutations in *C. elegans* resulting in the manifestation of altered phenotypes. The HSP-90 family is deemed an essential gene for the development of *C. elegans* and plays an important role in slowing mutations (Yahara, 1999). Previous members of the van Oosten-Hawle lab noted the HSP-90 knockdown strains accumulate cryptic mutations, affecting the observed phenotypes and obscuring interpretations. To decrease the prevalence of mutations, the strain was backcrossed into the genetic background, the *sid-1 (pk3321)* mutant strain, ten times prior to phenotype analyses.

Chapter 3. Transcellular Chaperone Signalling Regulates Organismal Proteostasis and Protects Against Aβ1-42 Protein Toxicity in Muscle and Neurones

3.1 Introduction

3.1.1 Proteostasis and Amyloid in *C. elegans*

Numerous chaperones are associated with the expression of amyloidogenic proteins in the *C. elegans* model. Several *C. elegans* amyloid models have been developed, in which the organisms express amyloidogenic proteins either systemically or in specific tissues, with distinct mutations and lengths tailored to the specific disease being modelled. These models include Aß and tauopathy models to study Alzheimer's disease, polyglutamine (polyQ) models to mimic Huntington's disease and spinocerebellar ataxias, and α-synuclein (α-Syn) models designed to explore Parkinson's disease. Analysis of gene expression in *C. elegans* has revealed that multiple genes associated with the proteostasis network exhibit upregulation in response to the presence of amyloidogenic proteins. For instance, there are 67 upregulated genes, including αB-crystallin (CRYAB) and tumour necrosis factor-induced protein 1 (TNFAIP1) in a *C. elegans* AD model (Link, 2003). An RNAi screen using an AD and a polyQ disease model, encompassing all chaperone genes in *C. elegans*, revealed a core set of 7 chaperone genes that function as suppressors of amyloid-associated toxicity in both models including

both *hsc-70* and *hsp-90* (Brehme *et al.*, 2014). RNAi screens performed in *C. elegans* α-Syn models identified genes that act as modifiers of disease, which are involved in various cellular processes, such as the ubiquitin proteasome system (UPS), the endocytic pathway, protein quality control within the ER/Golgi complex, and mitochondrial function (Vartiainen *et al.*, 2006; Kuwahara *et al.*, 2008; Van Ham *et al.*, 2008).

Two members from the HSP-70 family and three sHSPs related to αB-crystallin interact with intracellular Aß and HSP-16 colocalizes with intracellular Aß aggregates and, when over-expressed, partially mitigates Aß toxicity (Fonte *et al.*, 2002, 2008). Protein misfolding and aggregation induced stress responses in *C. elegans* disease models can be regulated cell-non-autonomously, meaning genes can affect processes outside of the cells they are expressed. Expressing HSP-90 in either neurones or the intestine of MAß$_{3-42}$, an AD disease model wherein Aß$_{3-42}$ is expressed in the body wall muscle of *C. elegans,* can alleviate the toxic paralysis phenotype associated with this strain (O'Brien *et al.*, 2018). This finding underscores the potential of transcellular chaperone signalling in ameliorating protein aggregation in *C. elegans*.

Nematodes possess a disaggregase complex that is composed of HSP-110, HSP-70, and J-proteins and influence polyQ aggregation in a *C. elegans* model (Nillegoda *et al.*, 2015). The simultaneous knock down of class A and B J-proteins in this model promotes the aggregation of polyQ synergistically, suggesting a collaborative effort between these J-proteins to slow aggregation (Kirstein *et al.*, 2017). Furthermore, knocking down *hsp-110* or *hsp-1* promotes aggregation in several polyQ models, and reproduced in neural cells derived from Huntington's

disease patients, where the over-expression of a J-protein, specifically DNAJB1, resulted in a reduction of polyQ aggregation (Scior *et al.*, 2018).

Subjecting a *C. elegans* AD model expressing $A\beta_{1-42}$ in the neurones to heat shock reduced the $A\beta_{1-42}$ aggregation and toxicity (Wu *et al.*, 2010). Furthermore, expressing polyQ in the *hsf-1(sy441)* mutant, a loss-of-function point mutation in the *hsf-1* gene that inhibits the transcriptional activity of HSF-1, increased the aggregation propensity of polyQ (Teixeira-Castro *et al.*, 2011). Furthermore, expressing polyQ in *C. elegans* strains with mutations in the AFD thermosensory neurones simultaneously inhibited the HSR and suppressed polyQ aggregation (Prahlad and Morimoto, 2011). Taken together, these studies indicate an interplay between the HSR and amyloid aggregation in *C. elegans*.

3.1.2 TCS is Activated by Tissue-Specific HSP-90 Over-expression

Under non-stressful conditions, HSP-90 is ubiquitously expressed in all tissues of *C. elegans*, and undergoes a HSF-1 dependent upregulation when the organism is subjected to heat stress (Miles *et al.*, 2023). When the HSP-90 client protein myosin heavy chain B (UNC-54) is mutated, myosin misfolds and causes a disruption to the thick filaments, simultaneously causing motility defects and HSP-90 upregulation at permissive temperatures. Despite the demand for chaperones being muscle-specific within these strains, HSP-90 upregulation extends beyond the body wall muscle, also occurring in tissues where UNC-54 is not expressed, namely the pharynx, intestine, and excretory cells. Conversely, when HSP-90 is over-expressed in neurons or the intestine, it induces a cell-non-autonomous upregulation of HSP-90 in the pharynx and body wall muscle,

thereby rescuing muscle organization in strains carrying mutated UNC-54 (van Oosten-Hawle, Porter and Morimoto, 2013).

In a *C. elegans* AD model of expressing the Aβ$_{3-42}$ in body wall muscle (MAβ$_{3-42}$), the over-expression of HSP-90 in neurons or the intestine results in reduced levels of Aβ$_{1-42}$ aggregation and reduced toxic phenotypes (O'Brien *et al.*, 2018). Indicating that cell-non-autonomous upregulation of HSP-90 via transcellular chaperone signalling can offer protection against amyloid aggregation within muscle tissues. However, it's worth noting that while tissue-specific HSP-90 over-expression proves beneficial with regard to enhancing the cell-non-autonomous protein folding environment, it reduces the organism's resilience to heat stress (van Oosten-Hawle, Porter and Morimoto, 2013). This cell-non-autonomous HSP-90 upregulation suppresses the transcription activity of HSF-1, resulting in a reduced organism-wide expression of chaperones such as HSP-70, and HSP-16. Additionally, HSP-90 upregulation preventing the expression of HSP-70p::mCherry under heat stress conditions. Consequently, the organism become less responsive to heat shock, being detrimental to organismal health and longevity (van Oosten-Hawle, Porter and Morimoto, 2013).

To understand the mechanisms by which cell-non-autonomous signalling could occur, a fundamental question is how cells communicates with each other. Notably, the transcellular upregulation of HSP-90 observed with tissue-specific HSP-90 over-expression is not HSF-1 dependent as observed in the canonical HSR. Instead, this phenomenon is contingent on the transcription factor PHA-4, which plays a crucial role in pharyngeal development and is upregulated in

strains exhibiting tissue-specific HSP-90 over-expression (van Oosten-Hawle, Porter and Morimoto, 2013).

During the early stages of development PQM-1 is primarily localized within the nucleus of intestinal cells of wild-type animals. Under normal conditions, once the animal reaches reproductive adulthood, PQM-1 translocates to the cytoplasm. However, this is circumvented when HSP-90 is over-expressed in neurons or the intestine, resulting in PQM-1 remaining within intestinal nuclei of adult *C. elegans*. The cell-non-autonomous upregulation of HSP-90 is dependent on PQM-1 following tissue-specific HSP-90 over-expression and operates within the specific tissue where HSP-90 is over-expressed (O'Brien *et al.*, 2018).

Although PQM-1 is essential for the upregulation of HSP-90 during heat stress, it does not directly regulate HSP-90 at the transcriptional level, implying the involvement of other downstream factors (O'Brien *et al.*, 2018). When HSP-90 is over-expressed in neurons, PQM-1 facilitates the upregulation of the CUB domain protein CLEC-41, which is neuronally required for cell-non-autonomous HSP-90 upregulation (O'Brien *et al.*, 2018). TCS activated by neuron-specific HSP-90 over-expression is augmented by glutamatergic signalling but suppressed by serotonergic or octopaminergic signalling. Conversely, when HSP-90 is over-expressed in the intestine, PQM-1 promotes the upregulation of the immune protein ASP-12, which is essential for cell-non-autonomous HSP-90 upregulation within the intestine (O'Brien *et al.*, 2018). The specific factors involved depend on the tissue in which HSP-90 is over-expressed (Figure 12).

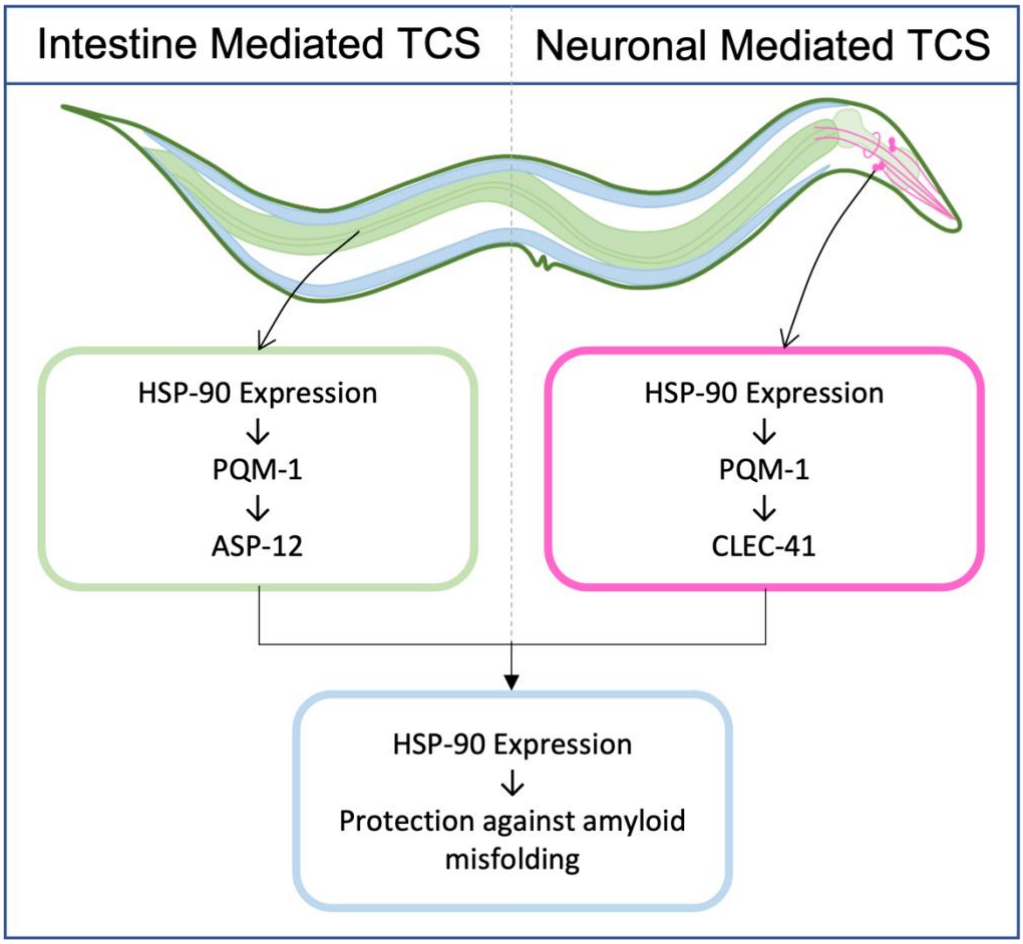

Figure 12. A schematic depicting the pathways of intestine and neuronal mediated TCS in AD *C. elegans* model MAß$_{3-42}$

3.2 Overview of Aims

Previous research outlining how over-expressing HSP-90 protects animals expressing intracellular Aß$_{3-42}$ in the body wall muscle by PQM-1 mediated TCS has been done in an outdated model, with low clinical relevancy to AD. In order to observe if PQM-1 mediated TCS is active in *C. elegans,* models expressing Aß$_{1-42}$ in the body wall muscle or mutants over-expressing HSP-90 in the same or distal tissues to Aß$_{1-42}$ were generated. The phenotypes of these animals were observed to see if HSP-90 over-expression rescued defects in the motility, lifespan,

fecundity, or chemotaxis of these animals. These experiments were done with the aim of elucidating a pathway of HSP-90-induced TCS in the future.

3.2 Materials and Methods

3.2.1 Motility Assays

Strains which exhibit muscular intracellular amyloid aggregation were subjected to paralysis assay to assess motility defects. For each strain, 25 L4-stage animals were picked onto four new 60 mm NGM agar plates. The subsequent day (Day 1), paralysis was analysed based on movement, pharyngeal pumping, and a touch-nose response using a platinum wire pick. The number of moving, paralysed, and censored animals was noted for each biological replicate. Moving animals were transferred to a new 60 mm plate, and the process was repeated every day until Day 8.

Strains which exhibit muscular extracellular amyloid aggregation were subjected to thrashing assay to assess motility defects. For each strain, a single animal was transferred to 200 µL of sterilized M9 on a glass slide. The nematode was left to thrash for 30 seconds before counting begins. Subsequently, the body bends were counted with a finger counter for another 30 seconds. This process was completed for 30 individual animals for a complete biological replicate; three biological replicates were assessed in total. This assay was done at timepoints Day 1, Day 4, and Day 7.

3.2.2 Chemotaxis Assay

Strains which exhibit neuronal amyloid aggregation were subjected to a chemotaxis assay to assess olfactory defects. In the case of iNAβ$_{1-42}$, and strains with this genetic background, L4-staged animals were subjected to a temperature upshift to 25°C which was maintained throughout the experiment. All other strains are assayed at 20°C. For each strain, Day 1 nematodes were washed off plates using M9 into 15 mL falcon tubes. The strains were washed 3 times and starved in clean M9 for 1 hour prior to the assay.

Unseeded 90 mm plates were split into quadrants on the underside of each plate, using a permanent marker. Four odorant spots were marked, a 1 cm diameter circle was marked around the odorant spots, and each odorant spot was supplemented with 1 µL of 1 M NaN_3. Once dry 1 µL of 99% EtOH was applied to the two control odorant spots, and 1 µL of 0.1% Benzaldehyde is applied to the final two experimental odorant spots (Figure 13A). For one biological replicate, 100 starved Day 1 nematodes were pipetted onto the centre of the plate (Figure 13B) and incubated at the appropriate temperature for 1 hour. This was completed for three biological replicates. Subsequently, the plates were imaged using a NAVITAR 67X Adapter camera. Using the images, the number of worms at the control odorant spots and experimental odorant spots are counted (Figure 13C). The chemotaxis index is calculated using the equation in Figure 13D.

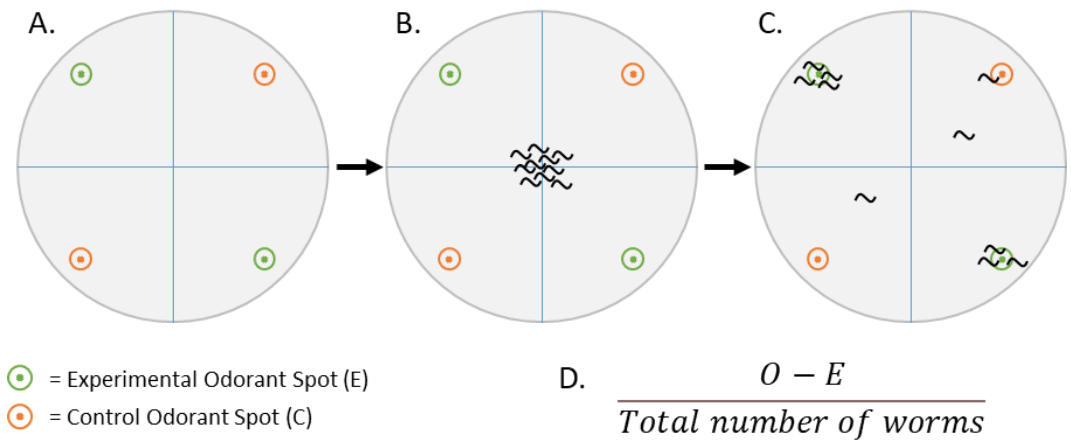

Figure 13. The Experimental Set Up for Chemotaxis Assays. (A) Experimental and control odorant spots were marked on 9 cm NGM agar plates, and supplemented with 1 µL of NaN_3, and 1 µL 0.1% Benzaldehyde (green) or 100% Ethanol (orange). (B) 100 starved nematodes were added to the centre of the plate, (C) an hour later the plate was imaged and (D) the chemotaxis index was calculated.

3.2.4 Offspring Assay

For one biological replicate, 10 L4 nematodes were isolated and transferred to a fresh NGM-agar 24-well plate daily. Every day, the number of eggs or L1 larvae in each well were counted until no more eggs were laid. Experiments were carried out in triplicate.

3.2.3 Lifespan Assay

For one biological replicate, 100 synchronised L4-staged nematodes were pipetted onto NGM-FUdR plates seeded with OP-50 *E. coli*; this was repeated in triplicate.

The plates were incubated at 20°C, and survival was scored every day for 30 days. Survival was measured by movement, pharyngeal pumping, and a touch-nose response using a platinum wire pick.

3.2.5 X-34 Staining and Confocal Microscopy

C. elegans were synchronised and aged to the relevant day of adulthood before being transferred into 500 µL of M9 buffer and washed three times in M9 buffer to remove residual bacterial contaminant. The animals were centrifuged, and the pellet was resuspended 1 mM X-34 dissolved in M9 buffer. Animals were incubated at 20°C for 2 hours on a rotator. Animals were washed three times in M9 buffer and transferred to a NGM agar plate and incubated at 20°C for 12-16 hours prior to imaging (excitation 400-410 nm, emission 455 nm).

Individual stained *C. elegans* were suspended in a drop of 5 mM levamisole on a 2% (w/v) agarose glass slide to anaesthetise the animal. Slides were left to dry for 2 minutes prior to a glass coverslip being placed on top of the slide. Images were taken of the slides using an upright Zeiss LSM880 laser scanning confocal microscope and Zen software. Images were taken at magnifications of 10X, 20X and 40X. Images were taken together for each experiment, and identical settings were used. Images were processed and analysed using ImageJ or Zen software.

3.3 Results

3.3.1 TCS Occurs in Untagged Amyloid Aggregation Models

The *C. elegans* AD models used in this work are abbreviated to NAß and MAß, indicating neuronal and muscle Aß expression respectively. The *C. elegans* AD model expressing untagged, truncated, $A\beta_{3-42}$ in the body wall muscle ($MA\beta_{3-42}$), was utilised in previous work exploring the connections between amyloid and transcellular chaperone signalling (O'Brien *et al.*, 2018). The human $A\beta_{1-42}$ peptide in the $MA\beta_{3-42}$ strain undergoes an unintentional truncation event resulting in the model expressing $A\beta_{3-42}$. Despite this, the $MA\beta_{3-42}$ model was originally selected over the temperature permissive $iMA\beta_{1-42}$ model to study TCS and the regulators of organismal proteostasis in *C. elegans*. This was attributed to *C. elegans* being highly sensitive to temperature change, thus strictly controlling this element is pivotal when investigating the regulation of heat shock proteins (van Oosten-Hawle, Porter and Morimoto, 2013; O'Brien *et al.*, 2018).

Investigating *in situ* aggregation and protein structure of $A\beta_{1-42}$ is more impactful and clinically relevant than $A\beta_{3-42}$, as $A\beta_{1-40}$ and $A\beta_{1-42}$ are the predominant amyloid forming peptides in AD. Additionally, the $MA\beta_{3-42}$ model is reported to exhibit accelerated aggregation propensity which could complicate interpretations drawn from data regarding aggregation location, plaque size, and the progression of fibrillization (McColl *et al.*, 2009).

The pathway by which over-expressing HSP-90 in the neurones or intestine initiates TCS resulting in a protective effect against $A\beta_{3-42}$ in the muscle has been

described previously (O'Brien *et al.*, 2018). However, it was unknown if over-expressing HSP-90 in distal tissues would be protective against Aß$_{1-42}$ in the muscle or neurones, or if PQM-1 dependent TCS would regulate any protective effects observed.

3.3.1.1 TCS has a protective effect in the body wall muscle when the signal sent from distal tissues

To confirm the previous observations seen in *C. elegans* expression the truncated version of Aß$_{1-42}$ (MAß$_{3-42}$ model), the motility was assessed and compared to N2 wild-type animals. The MAß$_{3-42}$ model exhibited an age-induced paralysis phenotype in 66% of the animals compared to N2 wild-type (Figure 14A, B). The paralysis phenotype was reduced in MAß$_{3-42}$ animals expressing HSP-90 in the body wall muscle, intestine, or neurones aligning with published data (Figure 14A, B) (O'Brien *et al.*, 2018).

To explore if over-expressing HSP-90 in strains expressing full length Aß$_{1-42}$ initiated TCS to protect against toxic amyloid phenotypes, the motility of the temperature permissive strain iMAß$_{1-42}$ was assessed. The iMAß$_{1-42}$ model exhibits increased in paralysis in 81% of animals at Day 4 of adulthood compared to N2 wild-type when upshifted to 25°C (Figure 14C, D). Similar to MAß$_{3-42}$, over-expressing HSP-90 in the neurones, intestine, or body wall muscle decreased paralysis compared to iMAß$_{1-42}$ after 4 days (Figure 14C, D). Taken together these results strongly suggest that HSP-90 can protect against the toxic effects of Aß$_{1-42}$ aggregation when expressed in either the same or distal tissues, evidencing transcellular chaperone signalling in the iMAß$_{1-42}$ *C. elegans* AD model.

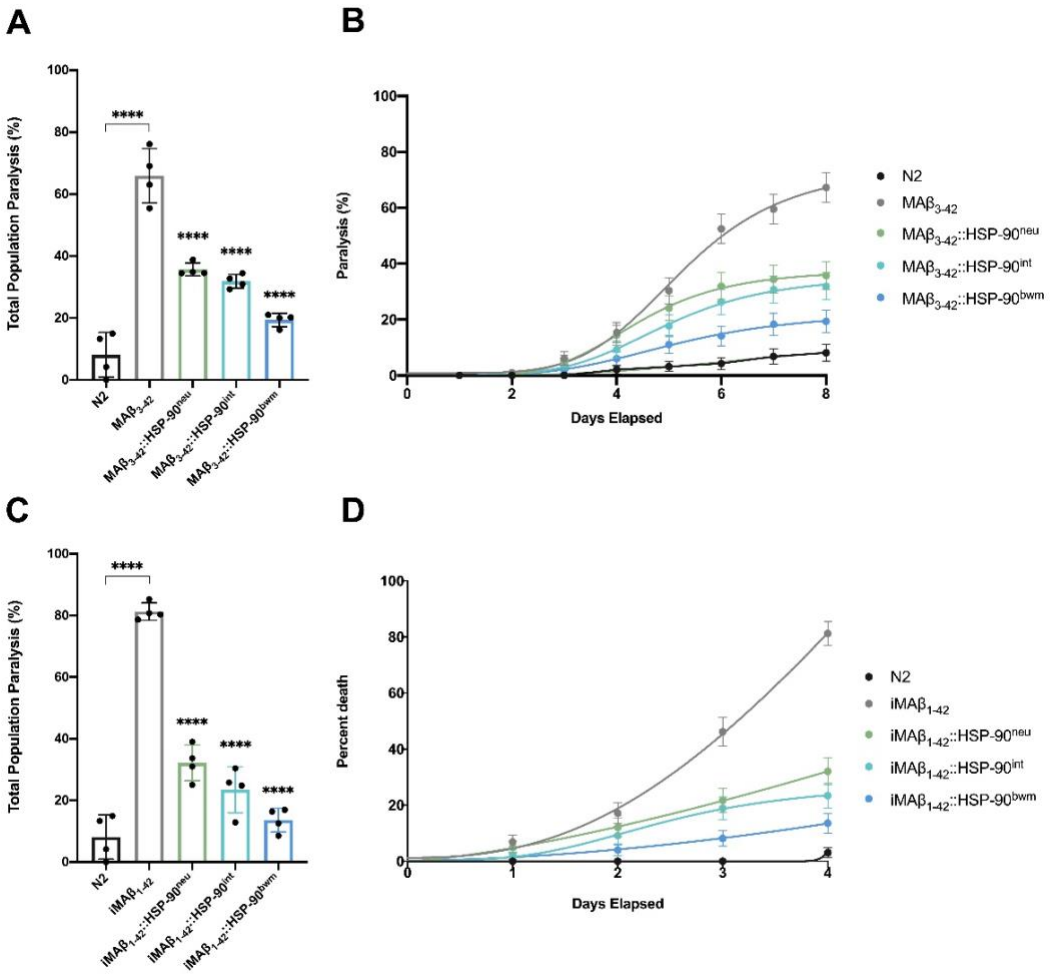

Figure 14. Over-expressing HSP-90 in distal tissues is protective against Aβ3-42 and Aβ1-42 in the body wall muscle of *C. elegans*. (A, B) Expressing Aß3-42 in the body wall muscle of *C. elegans* (MAß3-42) produces a paralysis phenotype which is rescued when expressing HSP-90 in the body wall muscle (MAß3-42::HSP-90bwm), neurones (MAß3-42::HSP-90neu), or intestine (MAß3-42::HSP-90int) of the animal. (C, D) Expressing Aß1-42 in the body wall muscle of *C. elegans* (iMAß1-42) produces a paralysis phenotype which is rescued when expressing HSP-90 in the body wall muscle (iMAß1-42::HSP-90bwm), neurones (iMAß1-42::HSP-90neu), or intestine (iMAß1-42::HSP-90int) of the animal. (A, C) Graphs represent the total population paralysis on the final day of scoring. (B, D) Graphs represent the population paralysis over time. (A – D)

Graphs represent 4 biological replicates of 25 animals per condition. Significance determined using one-way ANOVA * P < 0.05; ** P < 0.01; *** P < 0.001; **** P < 0.0001; ns = not significant. Error bars represent SEM of the 4 biological replicates.

3.3.1.2 TCS has a protective effect in the neurones when the signal sent from the intestine

Neuronal $A\beta_{1-42}$ aggregation in the $iNA\beta_{1-42}$ *C. elegans* model causes neurodegeneration, assessed by impaired chemotaxis and learning (Wu *et al.*, 2006). No data has been published evidencing TCS from distal tissues to the neurones in *C. elegans*, thus, the chemotaxis of these animals was used to explore if over-expressing HSP-90 in distal tissues of $iNA\beta_{1-42}$ caused a protective effect.

In accordance with published data, $iNA\beta_{1-42}$ shows a significant decrease in chemotaxis index in comparison to control (Figure 15) (Wu *et al.*, 2006). Within the neurones, over-expressing HSP-90 improves the chemotaxis of $iNA\beta_{1-42}$ animals. When HSP-90 is over-expressed in the intestine, there is a significant improvement in the chemotaxis ability of $iNA\beta_{1-42}$ animals, whereas over-expressing HSP-90 in the body wall muscle has no effect on the chemotaxis ability of $iNA\beta_{1-42}$ animals. It can be inferred that over-expressing HSP-90 in the intestine initiates TCS to the neurones resulting in a protective effect against $A\beta_{1-42}$.

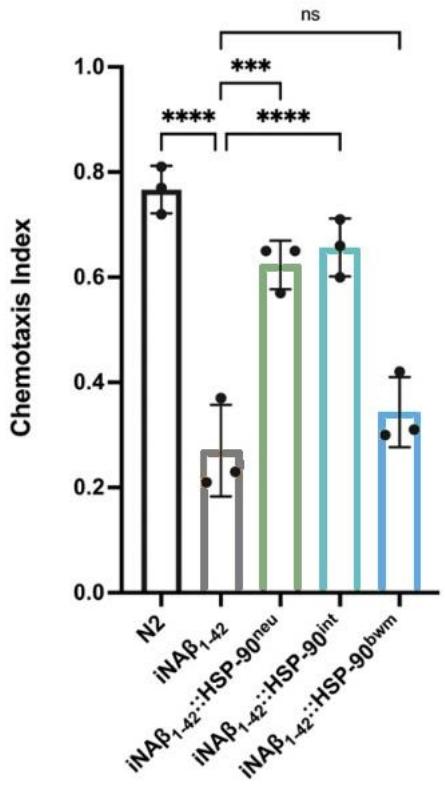

Figure 15. Over-expressing HSP-90 in the intestine initiates TCS to the neurones to protect against Aβ1-42 toxicity. Expressing Aß1-42 in the neurones of *C. elegans* (iNAß1-42) impairs the chemotaxis of the animal, which is rescued when over-expressing HSP-90 in the neurones (iNAß1-42::HSP-90neu) or intestine (iNAß1-42::HSP-90int). Graph represents 3 biological replicates of 100 animals per condition. Significance determined using one-way ANOVA * P < 0.05; ** P < 0.01; *** P < 0.001; **** P < 0.0001; ns = not significant. Error bars represent SEM of the 3 biological replicates.

3.3.1.3 Amyloid Aggregation can be Observed with X-34 Staining

X-34, a lipophilic, highly fluorescent derivative of Congo red binds to beta-sheet structures such as amyloid. The X-34 stain was used to locate Aß3-42 aggregates in the body wall muscle, or Aß1-42 in the body wall muscle or neurones of adult *C. elegans*. The MAß3-42 and iMAß1-42 *C. elegans* models were aged to Day 5 of

adulthood prior to staining, while iNAβ$_{1-42}$ animals were aged to Day 1 of adulthood. Confocal images were taken of individual animals and compared to N2 wild-type animals (Figure 16A).

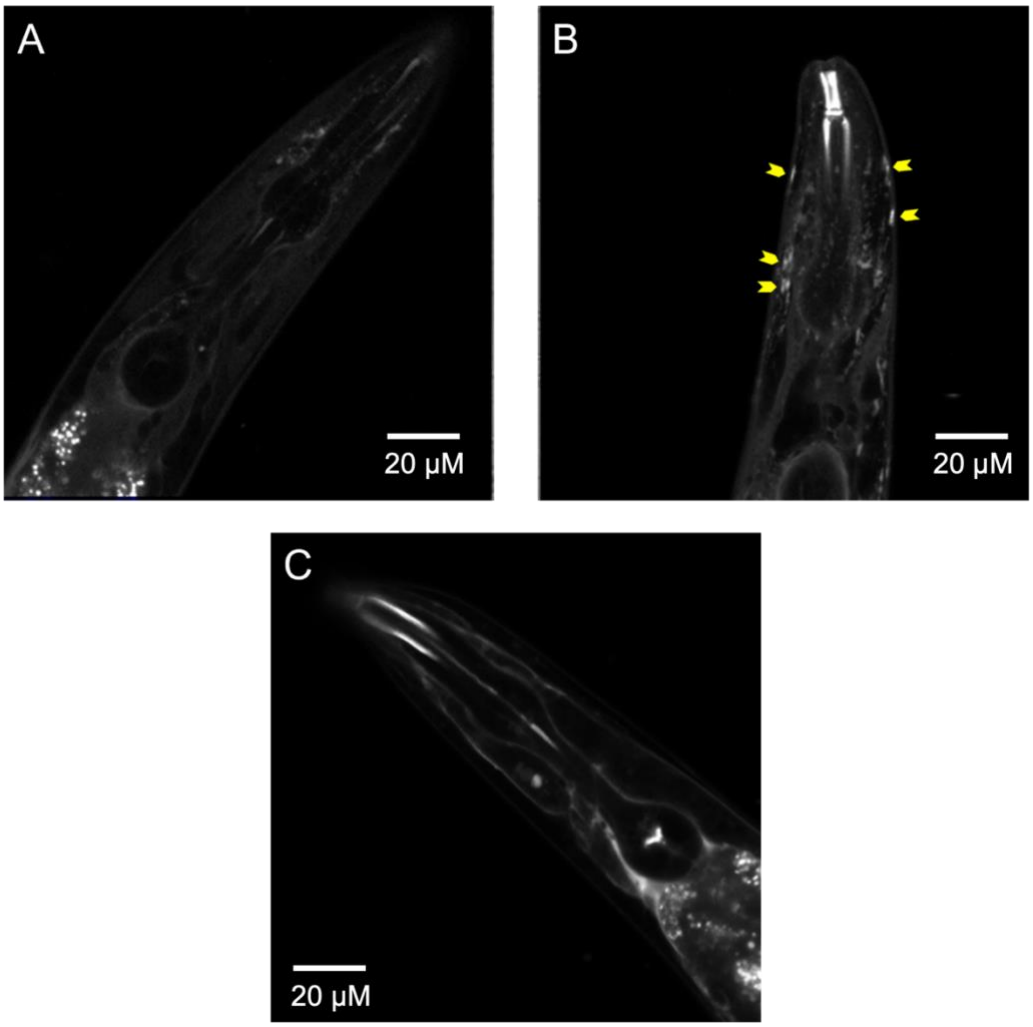

Figure 16. X-34 Staining of Aβ$_{1-42}$ expressing *C. elegans*. (A) N2 wild-type (B) iMAβ$_{3-42}$ and (C) iNAβ$_{1-42}$ animals stained with 1 mM of X-34 for 2 hours at Day 5 of adulthood. Fluorescence was observed by obtaining emission (excitation: 350 nm) and excitation (emission: 490 nm) spectra using Zeiss LSM880 with Airyscan Upright Confocal Microscope. 30 animals of each strain were imaged. Yellow arrows point to deposits in body wall muscle (B).

Upon X-34 staining, no amyloid aggregates were observed in N2 wild-type animals at Day 1 or Day 5 of adulthood (Figure 16A). Several amyloid deposits could be observed in the body wall muscle of the MAß$_{3-42}$ model (Figure 16B), however the same deposits could not be observed in iMAß$_{1-42}$ animals despite being previously successfully stained (McColl *et al.*, 2012). Additionally, X-34 staining of iNAß$_{1-42}$ animals was difficult to interpret due to non-specific binding of the stain clouding the interpretation. There is fluorescence in a small portion of the nerve ring (Figure 16C), however this could be non-specific binding of the stain in the intestinal tract of the nematodes.

3.3.2 Tagged Amyloid Aggregation in *C. elegans*

In 2021, novel Aß$_{1-42}$ pathology *C. elegans* models were published by the Kirstein lab which expressed Aß$_{1-42}$ in the body wall muscle (Figure 17A) and neurones (Figure 17B) of *C. elegans*. (Gallrein *et al.*, 2021). These strains offered significant advantages when compared to previously employed models.

Firstly, they allowed for sub-stoichiometric fluorescent tagging of Aß$_{1-42}$ fibrils using wrmScarlet, an mScarlet tag optimised for use in *C. elegans*. Secondly, they facilitated the study of extracellular Aß$_{1-42}$ aggregation-induced neurodegeneration and finally the expression of Aß$_{1-42}$ in the body wall muscle was not temperature permissible (Gallrein *et al.*, 2021). These undertakings had never been realised in *C. elegans*, marking a shift in the landscape of Aß$_{1-42}$ research within this model organism. These novel strains were more clinically relevant and offered the ability to observe unperturbed fibril growth with

fluorescent markers. For these reasons, the effects of over-expressing HSP-90 in distal tissues was done in these models.

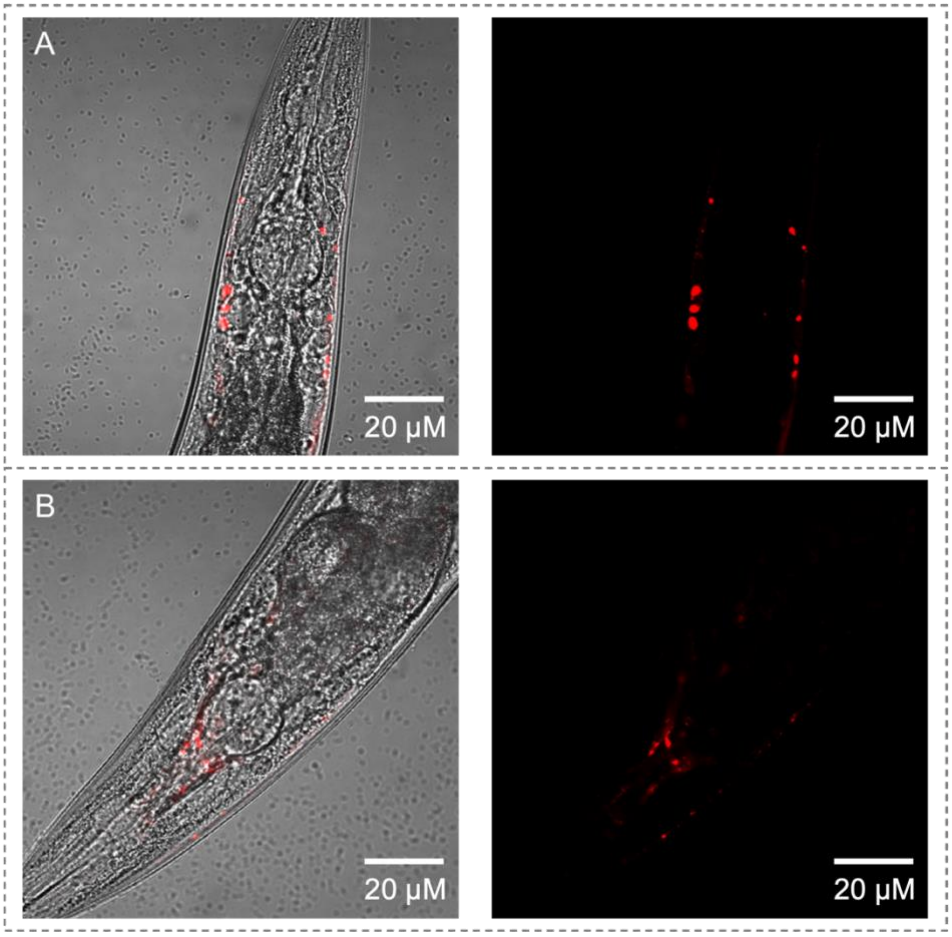

Figure 17. The localisation of fluorescently tagged Aβ$_{1-42}$ in *C. elegans*. Confocal Images of (A) MAß$_{1-42}$ and (B) NAß$_{1-42}$ at Day 5 of adulthood at 40 X magnification. Fluorescence was observed by obtaining emission (excitation: 587 nm) and excitation (emission: 610 nm) spectra using Zeiss LSM880 with Airyscan Upright Confocal Microscope. 30 animals of each strain were imaged.

3.3.2.1 Expressing HSP-90 in MAβ$_{1-42}$ and NAβ$_{1-42}$ Animals Reduces Motility Defects

The motility at of animals expressing Aß$_{1-42}$ extracellularly was assessed at Day 1 and Day 4 of adulthood. Initially, a paralysis assay revealed that while motility was clearly reduced, MAß$_{1-42}$ and NAß$_{1-42}$ animals do not exhibit a paralysis phenotype like seen in MAß$_{3-42}$ and iMAß$_{1-42}$ animals (Figure 15). This is likely due to the Aß$_{1-42}$ peptide aggregating extracellularly, and thus it was concluded that a paralysis assay would not be the best readout for motility defects in MAß$_{1-42}$ and NAß$_{1-42}$ *C. elegans* AD models. To circumvent this, a thrashing assay was utilised to measure the frequency of body bends per second, rather than total body paralysis (Figure 18).

Motility is decreased in MAß$_{1-42}$ animals at all time points compared to control. Unlike MAß$_{3-42}$ and iMAß$_{1-42}$, motility defects do not worsen with age indicating that cellular disruption caused by extracellular Aß$_{1-42}$ aggregation may not be caused by large amyloid deposits but rather by pre-amyloid aggregates. Expressing HSP-90 in the body wall muscle, intestine, or neurones of MAß$_{1-42}$ animals alleviates the motility defects observed at all time points (Figure 18A). This rescue phenotype could indicate that PQM-1-Mediated TCS observed in superseded *C. elegans* AD models is conserved in MAß$_{1-42}$ animals (O'Brien *et al.*, 2018).

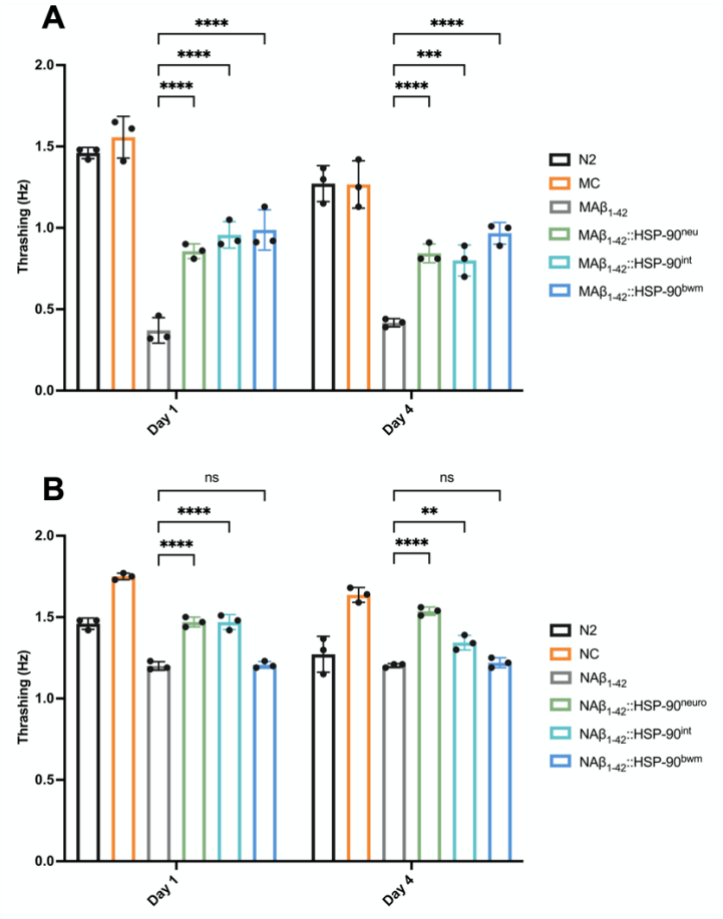

Figure 18. Over-expressing HSP-90 in the distal tissues of MAβ$_{1-42}$ and NAβ$_{1-42}$ animals ameliorates toxic Aβ$_{1-42}$ activity. (A, B) Expressing Aß$_{1-42}$ in the body wall muscle (MAß$_{1-42}$) or neurones (NAß$_{1-42}$) of *C. elegans* significantly decreases the motility of the animals at Day 1 or Day 4 of adulthood compared to control (MC and NC respectively). (A) Over-expressing HSP-90 in the same or distal tissues sees an significant improvement in the motility of MAß$_{1-42}$ animals. (B) Over-expressing HSP-90 in the neurones (NAß$_{1-42}$::HSP-90^{neu}) or intestine (NAß$_{1-42}$::HSP-90^{int}) of NAß$_{1-42}$ animals improves motility defects. Graphs represent 3 biological replicates of 30 animals per condition. Significance determined using one-way ANOVA * P < 0.05; ** P < 0.01; *** P < 0.001; **** P < 0.0001; ns = not significant. Error bars represent SEM of the 3 biological replicates.

Motility is similarly reduced in NAβ$_{1-42}$ animals compared to control. This motility is less severe than MAβ$_{1-42}$ animals, likely due to the indirect effect of motor neurone degeneration as a result of Aβ$_{1-42}$ aggregation in the neurones. Within the neurones, over-expressing HSP-90 in the neurones of NAβ$_{1-42}$ animals improves the motility defects at both Day 1 and Day 4 of adulthood (Figure 18B). Over-expressing HSP-90 in the body wall muscle of NAβ$_{1-42}$ animals does not rescue the defective motility phenotype at any timepoint. However, over-expressing HSP-90 in the intestine improves the motility of NAβ$_{1-42}$ animals at both Day 1 and Day 4 of adulthood. Taken together, these results indicate the presence of an undefined pathway wherein over-expressing HSP-90 in the intestine induces TCS to protect the neurones against Aβ$_{1-42}$ aggregation and to regulate organismal proteostasis in *C. elegans*.

3.3.2.2 Expressing HSP-90 in MAβ$_{1-42}$ and NAβ$_{1-42}$ Animals Increases Lifespan

Lifespan assays are often used as a readout for organismal fitness, as a prolonged lifespan is often an indicator of a functioning proteome. A lifespan assay was utilised to assess the impact of extracellular Aß$_{1-42}$ aggregation on the organismal health of *C. elegans*. Aggregation of Aß$_{1-42}$ in the body wall muscle of *C. elegans* significantly reduced the maximum lifespan by 8 days compared to control (Figure 19). Additionally, there was a significant drop in the median lifespan of MAß$_{1-42}$ animals of 5 days compared to control (Table 2). This indicates Aß$_{1-42}$ aggregation in the body wall muscle negatively affects organismal health.

Over-expressing HSP-90 in the body wall muscle, intestine, or neurones results in an increase in the maximum lifespan of MAß$_{1-42}$ animals. Furthermore, over-expressing HSP-90 in the body wall muscle (Figure 19C) or intestine (Figure 19B) increases the median lifespan of MAß$_{1-42}$ animals. However, there is no difference between the median lifespan when HSP-90 is over-expressed in the neurones (Figure 19A).

	MC	**MAβ$_{1-42}$**	**MAβ$_{1-42}$:: HSP-90^{bwm}**	**MAβ$_{1-42}$:: HSP-90^{neu}**	**MAβ$_{1-42}$:: HSP-90^{int}**
Median	16.5	11.5	14.5	12.5	13.8
Max	29.7	21.7	25.0	25.3	26.7

Table 2. Quantifying the MAβ$_{1-42}$ animal lifespan data. The Median and Maximum lifespan of MAß$_{1-42,}$ Control strains, and MAß$_{1-42}$ when HSP-90 is over-expressed in the body wall muscle, neurones, or intestine of the animal.

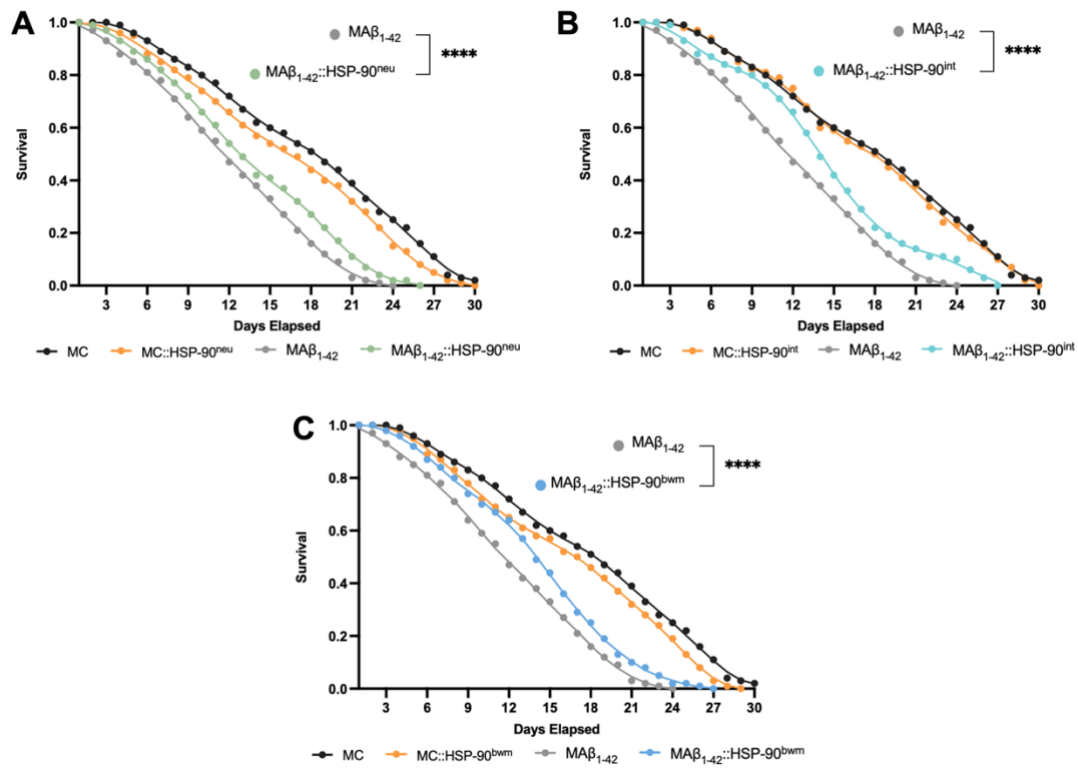

Figure 19. Over-expressing HSP-90 in the same or distal tissues as muscular Aβ$_{1-42}$ improves organismal fitness. (A-C) Expressing Aß$_{1-42}$ in the body wall muscle (MAß$_{1-42}$) of *C. elegans* decreases the lifespan of the animal. Over-expressing HSP-90 in the (A) neurones (MAß$_{1-42}$::HSP-90^{neu}), (B) intestine (MAß$_{1-42}$::HSP-90^{int}) or (C) body wall muscle (MAß$_{1-42}$::HSP-90^{bwm}), of MAß$_{1-42}$ animals improves lifespan and overall organismal health. (A – C) Graphs represent 4 biological replicates of 100 animals per condition, plotted points represent SEM of the 4 biological replicates. Significance determined using student t-test * P < 0.05; ** P < 0.01; *** P < 0.001; **** P < 0.0001; ns = not significant.

Expressing Aß$_{1-42}$ in the neurones of *C. elegans* decreases the maximum lifespan of the animal by 8.7 days compared to control (Figure 20, Table 3). The median lifespan of NAß$_{1-42}$ animals is reduced by 3.5 days compared to NC control (Figure 20, Table 3) indicating expressing human Aß$_{1-42}$ in the neurones negatively

impacts organismal health and longevity. Over-expressing HSP-90 in the neurones (Figure 20A) or intestine (Figure 20B) of NAβ1-42 animals improves the maximum lifespan by 2.7 and 4.7 days respectively (Table 3).

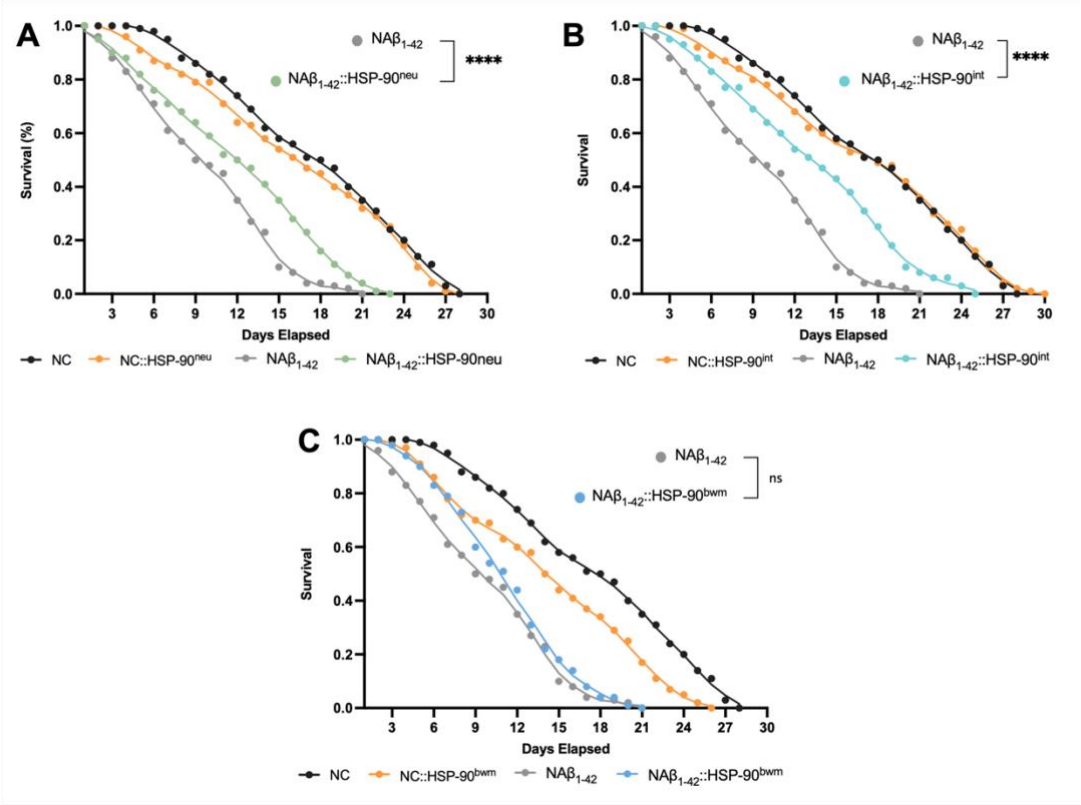

Figure 20. Over-expressing HSP-90 in the same or distal tissues as neuronal Aβ1-42 improves organismal fitness. (A-C) Expressing Aβ1-42 in the neurones (NAβ1-42) of *C. elegans* decreases the lifespan of the animal. Over-expressing HSP-90 in the (A) neurones (NAβ1-42::HSP-90neu), or (B) intestine (NAβ1-42::HSP-90int) of NAβ1-42 animals improves lifespan and overall organismal health. (A – C) Graphs represent 4 biological replicates of 100 animals per condition, plotted points represent SEM of the 4 biological replicates. Significance determined using student t-test * P < 0.05; ** P < 0.01; *** P < 0.001; **** P < 0.0001; ns = not significant.

	NC	NAβ$_{1-42}$	NAβ$_{1-42}$:: HSP-90^{bwm}	NAβ$_{1-42}$:: HSP-90^{neu}	NAβ$_{1-42}$:: HSP-90^{int}
Median	14.8	11.3	10.6	12.8	13.6
Max	29.3	20.6	20.6	23.3	25.3

Table 3. Quantifying the NAβ$_{1-42}$ animal lifespan data. The Median and Maximum lifespan of NAß$_{1-42,}$ Control strains, and NAß$_{1-42}$ when HSP-90 is over-expressed in the body wall muscle, neurones, or intestine of the animal.

However, over-expressing HSP-90 in the body wall muscle of NAß$_{1-42}$ animals has no effect on maximum lifespan (Figure 20C). Furthermore, when HSP-90 is over-expressed in the neurones (Figure 20A) or body wall muscle (Figure 20C) of NAß$_{1-42}$ animals, the median lifespan is unaffected. However, the median lifespan of NAß$_{1-42}$ animals is improved by 2.3 days when HSP-90 is over-expressed in the intestine (Figure 20B). Collectively, this data infers that over-expressing HSP-90 in the same or distal tissues as Aß$_{1-42}$ induces TCS to improve proteostasis, extend the lifespan and improve overall organismal health of *C. elegans* AD models. More work is required to elucidate the pathway regulating TCS, however, it could be hypothesised the PQM-1 mediated response is responsible for signalling within MAß$_{1-42}$ and NAß$_{1-42}$ animals. Furthermore, this data strengthens the hypothesis that a TCS pathway is present between the intestine and neurones of *C. elegans*. This unexplored intestine-to-neurone pathway highlights the potential role of the intestine in mediating cell nonautonomous stress responses, protecting *C. elegans*.

3.3.2.3 Expressing HSP-90 in MAβ$_{1-42}$ and NAβ$_{1-42}$ Animals Recovers Reduced Fecundity

Egg viability is an additional readout for organismal health, as well as being helpful information for planning experiments. Animals expressing Aß$_{1-42}$ in the body wall muscle laid less eggs (81.25) than control animals (298.12) (Figure 21A). Over-expressing HSP-90 in the neurones (136.1), intestine (172.42), and body wall muscle (196.28) significantly improves fecundity in MAß$_{1-42}$ animals (Figure 21A).

Animals expressing Aß$_{1-42}$ in the neurones laid less eggs (53.05) compared to control animals (261.25) (Figure 21B). When over-expressing HSP-90 in the neurones or intestine of NAß$_{1-42}$ animals, this toxic phenotype was alleviated, with mutants laying 173.92 and 224.98 eggs respectively (Figure 21B). Over-expressing HSP-90 in the body wall muscle of NAß$_{1-42}$ animals had no significant effect on fecundity (Figure 21B).

Confocal images (Figure 22) show older MAß$_{1-42}$ adults exhibit matriarchal hatching otherwise known as bagging; a behaviour described as eggs hatching within the parent. Bagging is usually a result of a low-nutrient, high-salt environment, however with these factors being controlled in this case bagging was likely a result of muscle impairment (Pickett and Kornfeld, 2013). Bagging was not observed in HSP-90 over-expression MAß$_{1-42}$ mutants. The systemic defects described here strengthens the hypothesis that over-expressing HSP-90 induces TCS in the *C. elegans* NAß$_{1-42}$ and MAß$_{1-42}$ AD models to protect organismal health. Furthermore, this data serves to strengthen the hypothesis regarding the

existence of an intestine-to-neuron TCS pathway, which plays a protective role in *C. elegans*.

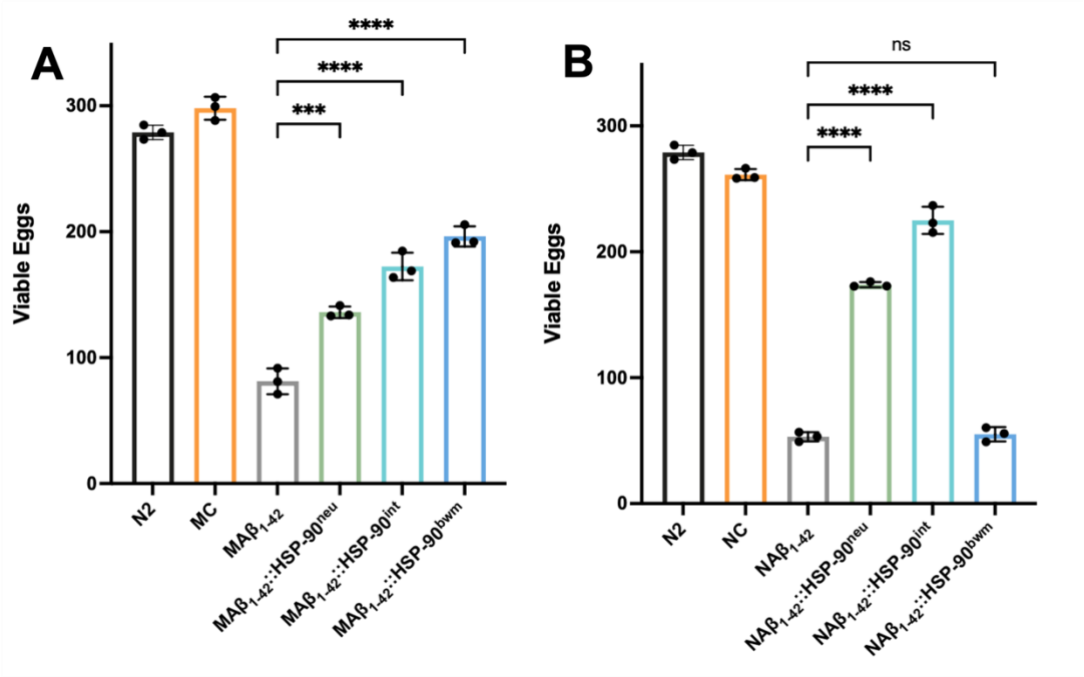

Figure 21. Over-expressing HSP-90 in the same or distal tissues rescuses reduced fecuntidy in NAβ$_{1-42}$ and MAβ$_{1-42}$ animals. (A) Expressing Aβ$_{1-42}$ in the body wall muscle of (MAβ$_{1-42}$) *C. elegans* decreases the number of viable eggs hatched by the animals. Over-expressing HSP-90 in the same or distal tissues improves the fecundity of MAβ$_{1-42}$ animals. (B) Expressing Aβ$_{1-42}$ in the neurones (NAβ$_{1-42}$) of *C. elegans* decreases the number of viable eggs hatched by the animals. Over-expressing HSP-90 in the neurones (NAβ$_{1-42}$::HSP-90^{neu}) or intestine (NAβ$_{1-42}$::HSP-90^{int}) improves the fecundity of NAβ$_{1-42}$ animals. Graphs represent 3 biological replicates of 10 animals per condition. Significance determined using one-way ANOVA * $P < 0.05$; ** $P < 0.01$; *** $P < 0.001$; **** $P < 0.0001$; ns = not significant. Error bars represent SEM of the 3 biological replicates.

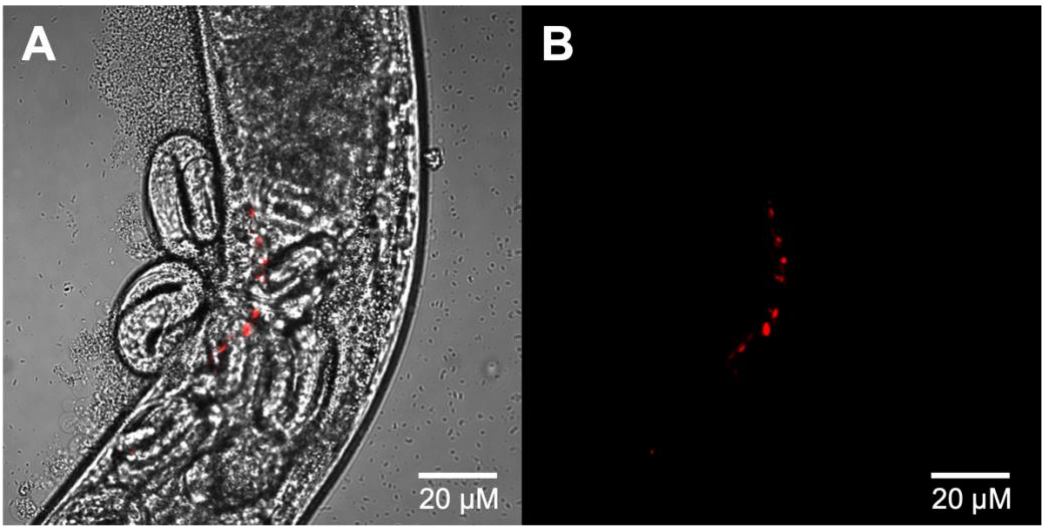

Figure 22. Bagging in MAβ$_{1-42}$ Day 5 adults. Confocal images of the MAß$_{1-42}$ *C. elegans* AD model at Day 5 of adulthood exhibiting matriarchal hatching or bagging indicating poor vulval muscular health. Fluorescence was observed by obtaining emission (excitation: 587 nm) and excitation (emission: 610 nm) spectra using Zeiss LSM880 with Airyscan Upright Confocal Microscope. 30 animals of each strain were imaged.

3.3.2.4 Expressing HSP-90 in MAβ$_{1-42}$ and NAβ$_{1-42}$ Animals Improves impaired chemotaxis

To investigate the protective effect of TCS against neurodegeneration, the chemotaxis of NAß$_{1-42}$ animals expressing HSP-90 in either the same or distal tissues was measured. Expressing Aß$_{1-42}$ in the neurones of *C. elegans* results in the chemotaxis index being impaired to 0.31 at Day 1 of adulthood compared to a chemotaxis index of 0.86 in control animals (Figure 23A). This indicates neuronal aggregation of Aß$_{1-42}$ causes neurodegeneration in adult *C. elegans*. Over-expressing HSP-90 in the neurones (Figure 23B) or intestine (Figure 23D) of

NAβ1-42 animals at Day 1 of adulthood restores the chemotaxis index to the same level as control. However, there is no improvement in chemotaxis index when HSP-90 is over-expressed in the body wall muscle of NAβ1-42 animals at Day 1 of adulthood (Figure 23C). The neurodegeneration observed indicates that over-expressing HSP-90 induces TCS in the *C. elegans* NAβ1-42 AD model to protect the neuronal health of the animal. Furthermore, this data acts to reinforce the hypothesis regarding the presence of an intestine-to-neuron TCS pathway, which plays a protective role in *C. elegans*.

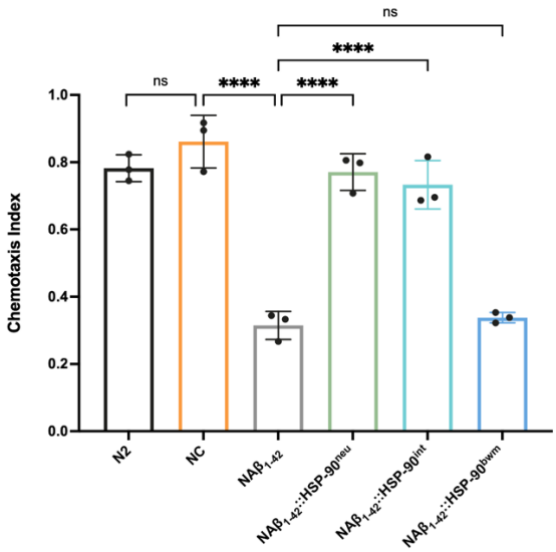

Figure 23. Over-expressing HSP-90 in the same or distal tissues as neuronal Aβ1-42 rescues chemotaxis impairment. (A) Expressing Aβ1-42 in the neurones of *C. elegans* (NAβ1-42) reduces the chemotaxis index of the animal compared to control (NC), which is rescued when HSP-90 is over-expressed in the (B) neurones (NAβ1-42::HSP-90^{neu}) and (D) intestine (NAβ1-42::HSP-90^{int}) of the animal. (A – D) Graphs represent 3 biological replicates of 100 animals per condition. Significance determined using one-way ANOVA * $P < 0.05$; ** $P < 0.01$; *** $P < 0.001$; **** $P < 0.0001$; ns = not significant. Error bars represent SEM of the 3 biological replicates.

3.4 Discussion

3.4.1 Temperature Permissive Strains

The MAß$_{3-42}$ *C. elegans* AD model expresses a truncated version of the Aß peptide, due to mis-cleavage of the signal peptide. iMAß$_{1-42}$ was therefore generated to express the full-length protein (McColl *et al.*, 2012). The iMAß$_{1-42}$ *C. elegans* AD model was paralysed by Day 4 of adulthood compared to N2 wild-type when upshifted to 25°C, while at 20°C no paralysis is observed (Figure 15C, D). This temperature upshift is also required for the iNAß$_{1-42}$ *C. elegans* AD model to express Aß$_{1-42}$ peptides in the neurones, which results in impaired chemotaxis at Day 1 of adulthood (Figure 15) (Wu *et al.*, 2006).

C. elegans are sensitive to temperature, and even within their physiological range, the nematodes undergo significant defence and metabolic response changes when the maintenance temperature fluctuates. Genes involved in the innate immune defence response are upregulated, while genes involved in metabolism are downregulated in *C. elegans* maintained at 25°C (Gómez-Orte *et al.*, 2018). Temperature dependent transcriptomic profiles makes the elucidation of pathways in strains which require temperature shifts challenging. Moreover, transgenic expression of Aß peptides in the body wall muscle leads to a strong muscle-specific induction of the small heat shock protein HSP-16. This is suggested to be due to the misfolded protein response being activated. Multiple stress responses being active simultaneously creates a situation which complicates the conclusions drawn when elucidating stress response pathways in *C. elegans*.

3.4.2 The Challenges of Staining *C. elegans* tissues

Attempts to stain amyloid deposits in the iMAß$_{1-42}$ and iNAß$_{1-42}$ *C. elegans* AD models were unsuccessful. Despite this, the amyloid deposits in the body wall muscle of the iMAß$_{1-42}$ model have been successfully stained with X-34 in the past (McColl *et al.*, 2012). Unsuccessful staining of iMAß$_{1-42}$ animals was likely due to user error, which would have been explored further but due to Covid-19 lab restrictions and the emergence of novel fluorescently tagged Aß$_{1-42}$ *C. elegans* AD models, work shifted onto the novel strains (Gallrein *et al.*, 2021). It was not surprising X-34 staining of the Aß$_{1-42}$ deposits in the neurones of iNAß$_{1-42}$ animals at Day 1 of adulthood was unsuccessful, as dye-filling of neurones is challenging. Although the exact mechanism of dye-filling is unknown, it is generally assumed that the exposed cilium takes up the dye from the outside and stains the entire neuron (Bae, 2008). It has been proposed that amyloid aggregation occurs in IL2 neurones, and it is widely reported that this subset of sensory neurones are difficult to stain reproducibly (Tong and Bürglin, 2010; Gallrein *et al.*, 2021). Because of this, it may not be possible to reproducibly stain animals expressing neuronal Aß$_{1-42}$ therefore utilising the fluorescently tagged NAß$_{1-42}$ *C. elegans* AD model is the best way to track the peptide *in vivo*.

3.4.3 Intracellular or Extracellular Aβ$_{1-42}$ Aggregation

Prior to the publication of fluorescently tagged Aß$_{1-42}$ *C. elegans* models, untagged Aß$_{1-42}$ models were the gold standard of *C. elegans* AD models. Staining with X-34 shows MAß$_{3-42}$ has intracellular Aß deposits (Figure 16B), despite the construct

containing a modified signal-peptide sequence. This sequence had been previously utilised for the secretion of a *her-1* protein product ectopically expressed in muscle cells (Perry *et al.*, 1993). However, the original MAß$_{3-42}$ *C. elegans* model publication, stated the researchers were unconvinced that Aß aggregated extracellularly based on the Thioflavin S and anti-ß staining of transgenic animals. They hypothesised that the small size of the Aß$_{3-42}$ protein was affecting the secretory routing (Link, 1995). Later, X-34 staining confirmed that the Aß peptide was either being inefficiently secreted, or efficiently reabsorbed into the muscle cells. One theory postulated that Aß$_{3-42}$ was aggregating rapidly into fibrils that were too large to be secreted from the cell. However, muscle deficiency indicating aggregation is not significantly above wildtype in MAß$_{3-42}$ animals until day 4 of adulthood (Figure 15B), further evidenced by the lack of stain-reactive Aß deposits until Day 5 of adulthood (Figure 16B). From this it can be inferred that Aß$_{3-42}$ is detected as a misfolded protein and is actively re-routed to prevent its secretion (Link C.D *et al.*, 2001).

While exploring the best staining methods, a novel amyloid *C. elegans* model was kindly shared with us by the Kirstein Lab (The University of Bremen, Germany). This model utilised a new system was to overcome the challenge of fluorescently tagged Aß$_{1-42}$ in *C. elegans* utilizing a sub-stoichiometric labelling model. In this model, tagged and untagged Aß$_{1-42}$ are simultaneously translated from one bicistronic mRNA resulting in a lower proportion of tagged Aß$_{1-42}$ being transcribed compared to untagged; approximately 1:10. Sub-stoichiometric labelling has been used effectively to study amyloids *in vitro* (Pinotsi *et al.*, 2014; Young, Kaminski Schierle and Kaminski, 2017). The systemic defects and neurodegeneration exhibited in MAß$_{1-42}$ and NAß$_{1-42}$ strains (Figure 18, 19, 20, 21,)

confirm the labelling Aβ$_{1-42}$ peptides does not affect fibril propensity but it may alter Aβ$_{1-42}$ fibril morphology.

Like early *C. elegans* AD models, MAβ$_{1-42}$ and NAβ$_{1-42}$ constructs contain a signal peptide to secrete Aβ$_{1-42}$ out of the cell to aggregate extracellularly. Based on confocal images (Figure 17), it is likely the majority, if not all, Aβ$_{1-42}$ is localised and aggregating intracellularly in the MAβ$_{1-42}$ and NAβ$_{1-42}$ *C. elegans* AD models. However, there was evidence Aβ$_{1-42}$ was released from the original tissue to perturb distal tissues such as the hypodermis by an unknown method of transmission. The hypodermally expressed calcium-reporter sfGFP::Gal3 showed membrane integrity had deteriorated (Gallrein *et al.*, 2021), from this it could be inferred that rather than being secreted out of the cell, Aβ$_{1-42}$ is leaking from damaged cells possibly due to Aβ$_{1-42}$ membrane damage. While Aβ$_{1-42}$ is known to form extracellular plaques in AD, there is evidence Aβ$_{1–42}$ can be localized inside neurons and form interactions with intracellular proteins (Billings *et al.*, 2005; Kobro-Flatmoen, Nagelhus and Witter, 2016) meaning intracellular models are beneficial for observing the molecular traits of AD.

3.4.4 Mechanisms of HSP-90 Over-expression Induced TCS

Expressing fluorescently tagged Aβ$_{1-42}$ in the body wall muscle of *C. elegans* resulted in neurodegeneration and systemic defects including impaired motility (Figure 18), lifespan (Figure 19), fecundity (Figure 21), and chemotaxis (Figure 22). Over-expressing HSP-90 in the body wall muscle, intestine, and neurones of MAβ$_{1-42}$ animals, rescues the toxic phenotypes caused by muscular Aβ$_{1-42}$ expression. This indicates that over-expressing HSP-90 in the distal tissues of

MAß$_{1-42}$ animals initiates TCS to safeguard *C. elegans* from toxic Aß$_{1-42}$ and maintain overall organismal health.

As previously mentioned, over-expressing HSP-90 in the same or distal tissues of MAß$_{3-42}$ animals initiates a PQM-1 mediated response which activates TCS. PQM-1 regulates neuron-activated TCS through CLEC-41, an innate immunity-associated transmembrane protein, while intestine-activated TCS is regulated by ASP-12 an aspartic protease. Both mechanisms can induce HSP-90 expression in the body wall muscle, and which reduces Aß$_{3-42}$-associated toxicity (O'brien *et al*., 2018). It is highly probable that the PQM-1 mediated pathway is responsible for the reduced Aß$_{1-42}$-associated toxicity observed in Figures 17, 18, 20, and 21. To achieve this the *pqm-1* knock out *C. elegans* strain RB711 (CGC), could be used to generate mutants with the MAß$_{1-42}$::HSP-90 over-expression strains, and HSP-90 mRNA levels can be measured by qPCR.

Expressing fluorescently tagged Aß$_{1-42}$ in the neurones of *C. elegans* resulted in neurodegeneration and systemic defects including impaired motility (Figure 18), lifespan (Figure 20), fecundity (Figure 21), and chemotaxis (Figure 22). Over-expressing HSP-90 in the intestine and neurones of NAß$_{1-42}$ animals, rescues the toxic phenotypes caused by neuronal Aß$_{1-42}$ expression. But over-expression of HSP-90 in the body wall muscle of NAß$_{1-42}$ animals does not ameliorate Aß$_{1-42}$-associated toxicity. This indicates that over-expressing HSP-90 in the intestine of NAß$_{1-42}$ animals initiates an unknown intestine-to-neurone TCS to protect *C. elegans* from toxic neuronal Aß$_{1-42}$.

The intestine plays a critical role in cell-non-autonomous signalling to maintain proteostasis. The intestine orchestrates a network of signalling responses triggered by dietary and nutritional conditions, olfactory signals influenced by the nervous system, and environmental stressors that trigger protein quality control mechanisms. In C. elegans, the intestine functions to store fat (Mullaney and Ashrafi, 2009) and respond to pathogenic infections (Kim, 2018). It plays a crucial role in relaying information to the nervous system and other tissues, thereby facilitating communication and crosstalk among different bodily systems, ultimately contributing to maintaining organismal health and prolonging the lifespan of the animal. This is achieved by the intestine acting as a repository for lipids, which, upon release, serve as signalling molecules that facilitate communication between tissues (Imanikia *et al.*, 2019).

The expression of XBP-1s in the intestine is linked to alterations in lipid metabolism and promotes longevity and enhances cell-non-autonomous proteostasis (Imanikia *et al.*, 2019). Lysosomes are crucial organelles involved in lipid metabolism, actively facilitating the breakdown of lipids through lysosomal lipases. This process releases free fatty acids from triacylglycerols stored within the intestine. In addition to their role in lipid metabolism, XBP-1s expression in the intestinal tract also triggers an increase in lysosome activity, triggering protein quality control mechanisms, including autophagy. This, in turn, results in reduced aggregation and mitigates the proteotoxic effects associated with age-related disease proteins such as $A\beta_{1-42}$ in muscle tissues (Imanikia *et al.*, 2019).

Most examples of intestine-induced cell-non-autonomous signalling in *C. elegans*, the signals are received by the body wall muscle or have a systemic effect. A few

examples of intestine-to-neurone signalling have been observed in *C. elegans* to improve organismal health. Increasing SKN-1 in the intestine, blocks SPHK-1, which through unknown trans-tissue signals initiates neuropeptide secretion from the motor neurones initiating oxidative stress resistance (Minnerly *et al.*, 2017). Moreover, downregulating *daf-2* in the intestine, induces the expression of DAF-16, which via FOXO-to-FOXO signalling induces DAF-16 expression in the neurones which improves the longevity of *C. elegans* (Uno *et al.*, 2021).

Gaining deeper insights into the intercellular signalling interactions that transpire between the intestine and distal tissues, with a specific focus on intestine-to-neuron communication, has the potential to unveil promising avenues for future therapeutic strategies aimed at enhancing brain homeostasis as individuals age.

Chapter 4. Native In-Tissue Structures of Amyloid-β in a *C. elegans* model of AD by Cryo-ET

4.1 Introduction

Alzheimer's disease (AD) is a debilitating condition characterized by cognitive decline and brain atrophy. This deterioration is marked by various pathological features, including the emergence of extracellular protein deposits composed of Aß amyloid fibrils and intracellular neurofibrillary tau tangles, likely being the cause of loss of neurons and synapses (Cras *et al.*, 1991). The Aß peptide is present at varying lengths, with $Aß_{1-40}$ and $Aß_{1-42}$ being the most abundant, generated through the cleavage of Amyloid Precursor Protein (APP) by ß- and γ-secretases (Chow *et al.*, 2010). These peptides exhibit a high propensity for aggregation, initially forming oligomers and protofilaments before progressing into larger Aß fibrils (Iadanza *et al.*, 2018). Over time, the accumulation of Aß fibrils gives rise to amyloid plaques within the brain tissue, one of the key hallmarks of AD (Garwood *et al.*, 2017; Schwabe, Srinivasan and Rhinn, 2020).

In recent years, the structures of Aß amyloid fibrils have been revealed through cryoEM studies and 3D models reconstructed using helical reconstruction methods. These fibrils were either artificially assembled *in vitro* from recombinant or synthetic $Aß_{1-42}$ or extracted *ex vivo* from post-mortem brain tissue (Gremer *et al.*, 2017; Yang *et al.*, 2022; Leistner *et al.*, 2023). Notably, the *ex vivo* samples revealed two distinct structural configurations of $Aß_{1-42}$ amyloid fibrils. Type I fibrils were found to be associated with sporadic Alzheimer's disease in

human brains post-mortem, whereas type II fibrils were linked to familial disease and various other brain pathologies (Yang *et al.*, 2022). It is worth noting that both fibril types have dissimilar structures compared to Aß$_{1-42}$ fibrils produced in vitro and Aß$_{1-40}$ fibrils obtained from the meninges of 15 cases of cerebral amyloid angiopathy (CAA).

Despite these varying Aß$_{1-42}$ fibril structure characterisations, the precise molecular architecture and arrangement of Aß amyloid fibrils in native, unfixed tissue remained enigmatic until recently (Gilbert *et al.*, 2023; Leistner *et al.*, 2023). Unique assemblies, such as the structure of Aß amyloid fibrils *in situ,* are observed using cryogenic electron tomography (Cryo-ET). Cryo-ET is suitable for samples of varying size, from pleomorphic viruses to thick samples such as cells, tissue, or whole organisms like *C. elegans*. Depending on the sample, the method of freezing differs wherein thinner samples such as heterogenous protein or viruses, fractionated tissue homogenates, or cells grown on grids can be plunge frozen (Schaffer *et al.*, 2015; Hampton *et al.*, 2017; Hover *et al.*, 2023). This can be accomplished by applying blotting techniques to create a thin layer of aqueous sample, followed by immediate immersion in a cryogen, typically liquid ethane or propane cooled by liquid nitrogen (Dobro *et al.*, 2010). Once frozen, the grids can either be imaged as is, or thinned by focus ion beam (FIB) milling to produce ultra-thin lamella. This process involves eliminating atoms from the sample's surface by using a focused ion beam in a technique referred to as sputtering (Lam and Villa, 2021). High-pressure freezing (HPF) is a suitable method for vitrifying samples with thicknesses ranging between 100 – 300 µm. HPF entails elevating the pressure in the freezing chamber to 2000 bar while simultaneously reducing the temperature using liquid nitrogen (McDonald and Auer, 2006). However, for

these samples to be suitable for transmission electron microscopy (TEM), they must undergo subsequent thinning through cryo-sectioning typically by cryo-EM of vitreous sections (CEMOVIS) (Al-Amoudi *et al.*, 2004; Al-Amoudi, Norlen and Dubochet, 2004; Chlanda and Sachse, 2014), and more recently FIB milling and cryo-lift out (Schaffer *et al.*, 2019; Parmenter and Nizamudeen, 2021; Berger *et al.*, 2023).

The ultra-thin vitreous tissue sections produced from cryo-sectioning are adhered to grids, imaged by cryo-ET and reconstructed to produce tomograms. The resolution of tomograms is less than 10 nm, however with subtomogram averaging reconstructions can reach a resolution of 10 Å (Schur *et al.*, 2015). Tomograms are only useful when biological features can be confidently identified, and while certain cellular structures like mitochondria and ribosomes are obvious, many smaller features become challenging to recognize at lower resolutions, particularly in the case of locating protein complexes within their natural context. To address this challenge the method Cryogenic Correlative Light Electron Microscopy (cryo-CLEM) has been developed. This innovative approach integrates fluorescent microscopy with the use of fluorescent markers to enable the simultaneous tracking of proteins and other cellular components. A vitrified sample is first imaged using light microscopy to locate regions of interest or fluorescently tagged protein. Then, the same sample is transferred to an electron microscope for high-resolution imaging. (Sexton *et al.*, 2022).

Prior to the work being completed in this chapter, the molecular architecture of Aß fibrils and plaque assembly within native tissue was observed by producing ultra-thin cryo-sections from vitrified tissue samples obtained from the

homozygous mouse model App$^{NL\text{-}G\text{-}F/NL\text{-}G\text{-}F}$ (Leistner *et al.*, 2023) and post-mortem human AD brain (Gilbert *et al.*, 2023). Reconstructed tomograms obtained from both murine and human brain tissues provided insights into the intricate structure of extracellular Aß plaques. As expected, plaques were composed of Aß fibrils, but the tomograms also revealed branched fibrils and protofilament-like rods resembling early assembly intermediates.

While examining Aß amyloid fibrils in their native environment within the mammalian brain is highly impactful and clinically relevant, the study of Aß fibrils within the tissues of *C. elegans* still provides valuable insights. Firstly, it is essential to ascertain whether *C. elegans* remains a valid model for AD by comparing the molecular architecture of Aß amyloid fibrils in both mammals and nematodes. The presence of a similar structural configuration may signify common Aß pathologies in both mammalian and nematode models, thereby reinforcing the conclusions drawn from observations of AD-related phenotypes in *C. elegans* models. Furthermore, if Aß fibril structures exhibit similarities between mammalian and nematode models, it may suggest the potential for TCS to have a protective effect against fibril formation in mammals. Lastly, given the challenges associated with obtaining human AD brain samples, model organisms play an indispensable role in the study of neurodegenerative disorders. They offer a wide array of advantages, including genetic manipulability, shorter generation times, the conservation of critical biological pathways, and the capacity to manipulate and investigate the progression of diseases. These organisms effectively complement studies conducted in human patients and significantly contribute to the understanding of the root causes and potential treatments for neurodegenerative disorders.

Only recently, researchers have begun employing cryo-sectioning and cryo-ET techniques for the analysis of *C. elegans* tissues. Previous investigations involving nematodes predominantly utilized plastic or resin embedding methods along with room temperature sectioning to examine the overall cellular ultrastructure and assess changes associated with diseases (Gallrein *et al.*, 2021). Even today, the practice of cryo-sectioning and cryo-ET on adult *C. elegans* remains infrequent, with scientists often favouring specimens in the early stages of development or in the dauer stage due to their smaller size (Schaffer *et al.*, 2019; Buzzard *et al.*, 2023). This is because freezing adult *C. elegans* represents a significant bottleneck in cryo-ET workflows, as achieving vitrification within the core of the organism is a challenging endeavour.

4.1.1 Aims

Until now, the visualisation of dysfunctional amyloid within *C. elegans* has never been accomplished by cryo-ET. A novel workflow of HPF, CEMOVIS, and cryo-CLEM methodologies offered the opportunity to gain unprecedented insights into the *in-situ* structure and pathology of $A\beta_{1\text{-}42}$ amyloid fibrils in aged *C. elegans*. Due to the novel aspect of this work, and the limited use of *C. elegans* in published studies such as these, there was limited understanding into the workflow of cryo-ET of adult *C. elegans* tissue necessitating months of optimization efforts. As such, the aims of this section are as follows. To optimise correct vitrification of *C. elegans* by HPF and optimise the cryogenic ultramicrotomy of vitrified *C. elegans* tissue. Prior to, and after cryo-sectioning, use cryo-CLEM to target regions of Aß1-42 within vitrified *C. elegans* tissue and once located use cryo-ET to acquire

volumes of Aß$_{1-42}$ regions. Once reconstructed, annotate, and describe volumes of Aß1-42 pathology, and its relationship with surrounding cellular environment.

4.2 Methodology

4.2.1 High Pressure Freezing

The flat side of type B specimen carriers (Leica, 16770153) were coated in lipid to prevent carriers sticking together during the freezing process. Pressure graphs assessed using a dry run with two half cylinders and a middle plate. *C. elegans* to be frozen were incubated in cryoprotectant (20% w/v 40,000 Dextran in M9 buffer) for 1 hour.

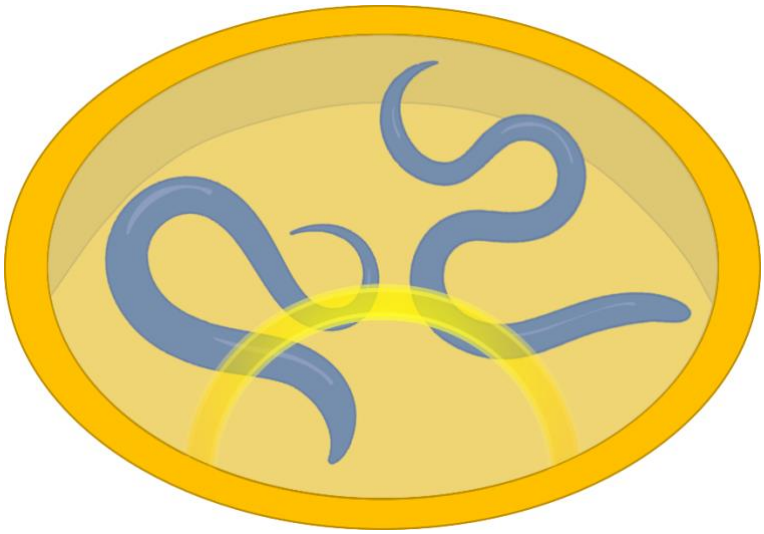

Figure 24. Diagram of High Pressure Freezing Adult *C. elegans*. The semi-circle of light which forms on the surface of the cryo-protectant which indicates the perfect volume inside the carrier for vitrification.

Animals were centrifuged (1000 xg, 5 minutes), and 1 – 2 µL of the pellet was aspirated into the 100 µm side of specimen carrier type A (Leica, 16770152). Over

or under-filling the well prevents vitrification, the perfect level was based on the ring of light forming a semi-circle at the bottom of the carrier (Figure 24). The lipid-coated type B specimen carrier was carefully placed on top, and carriers were high-pressure frozen at ~2000 bar, -188°C. The carriers were collected from Leica EM ICE and stored in eppendorfs.

4.2.2 Cryo-Sectioning

Cryo-sectioning was performed using a Leica EM FC7. Diamond knives were loaded into the knife holder at a 6° angle. The knives and sample holder were inserted into the cooling chamber, which was subsequently covered, and the instrument sealed in an acrylic chamber to prevent the build-up of frost. Prior to cryo-sectioning of the tissue, the carriers were trimmed to produce a small protruding pyramid shaped chunk of tissue (Figure 25).

Trimming prevents the gold of the carrier interfering with data collection of tissue and allows the pieces of tissue to connect and form a ribbon, which can be 'pulled' to an appropriate length and adhered to a grid. For trimming, the system was cooled to -160°C, at which point the carrier was loaded into the sample holder using pre-cooled tweezers. The carrier was trimmed using a diamond knife (DiATOME trim 45 T1865, trim 20 T3315) at a section thickness of 150 nm and a speed of 100 mm/s. The ionizer was mounted with the tip pointing towards the knife edge and set to 100% power. The sample was rotated 90° clockwise, and the carrier was trimmed to the point of interest. The sample was rotated a further 90° clockwise, and the knife was aligned to the sides of the carrier removing 100 µm of gold (Figure 25A). Subsequently, the knife was aligned with the edge of the

area of interest cutting back 60 µm (Figure 25B). The knife is retracted and aligned with the edge of the previous cut, using the west-east scroll wheel the knife was shifted 150 µm (Figure 25C), and a further 60 µm was removed.

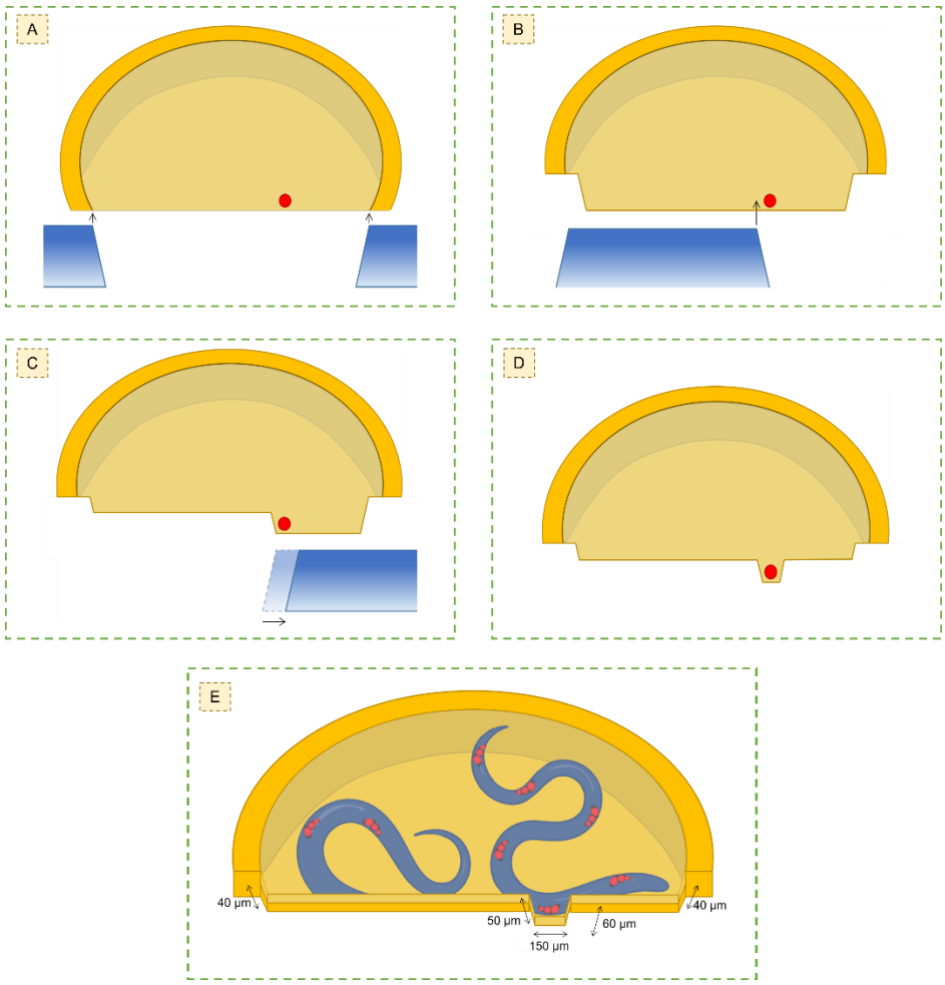

Figure 25. Schematic of a Sample Pyramid for CEMOVIS. (A) The trim-20 diamond knife was aligned with the carrier's sides, and 100 µm of gold is trimmed away on each side. (B) Cryo-CLEM identified the point of interest, the knife was aligned to the left-hand side, and 60 µm was trimmed away. (C) The knife was retracted, aligned with the previous trimmed edge, and shifted 150 µm to the right. (D) 50 µm of the back side of the gold carrier was trimmed away, leaving a small piece of tissue protruding, (E) measuring 60 µm in length and 150 µm in width.

The sample was rotated 90° anti-clockwise, the knife was aligned to only cut the carrier, and removed 40 – 50 μm of gold (Figure 25D). This left a small pyramid of tissue measuring 50 μm long, 150 μm wide, and 100 μm deep (Figure 25E).
The tissue was sectioned using a CEMOVIS diamond knife with a 35° angle (DiATOME MT 16563). For ultra-thin sectioning, the temperature in the chamber was adjusted to -150°C. The sample thickness ranged between 70 – 150 nm, and the cutting speed ranged between 0.5 – 2.0 mm/s. Two micromanipulator tools are attached inside the cooling chamber, on the left a gold coated eyelash and on the right forceps holding a glow discharged (Cressington glow discharger, 30s, 10-4mbar, 15mA) 2/2, 300 mesh Cu grid. The ionizer is mounted with the tip pointing towards the knife edge and adjusted according to how the ribbon behaves; typically, 30% power. Once pulled, the ribbon is positioned over the grid and adhered using the ionizer at 100% power.

4.2.3 Cryogenic Fluorescent Microscopy

High-pressure frozen carriers and ultra-thin tissue adhered to grids were screened for mScarlet fluorescence to locate $A\beta_{1\text{-}42}$ aggregates within the samples using a cryo-fluorescent microscope (cryo-FM, Leica EM Thunder). Samples were loaded into the transfer shuttle with pre-cooled tweezers and inserted into the thunder. Images were taken using a HC PL AP O 50x/0.9 NA cryo-objective, Orca Flash 4.0 V2 sCMOS camera (Hamamatsu Photonics) and a Solar Light Engine (Lumencor) using the LAS-X software. Samples were screened using the Rhodamine filter set (excitation 546/10, dichroic 560, emission 525/50) and Z-stacks of the grids were taken using a 0.2 X step size. For carriers, *C. elegans* with bright fluorescent deposits in the body wall muscle (Figure 26A) were taken

forward for cryo-sectioning, grids with flat, well-adhered tissue containing repeating fluorescent and limited frost build up (Figure 26B) were taken forward for data collection. Images were processed using the LAS-X software and Fiji ImageJ (Schindelin *et al.*, 2012).

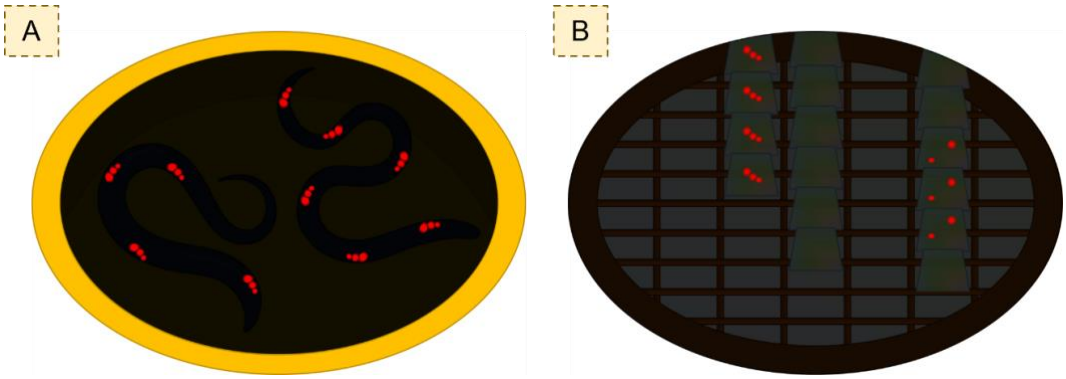

Figure 26. Diagram of Carrier and Grid Cryo-FM Screening for adult MAβ$_{1-42}$ *C. elegans*. HPF carriers and grids with tissue adhered are screened with cryo-FM (Leica EM Thunder) using the Rhodamine filter set (excitation 546/10, dichroic 560, emission 525/50).

Cryo-FM images of high-pressure frozen carriers were used to correlate the fluorescence in the tissue during sectioning using PowerPoint. For tomography, grid squares that contained signal for mScarlet under the Rhodamine filter were selected for electron microscopy. An EM atlas was collected of the whole grid at 370x magnification, 0.23 exposure, and illumination area of 1100 µm (pixel size: 34.97nm, total dose: 0.01e/nm2). The correlation between the tissue identified in the EM atlas and the fluorescence patterns detected in the cryo-FM images was used to guide the collection of tomogram data.

4.2.5 Cryo-Tomography Data Collection and Reconstruction

Tilt series positions were selected based on cryo-FM maps; positions were also selected in surrounding grid holes. Data was collected using a 300 keV FEI Titan Krios G2, X-FEG and autoloader, equipped with a Falcon 4i electron detector in counting mode and BioQuantum energy filter (GatanInc.). The tilt series was collected at 42,000 X magnification, from +60° to -60° with a tilt step of 2° using a dose symmetric tilt scheme in Tomo 5.13 (ThermoFisher Scientific). Data sets were collected using a 100 µm objective aperture and a -3.5 to -5.0 defocus range. Each tilt increment had 3.6 s exposure, fractionated into 6 movie frames at a 0.407 $e^-/Å^2$ dose rate, and thus a total dose per tilt series of 149.08 electrons and pixel size of 3.00 Å. Tilt series motion correction was carried out with MotionCorr2 1.3 (Zheng *et al.*, 2017). Tilt series stacking was achieved using IMOD stacker (Kremer, Mastronarde and McIntosh, 1996). AreTomo was utilised for automated tomogram alignment and reconstruction (Zheng *et al.*, 2022).

4.3 Results

4.3.1 Optimising High Pressure Freezing C. elegans

Limited methodology was available for high-pressure freezing and cryo-sectioning adult *C. elegans* as the majority of labs utilised freeze substitution and room temperature sectioning or cryo-sectioning young stage *C. elegans*. Vitrification and cryo-sectioning of adult *C. elegans* is technically difficult and requires specialized equipment (Hall D et al. 2012). For the initial round of freezing, we

followed protocols used prior to freeze substitution wherein animals were frozen using 20% BSA in M9 as a cryo-protectant.

BSA is preferable for freeze substitution as it is viscous and stays clear after osmium staining. It was difficult to produce ultra-thin sections using 20% BSA as a cryo-protectant as the sample would crumble rather than pull ribbons (Figure 27). Subsequently numerous different cryo-protectants were assessed including 20% glycerol, 20% sucrose, 20% glucose, and 20% dextran. Consequently, it was concluded 20% Dextran in M9 is the best cryoprotectant for adult *C. elegans*. Some publications state supplementing 20% Dextran in M9 buffer with 5% sucrose, glycerol, or glucose improves tissue vitrification (Gilbert *et al.*, 2023), however this showed no discernible difference in the ribbon quality of adult *C. elegans*.

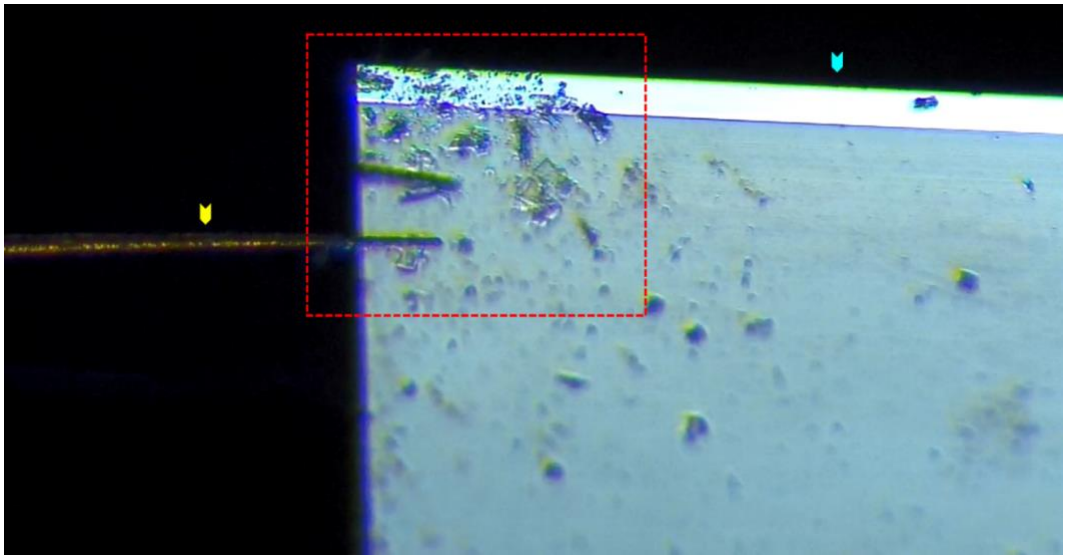

Figure 27. Adult *C. elegans* tissue devitrification during CEMOVIS. An example of devitrified tissue (red box) breaking apart on the edge of the diamond sectioning knife during CEMOVIS. Blue arrow indicates knife edge, yellow arrow indicates gold eyelash.

Screening of carriers containing large populations of *C. elegans*, showed unvitrified or damaged samples (Figure 28A, C). It was hypothesised this was due to animals swimming in the carrier, producing bubbles affecting the quality of the freeze. To counteract this, we froze fewer animals into a single carrier and immobilised animals using 5% levamisole, a paralytic, in M9 for 5 minutes prior to resuspension in cryo-protectant. This improved the vitrification of the cryo-protectant, but ultra-thin tissue sections would crumble indicating *C. elegans* tissue had not vitrified (Figure 28D). Consequently, the animals were incubated in cryoprotectant for at least 1 hour prior to high-pressure freezing. Feeding *C. elegans* Dextran allowed the cryo-protectant to be present within the animals. Additionally, suspending *C. elegans* in liquid for an extended period causes swim exhaustion thus temporary immobility. This greatly improved the vitrification of both cryo-protectant and *C. elegans*, allowing for ultra-thin cryo-sectioning (Figure 28B).

Following freezing, type A and B carriers would stick together and attempting to separate the carriers would damage the frozen samples, sometimes resulting in fractured ice (Figure 28C). To circumvent this, prior to freezing the flat side of type B carriers were coated with lipid. This step was successful in preventing carriers sticking together and protected the sample.

The level to which carriers are filled is essential to the freezing process. *C. elegans* float in sugar solutions, meaning when aspirated into a carrier, they will be at the surface of the cryoprotectant. If overfilled, the animals can either swim out of the carrier, or be ejected with the excess liquid when the flat B side carrier is placed

on top. The correct volume of liquid was present when a ring of light reflected onto the liquid in the shape of a semi-circle at the base of the carrier (Figure 24). This was the most important step for sample vitrification, second only to using the correct cryo-protectant.

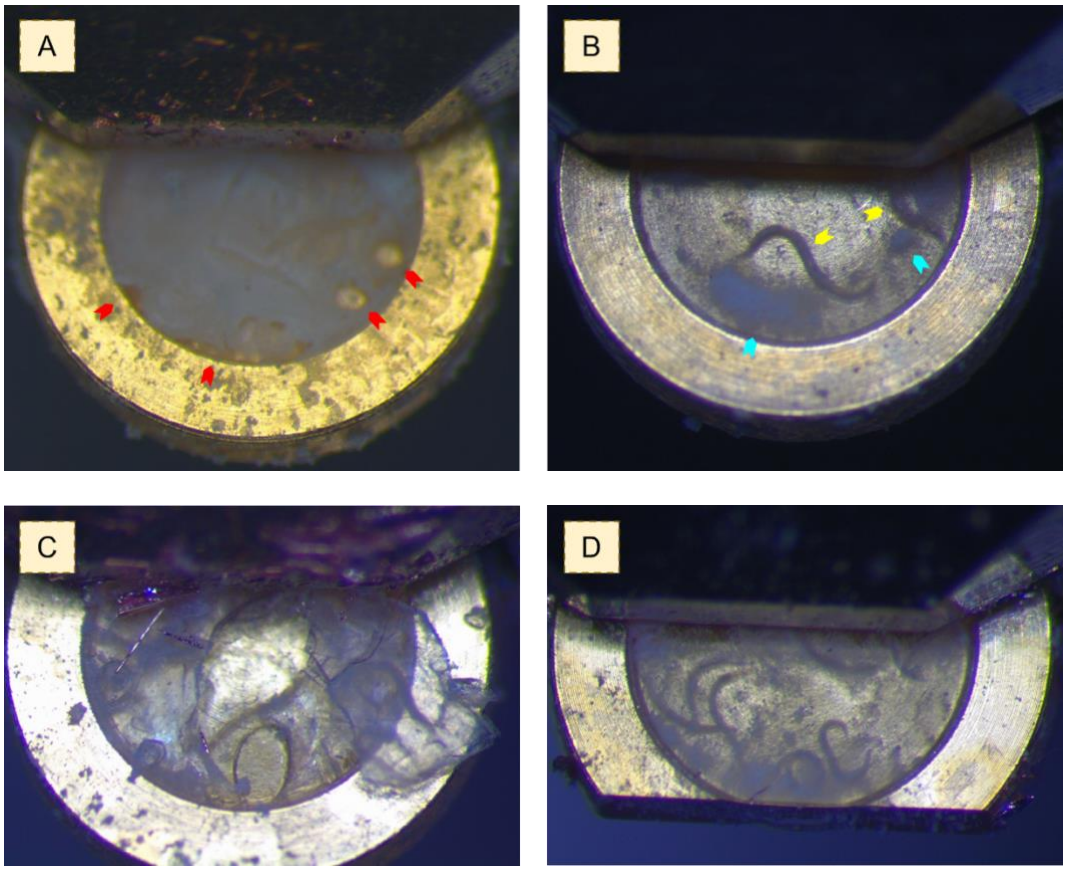

Figure 28. High Pressure Frozen *C. elegans* Samples During the Optimisation Process. (A) During the initial rounds of high pressure freezing samples were unvitrified and contained fractures and holes (red arrows). (B) Once optimised transparent, vitrified ice allowed for localisation of *C. elegans* tissue (yellow arrows), and subsequence cryo-CLEM and CEMOVIS; blue arrows indicate frost sitting on top of the carrier. During the optimisation process problems to overcome included (C) cracked and fractured ice or (D) sample devitrification.

4.3.2 Optimising Carrier and Grid Cryo-Fluorescent Screening

Cryo-FM grid screening plays a pivotal role not only in the context of cryo-CLEM correlation but also in assessing tissue quality and grid adherence. The visibility of tissue can be compromised when frost accumulates on the grid during the screening process (Figure 29A). Frost build-up is most likely when moving the grid from liquid nitrogen to the transfer shuttle. While some situations may make frost build-up inevitable, there are proactive measures that can be taken to mitigate it. The success of the CEMOVIS pipeline critically depends on strict adherence to fundamental precautions encompassing several key steps. Firstly, ensuring a constant supply of fresh liquid nitrogen is paramount.

Old liquid nitrogen can exacerbate frost accumulation as the longer it sits in unused vessels, including the transfer shuttle, liquid nitrogen bath, and liquid nitrogen canister, especially uncovered, allows for moisture infiltration. Grids must be transferred rapidly, with pre-cooled unused forceps, while wearing appropriate protective gear, such as a mask and nitrile gloves, in an isolated room. This approach significantly reduces frost formation on the grid. Finally, the liquid nitrogen supplied to the cryo-FM should always be fresh and the supply dewar should undergo a thorough thawing and drying process at least once a week. By following these guidelines, the effectiveness of cryo-FM grid screening is enhanced and thereby improves the overall success of the CEMOVIS pipeline (Figure 29B).

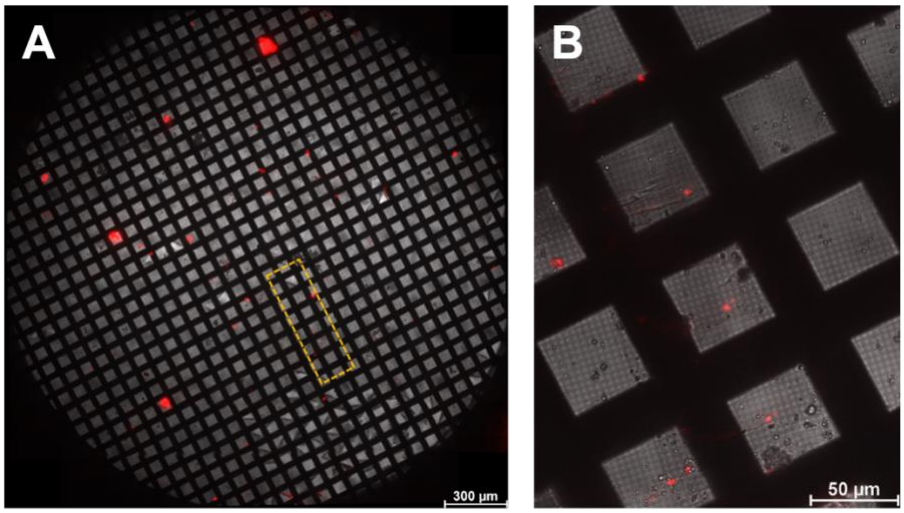

Figure 29. Reducing Frost Accumulation on CEMOVIS grids during cryo-FM screening. (A) Before method optimization, frost build-up on CEMOVIS grids hindered the observation of fluorescent tissue, rendering the grids unsuitable for cryo-ET data collection. (B) After method optimization, frost no longer obstructs the visibility of tissue, fluorescence is clearly discernible, and grids can be used for subsequent cryo-ET data collection.

Despite sectioning fluorescent tissue, the majority of ribbons did not exhibit the recurring fluorescence patterns observed in Figure 29B. This posed a significant challenge in distinguishing between tissue and cryoprotectant, and it raised questions about whether the puncta were too small in the ultra-thin sections, resulting in dim fluorescence. To address this challenge, Alexa Fluor™ 647-labeled dextran, possessing a distinct excitation/emission spectrum compared to mScarlet Aß$_{1-42}$ deposits in the MAß$_{1-42}$ *C. elegans* model, was introduced as a fluorescent cryoprotectant for CEMOVIS (Figure 30).

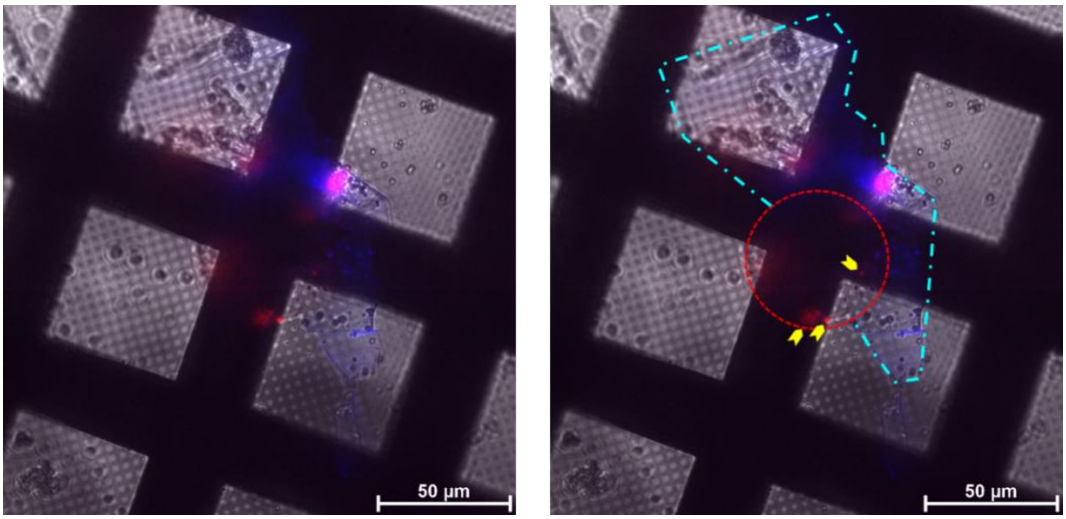

Figure 30. Alexa Fluor™ 647-labeled dextran used as a cryoprotectant for the CEMOVIS of adult MAβ$_{1-42}$ *C. elegans*. Cryo-FM image of ultra-thin cryo-sections with Alexa Fluor™ 647-labeled dextran as a cryoprotectant. The blue line outlines Alexa Fluor™ 647-labeled dextran, the red line outlines a cross section of the cylindrical body of adult MAβ$_{1-42}$ *C. elegans*, and yellow arrows point to Aβ$_{1-42}$ deposits within the body wall muscle of MAβ$_{1-42}$ animals.

Given the sub-stoichiometric tagging of Aβ$_{1-42}$ in MAβ$_{1-42}$ animals, only 1:10 Aβ$_{1-42}$ monomers is fluorescently tagged, and thus fibrils without fluorescence may be present within the tissue. Because of this, there remained value in capturing tomograms of non-fluorescent tissue, thus distinguishing tissue from cryo-protectant was essential. To achieve this, animals were initially incubated in unlabelled dextran for one hour before being immersed in labelled dextran and subsequently subjected to high-pressure freezing. This approach enabled a clear differentiation between cryoprotectant (blue) and tissue (red), enabling the visualization of cross sections of adult *C. elegans* tissue containing Aβ$_{1-42}$ puncta (Figure 31A, B).

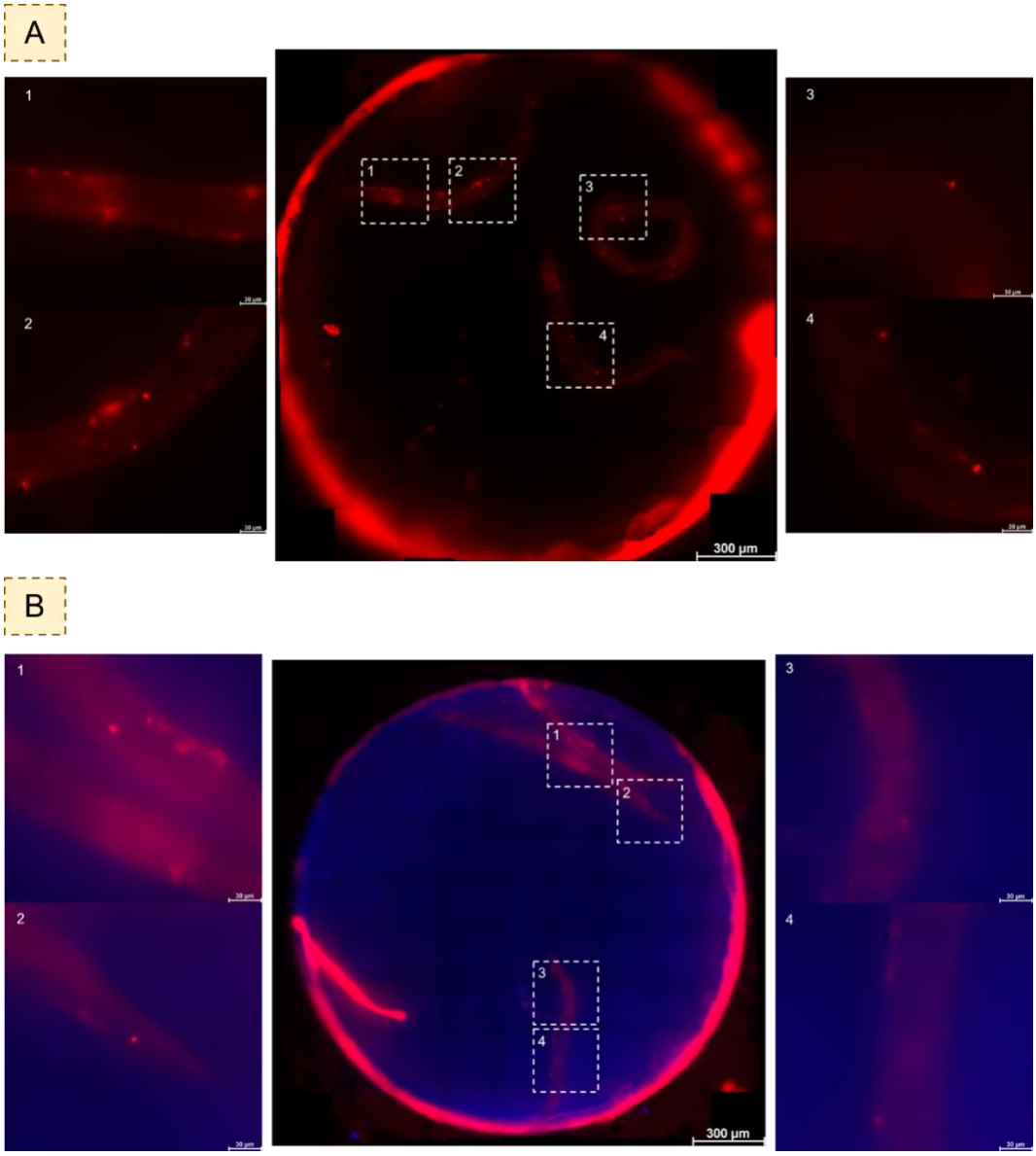

Figure 31. Cryo-FM of MAβ$_{1-42}$ *C. elegans* at Day 10 of adulthood. Cryo-FM of MAβ$_{1-42}$ *C. elegans* at Day 10 of adulthood high pressure frozen using either (A) 20% Dextran M9 buffer or (B) Alexa Fluor™ 647-labeled dextran M9 buffer as a cryoprotectant. (A, B) Red puncta in 1 – 4 side panels of displays Aβ$_{1-42}$ deposits in the body wall muscle of these animals. During sectioning, images are used to locate Aβ$_{1-42}$ deposits within *C. elegans* tissue for CEMOVIS.

4.3.3 Optimising Cryo-Sectioning

To facilitate CEMOVIS, a critical step involves securely affixing the ribbon of sections to the support film on an EM grid. This is accomplished through the utilization of an electrostatic charging apparatus, comprising a generator responsible for applying a high voltage to an electrode, foot pedals that allow precise control over the generator's output, and a control box for system management. The discharge mode of this apparatus generates an ionization current, which enhances the surface-glide properties of the diamond knife employed during vitreous cryo-sectioning. The degree of ionization can be finely tuned granting flexibility in the process. An electrostatic charging mode serves the purpose of securely attaching the vitreous cryo-sections to the support film of the EM grid. When transitioning the generator from the discharge to the charge mode, a brief burst of negative charge emanates in the proximity of the electrode. This charge effectively fastens the sections to the support film, ensuring their stability during the subsequent cryo-ET procedure (Pierson *et al.*, 2010).

This method manipulating the charge of the tissue relies on grounding of the FC7 cryo-ultramicrotome and its components, including the EM grid, golden eyelash, and diamond knife. The grounded EM grid is conductive and thus there is an electrostatic force between the negatively charged ribbon and the EM grid. Initial attempts to produce ultra-thin cryo-sections of tissue were hindered by ineffective grounding of the ultramicrotome. This impedes the user's ability to pull a ribbon, as the individual sheets of tissue do not connect to each other, there is no electrostatic attraction between the tissue and the golden eyelash, and the tissue will not adhere to an EM grid.

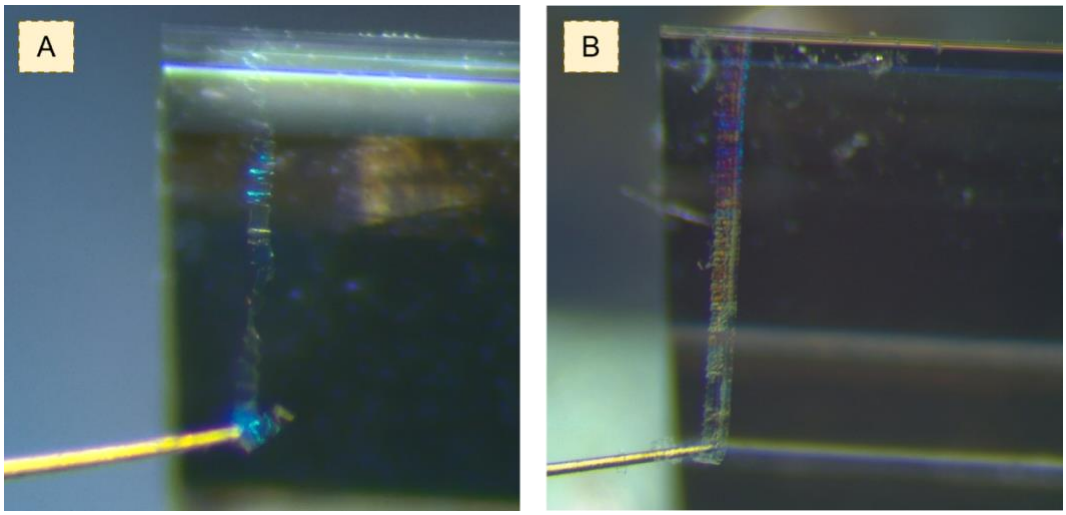

Figure 32. Improving the quality of ribbons produced from adult *C. elegans* tissue. (A) Twists and tears in the ribbon prior to optimisation of cryo-sectioning affect the quality and length of the ribbon, and the ability for the ribbon to adhere to glow discharged carbon coated grids. (B) Optimisation resulted in produced larger, stronger pyramids, and in turn more robust ribbons

To correct electrostatic attraction between the tissue and the golden eyelash, the nitrogen dewar supplying the ultramicrotome was grounded, and micromanipulators were replaced to ensure grounding to the gold-coated eyelash and grid. We introduced an anti-static earth grounding plug to offer a connection between the electrical supply and the earth below. This guaranteed that any electrical discharges were rerouted away from the ultramicrotome. Furthermore, static chargers introduced by the user were diminished using grounding cables connected to anti-static wrist straps, and a crocodile clip gripping an aluminium wire to directly ground individual components of FC7. While these adjustments improved sheets sticking together, and adherence of tissue to grids, under close inspection, oxidation of gold eyelashes could be observed, affecting their conductivity. Replacing eyelashes regularly maintained conductivity, and thus ribbon manipulation improved. Despite all optimisations, manual handling and

manipulation of tissue ribbons remains extremely challenging and is a major time limiting step in this type of structural analysis.

The production of long, robust ribbons is invaluable for precise ribbon placement on the EM grid. The ideal positioning for a tissue ribbon is between two adjacent grid bars, spanning the central region of the EM grid (Figure 26B). Prior to the optimization of cryo-sectioning, the tissue ribbons often suffered from unwanted twisting and tearing, leading to inadequate adhesion to the grid which, in turn, had downstream repercussions on cryo-ET data collection. An uneven or flawed tissue ribbon restricts the possible orientations for data acquisition, especially at higher angles, resulting in obscured specimen areas and the generation of subpar tomograms (Figure 33A). Imperfections in the sample pyramid, often stemming from sample devitrification or the inadvertent blunting of the knife edge during the trimming process, caused ribbons to twist or tear during the sectioning process (Figure 32A). To mitigate these issues, steps were taken to enhance sample vitrification (see Section 4.3.1), and all knives utilized were sharpened (DiATOME), to ensure precise and controlled sectioning.

Diamond trimming and sectioning knives are available in a variety of angles, each resulting in pyramids of different sizes depending on the angle of the cut. In the case of this delicate sample, a 45° angle proved too severe, leading to the production of pyramids that were not only too small but also too fragile. Consequently, the 45° angle was employed initially to cut through the bulk of the gold (24A). Subsequently, a 20° angle was adopted to craft the sample pyramid. By reserving the 20° angle for the sample pyramid, the knife's cutting edge remained sharp, yielding larger and sturdier pyramids. This, in turn, facilitated

the creation of more durable ribbons (Figure 32B) and higher quality tomograms (Figure 33B).

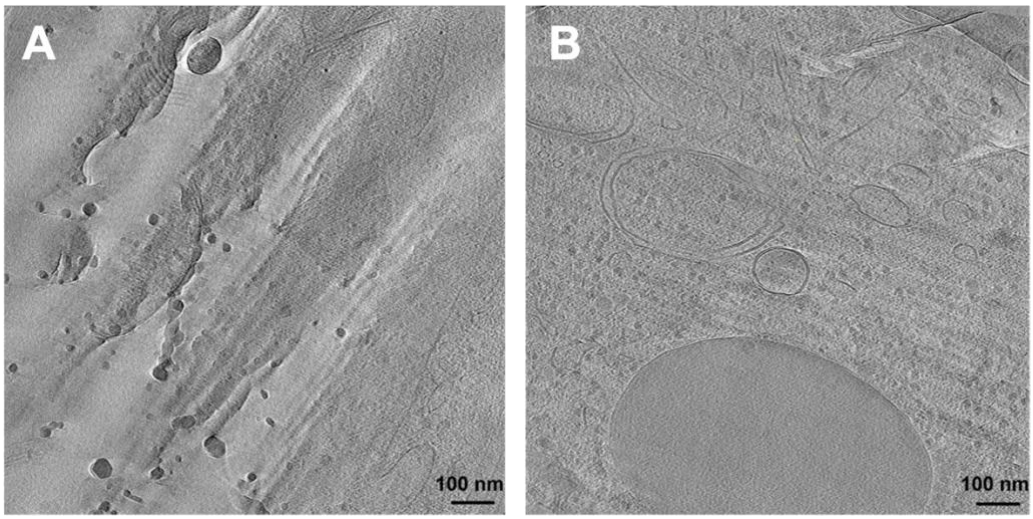

Figure 33. Poor vs High Quality Tomograms. (A) A poor-quality tomogram acquired from a damaged tissue ribbon, sitting unevenly on the support film on an EM grid. (B) A high-quality tomogram, acquired from a 70 nm thick tissue ribbon exhibiting a good contrast on subcellular structures.

The section thickness varied between 70 and 150 nm. Ribbons crafted from sections measuring 70 to 90 nm in depth are more challenging to handle, but they demonstrate superior grid adherence and yield high-quality tomograms thank thicker sections. In the initial high-pressure freezing procedure, adult *C. elegans* were cryogenically preserved in carriers with depths of both 100 μm (Figure 34A) and 200 μm (Figure 34B).

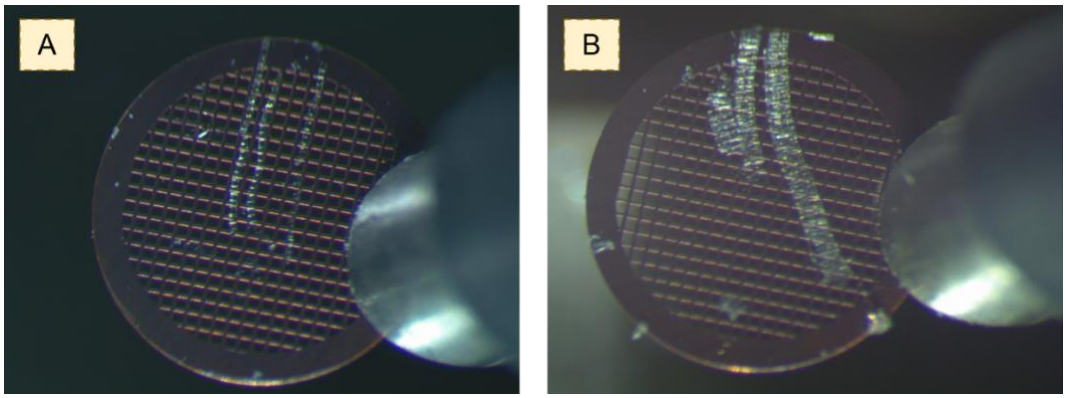

Figure 34. Tissue ribbons from different depth HPF carriers. (A) The tissue ribbons produced from high pressure freezing adult *C. elegans* in carriers of 100 μm depth. (B) The tissue ribbons produced from high pressure freezing adult *C. elegans* in carriers of 200 μm depth.

Vitrifying adult *C. elegans* poses a significant challenge, and there is a low probability of achieving vitrification at the core of a 200 μm carrier. In instances where vitrification did occur in 200 μm carriers, a notable enhancement in the structural integrity of the sample pyramid was observed, and ribbon manipulation significantly improved. However, wider ribbons proved to be less stable when sectioned at 70 to 90 nm, often resulting in ribbon breakage. Stability was achieved more effectively within the 120 to 150 nm section thickness range. Nevertheless, ribbons of this thickness displayed diminished adherence to the grid and resulted in tomograms of lower quality. Handling ribbons measuring 100 μm in width and 70–90 nm in thickness presents a notable challenge. However, with practice, proficiency of tissue manipulation increases. Striving for the optimal balance between grid adherence and tomogram quality, the most desirable ribbon dimensions were found to be 70–90 nm in thickness and 100 μm in width.

4.3.5 *In situ* Tomography of the Adult MAβ$_{1-42}$ *C. elegans* Model

Following optimisation, cryo-ET data collection was acquired from EM grids with tissue ribbons. Grids were selected with strongly adhered 70 – 90 nm thick tissue, both positive and negative for Aβ$_{1-42}$ deposits determined by cryo-FM (Figure 29B). Due to the low throughput nature of the CEMOVIS workflow, only one tomogram was acquired from *C. elegans* expressing Aβ$_{1-42}$ in the body wall muscle at Day 10 of adulthood (Figure 36). However, tomograms displaying the tissue architecture of these animals (Figure 35) were still valuable to exhibit the successful optimisation of using adult *C. elegans* tissue for CEMOVIS and cryo-ET data collection.

The tomograms revealed a range of components, including amyloid fibrils, which were identified through mScarlet cryo-CLEM labelling or their characteristic rod-like, twisted shapes running in parallel, consistent with descriptions found in the literature (Gilbert *et al.*, 2023; Leistner *et al.*, 2023). Ribosomes were distinguishable as circular objects of approximately 30 nm in size, featuring higher tomographic density compared to the surrounding macromolecules, attributable to their abundant nucleic acid content. Microtubules were recognized as approximately 25 nm wide filaments, displaying a distinctive 'star-shaped' end configuration. The cell plasma membranes encapsulated various organelles, such as ribosomes, microtubules, and mitochondria (Figure 35). Finally, knife damage was discerned in specific regions of the tomogram where the sample had undergone compression or tearing, resulting in visible fractures within the tissue, which were easily identifiable as holes (Figure 35).

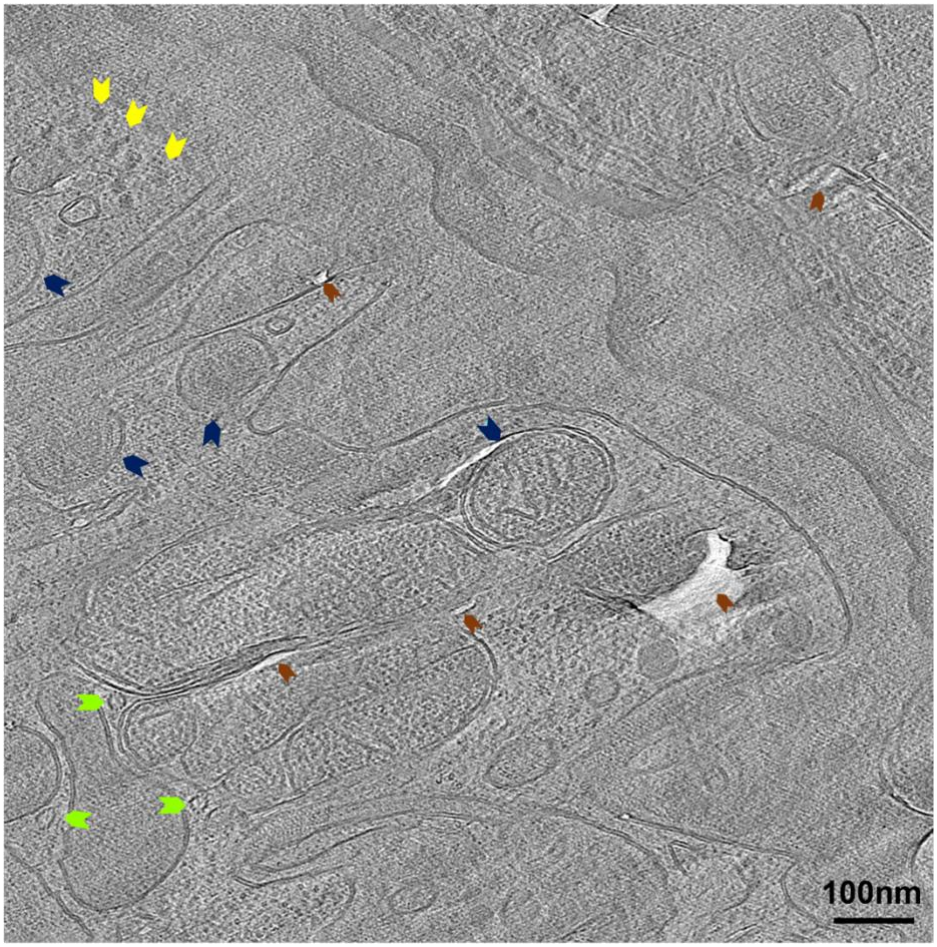

Figure 35. Tomographic slice through a cryo-ET reconstruction of the cellular ultrastructure within adult *C. elegans*. A tomogram of tissue sectioned from MAβ$_{1-42}$ animals, cryogenically frozen at day 10 of adulthood. Yellow arrowheads, ribosomes. Navy blue arrowheads, mitochondria. Lime green, microtubules. Brown arrowheads, localised knife damage in tissue cryo-section. 100 tomograms were reconstructed in total, one was selected here as a representation of all tomograms not containing amyloid. This tomogram was selected due to the large variety of organelles and sub-cellular features visible. Scale bar 100 nm.

The tomogram containing Aβ$_{1-42}$ fibrils, has relatively low contrast, making conclusions difficult to draw. Several cellular features can be observed in close proximity to the Aβ$_{1-42}$ fibrils as well as features such as ribosomes and lipid

bilayers being present between parallel bundles of fibrils (Figure 36), which is in accordance with the literature (Gilbert *et al.*, 2023; Leistner *et al.*, 2023).

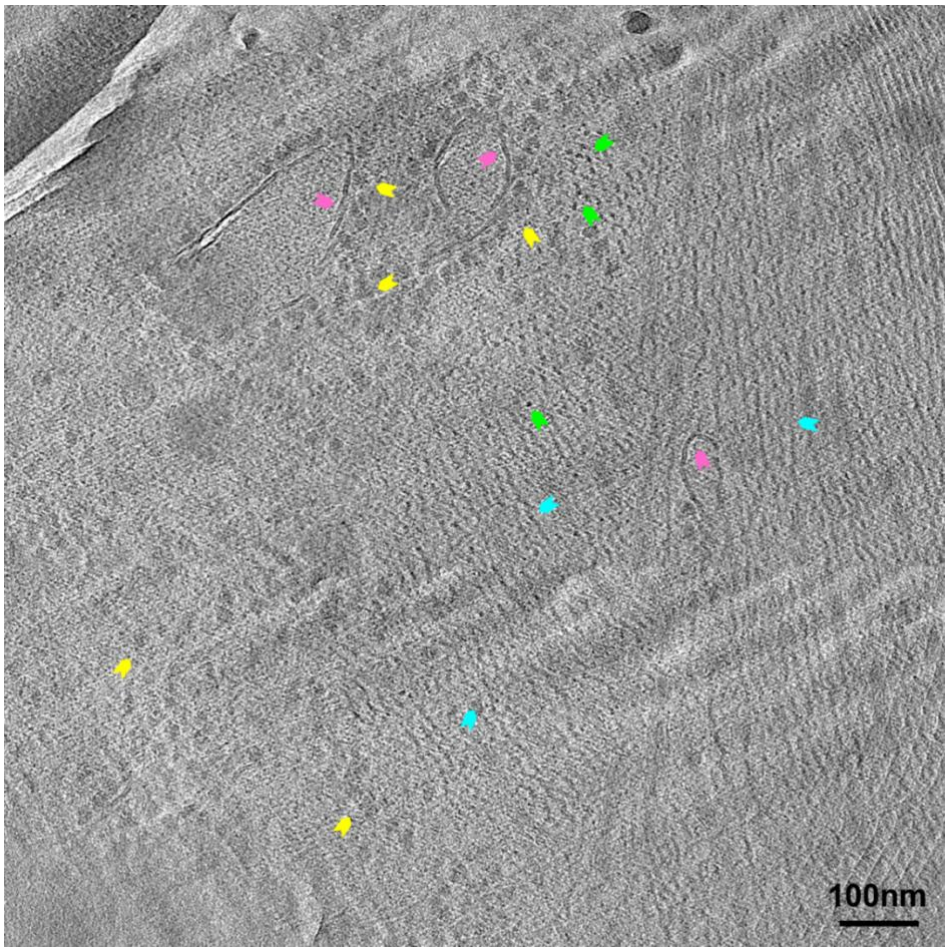

Figure 36. Tomographic slices through cryo-ET reconstruction of Aβ$_{1-42}$ pathology within adult *C. elegans*. A tomogram of tissue sectioned from MAß$_{1-42}$ animals, cryogenically frozen at day 10 of adulthood. Pink arrowheads, lipid bilayers. Yellow arrowheads, ribosomes. Green arrowheads, Aß$_{1-42}$ fibril ends. Cyan arrowheads, Aß$_{1-42}$ fibrils. 100 tomograms were reconstructed in total, one tomogram contained amyloid fibrils. Scale bar 100 nm.

However, deciphering if these fibrils are intra- or extracellular is challenging. Based on the presence of ribosomes, and no clear lipid bilayer separating intra-

and extracellular regions, it could be inferred that Aß$_{1-42}$ fibrils are aggregating intracellularly in the body wall muscle of MAß$_{1-42}$ *C. elegans*.

4.4 Discussion

4.4.1 CEMOVIS Method Development

Here high-pressure freezing was employed to cryo-immobilize adult *C. elegans* for cryo-ET studies. Vitrifying the core of the animal proved to be a formidable challenge, therefore exploring options beyond vitrification of the whole animal was necessary. Some groups have achieved moderate success in homogenizing brain tissue from mouse models to observe amyloid plaques by plunge freezing the homogenates onto grids. This method can be complemented with the introduction of fiducial markers, such as immunogold, during plunge freezing which facilitates tomographic reconstructions (Han, Zhang and Gao, 2018). This approach not only proves more cost-effective, and higher throughput when compared to HPF and subsequent CEMOVIS. However, while plunge-frozen homogenates of homozygous mouse model AppNL-G-F/NL-G-F brain tissue have successfully vitrified, no Aß fibrils or plaques could be observed in the reconstructed tomograms. The researchers concluded this was likely due to the abundance of plaques in brain being too low for reliable detection.

While cryo-sections exhibit a lower signal-to-noise ratio, they offer the distinct advantage of preserving the native in-tissue architecture, and by employing CLEM, it becomes possible to trace small quantities of amyloid fibrils and plaques within large tissue samples. Previous studies focused on vitrifying *C. elegans*

primarily during the early stages of development or during the dauer stage, due to the substantial size reduction in comparison to adult animals. One method to successfully vitrify early-stage *C. elegans* and embryos included loading anaesthetized animals into cellulose capillary tubing, possessing an inner diameter of 200 µm, followed by crimping the tube ends to securely enclose the nematodes. Subsequently, a 1 mm segment of this capillary tube is placed within the cavity of a membrane carrier with a depth of 100 µm. This assembly is then carefully inserted into the rapid transfer system of the EM PACT2 for high pressure freezing. While attempting this method, we encountered a roadblock as adult *C. elegans* proved too large for the tubing. Looking ahead, it's possible that future advancements in tubing options, offering a wider range of diameters, could render this method more viable for freezing adult *C. elegans*, in the interim, high-pressure freezing in gold-coated carriers proved to be the best alternative, which effectively preserved the native state of the tissue.

Recent developments in CEMOVIS have significantly enhanced the accessibility of this technique. Historically, tissue attachment to grids was achieved through compression, a process that introduced artifacts and caused damage to delicate tissue sections. However, following modernisation, the method now employs electrostatic charge to affix tissue onto a hydrophilic grid, facilitating the connection between the sample and the carbon grids. While using electrostatics circumvents tissue damage, it is imperative that the instrument is properly grounded to the earth. Initial efforts to create ultra-thin cryo-sections of tissue were impeded due to the inadequate grounding of the cryo-ultramicrotome, which were rectified by introducing new grounding cables, new gold-coated eyelashes, and adding the option to manually ground individual elements of the cryo-

ultramicrotome. Another significant advancement involved the addition of micromanipulators to the cryo-ultramicrotome, enhancing the ease with which tissue could be manipulated and adhered to grids, and thus the accessibility of this technique. Despite these technological advancements, the success rate of tissue attachment for cryo-sectioning remains low, which presents a distinct challenge, especially within the vacuum environment of the Krios.

It is important to note that CEMOVIS remains a highly challenging technique which offers limited throughput, and other cryo-sectioning techniques are accessible. Until recently, cryo-FIB milling could only be done on vitrified single cells plunge frozen onto grids, however with a cryo-gripper tool targeted extraction of material from high-pressure-frozen adult *C. elegans* for a structural study of cytosolic 80S ribosomes. In this technique, high-pressure frozen samples are cryo-planed, screened by cryo-FM allowing for targeted FIB-milling of the sample. During the milling procedure, trenches are created on both sides of the target volume to produce a lamella approximately 3 µm in thickness, ready for lift-out. This lamella is grasped by the cryo-gripper tool and delicately removed from the sample before being placed into the designated slot on a TEM half-grid. To ensure optimal electron transparency for cryo-ET, the lamella is further milled to a thickness of 150 nm. This approach yields high-resolution tomograms, which enables detailed subtomogram analysis of cellular structures and proteins such as ribosomes. Through refinement, these tomograms have achieved resolutions spanning from 11.8 Å to 15.6 Å. In the future, there is potential to apply this technique for advanced structural investigations involving adult *C. elegans*. However, it's important to note that only a limited number of research

laboratories currently possess the necessary equipment and expertise to conduct such studies.

While conventional cryo-FIB/SEM methodologies may not suit all sample types, recently a novel solution known as the 'waffle method' was developed to addresses these limitations. This method integrates a grid into the high-pressure freezing (HPF) workflow, offering an approach for FIB-milling thick specimens with vitrification issues, samples that tend to unevenly distribute across grid squares, or samples like *C. elegans* that cannot be plunge-frozen conventionally. To implement the waffle method, the flat sides of type B specimen carriers are coated with a lipid layer to prevent them from sticking together. A carrier is positioned with its flat side facing upward, and on top of it, a glow-discharged grid coated with a thin layer of carbon is placed. To create a small well for the sample, a slot grid is then positioned on top of the carbon-coated grid. The sample is pipetted into this well on the grid surface. Once the sample is in place, the flat sides of another type B specimen carrier can be positioned on top, effectively sealing the sample within the well. Subsequently, the entire assembly is high-pressure frozen, enabling the successful cryo-immobilisation of the sample on a grid for FIB-milling. In this chapter, this method was applied to vitrify adult *C. elegans*; unfortunately, the initial attempts did not yield the desired results. Due to time constraints, optimisation of the freezing process for *C. elegans* using the waffle method was not possible. However, it remains a viable avenue for exploration in future research endeavours.

Despite the challenges of cryo-sectioning, adult *C. elegans* tissue was successfully sectioned by CEMOVIS following optimisation of the method as described

previously. Although, the tissue was prone to cutting damage which would not be fully eliminated during sectioning. To improve the quality of the sections, the CEMOVIS method requires further optimisation and improvements.

Another significant challenge encountered when sectioning tissue to study something as small and sparse as amyloid fibrils, is akin to finding a "needle in the haystack". The composition of Aß$_{1-42}$ amyloid fibrils, or if plaques are being formed in *C. elegans* is unknown. Locating amyloid within the tissue proved challenging, possibly due to a relatively low amyloid plaque density. Incorporating cryo-CLEM as an additional step to the workflow, resulted in a breakthrough which offered more precise guidance for the collection of ultra-thin cryo-sections, and increased the success of observing repeating fluorescence in cryo-sections of tissue affixed to grids indicating the presence of Aß$_{1-42}$ fibrils. However, mScarlet cryo-CLEM of MAß$_{1-42}$ animals was not always dependable due to sub-stoichimetric tagging of Aß$_{1-42}$ in this model resulting in most Aß$_{1-42}$ monomers being untagged. Incorporating an amyloid stain, such as X-34 (see Section 3.3.1.3) or Methoxy-X04 (Gilbert *et al.*, 2023; Leistner *et al.*, 2023), could make more Aß$_{1-42}$ fibrils evident in the MAß$_{1-42}$ *C. elegans* model and should be explored in the future.

4.4.2 Qualitative Tomogram Assessments

Conventional EM studies conducted on plastic-embedded tissue samples from post-mortem AD brain and familial AD animal models have traditionally provided valuable insights. These studies have indicated that plaques are primarily composed of parallel bundles and a lattice-like network of Aß fibrils, shedding

light on the structural organization of these amyloid deposits. The molecular architecture of Aß fibrils and plaque assembly in their natural context was observed using ultra-thin cryo-sections from vitrified tissue samples obtained from the homozygous mouse model AppNL-G-F/NL-G-F (Leistner *et al.*, 2023). This model uses a knock-in strategy to express APP at natural levels rather than over-expressing the protein, to enhances the levels of pathogenic Aß by incorporating mutations associated with familial Alzheimer's disease. Tissue samples were analysed by cryo-CLEM and cryo-ET, which produced tomograms of fully assembled Aß fibrils, protofilament-like rods and branched fibrils presenting a complex network of fibrils interwoven with non-amyloid constituents (Leistner *et al.*, 2023). Qualitative analysis of the tomogram (Figure 36) revealed that fibrils were organised into parallel bundles, and the tightly packed meshwork observed in mammalian models was not present in *C. elegans* tissue. However, this is based on one tomogram, and the previously observed meshwork may be elucidated in *C. elegans* if more tomograms containing $Aß_{1-42}$ fibrils were acquired.

The optimisation of this workflow in *C. elegans* offers the opportunity to shed light on the structural complexity of $Aß_{1-42}$ but also contribute to our understanding of the pathological processes underlying neurodegenerative diseases like AD.

Chapter 5. TCS is an Intercellular Stress-Response Distinct from the HSF-1-Mediated HSR

5.1 Introduction

5.1.1 HSP70

The HSP-70 family functions in the folding and refolding of proteins and plays a role in protein disaggregation. The HSP-70 proteins operate through cycles of ATP-dependent binding and releasing of client proteins, orchestrated through allosteric coupling between the Hsp70 ATPase domain and the C-terminal substrate-binding domain (SBD) (Kohler and Andréasson, 2020). The SBD comprises of a subdomain with a ß-sandwich structure, characterized by two opposing antiparallel ß-sheets, and an α-helical lid segment. The ß-sandwich subdomain recognizes hydrophobic amino acids (Rüdiger, Buchberger and Bukau, 1997), often associated with protein aggregation, in extended segments of approximately seven residues typically appearing at intervals of 50-100 residues (Rousseau, Serrano and Schymkowitz, 2006). Additionally, the SBD possesses an α-helical lid segment which modulates the binding affinity for peptides in an ATP-dependent manner. HSP-70s do not operate in isolation; they interact with various co-chaperones to fulfil their functions, which usually include Hsp40 and a nucleotide exchange factor (NEF) (Kampinga and Craig, 2010). The presence of Hsp40 stimulates the ATPase activity of Hsp70 and the hydrolysis of ATP triggers the closure of the lid and stable binding of the peptide. Following ATP hydrolysis, a NEF binds to the Hsp70 ATPase domain and facilitates the exchange of ADP

for ATP, reopening the α-helical lid and the releasing the substrate (Langer *et al.*, 1992; Kampinga and Craig, 2010).

5.1.2 Systemic and Tissue-Specific HSP-90 Depletion

One of the intrinsic functions of HSP-90 is to exert a negative regulatory effect on HSF-1 activity (Zou *et al.*, 1998). Consequently, systemic hsp-90 knockdown leads to heightened HSF-1 activity, resulting in the upregulation of target genes such as hsp-70. This effect can be observed in strains carrying the hsp-70 transcriptional reporter, predominantly in the body wall muscle (Gaiser *et al.*, 2011; van Oosten-Hawle, Porter and Morimoto, 2013). However, it is crucial to note that this upregulation does not translate into an improvement in the muscle folding environment. On the contrary, these animals exhibit a range of adverse outcomes, including reduced motility and the formation of insoluble myosin aggregates (Gaiser *et al.*, 2011).

Within the HSR, the HSP-90 capacitor hypothesis is a pivotal concept. HSP-90 is described as a 'hub' protein with an extensive network of known interaction partners and a critical role in cellular signalling processes, both in normal and stressful conditions (Taipale, Jarosz and Lindquist, 2010; Da Silva and Ramos, 2012; Freeman and Morimoto, no date). The capacitor hypothesis states that sporadic mutations produce variants which can alter phenotypes observed both *in vitro* and *in vivo*. HSP-90 interacts with, and stops the expression of, these phenotype-altering variants resulting in systemic accumulation of silenced or cryptic state variants (Rutherford and Lindquist, 1998; Queitsch, Sangster and Lindquist, 2002).

However, during systemic or tissue-specific HSP-90 depletion, regardless of whether it is a result of reduced function or an increased demand for protein re-folding during cellular stress, phenotype-altering variants are no longer silenced (Sollars *et al.*, 2003). The consequence of this newfound freedom depends on the fitness of the resulting phenotype. A previously cryptic variant may thrive under these altered conditions and evolve to operate independently of HSP-90 regulation. The knockdown of *hsp-90* gene diminishes the buffering capacity against cryptic mutations in *C. elegans* resulting in the manifestation of altered phenotypes. In accordance with the capacitor hypothesis, HSP-90 is deemed an essential gene for the development of *C. elegans* (Birnby *et al.*, 2000). *C. elegans* subjected to hsp-90 RNAi from the L1 stage onward follow a trajectory of delayed development, ultimately reaching adulthood but as sterile animals. These individuals exhibit an elevation in the expression of HSF-1 target genes, such as hsp-70, small heat shock proteins (sHSPs), and HSP-90 co-chaperones (Eckl *et al.*, 2017). Simultaneously, a reduction in the expression of immune-related genes, particularly C-type lectins and aspartyl proteases, is observed in hsp-90 knockdown animals, especially in the intestine. Furthermore, regardless of whether hsp-90 RNAi is initiated at the L1 or L4 stage, animals display a reduced lifespan, underscoring the critical role of hsp-90 in preserving health and organismal lifespan longevity (Somogyvári, Khatatneh and Sőti, 2022). Body wall muscle-specific *hsp-90* knockdown can result in defective intestine, tail, or excretory canal development, while intestine-specific *hsp-90* knockdown causes abnormal gonad development (van Oosten-Hawle, Porter and Morimoto, 2013). This is consistent with the HSP-90 capacitor hypothesis and the role of HSP-90 in suppressing cryptic mutations in wild-type animals.

While research has examined the impact of systemic hsp-90 knockdown in C. elegans, there remains a significant knowledge gap regarding the systemic implications of tissue-specific hsp-90 depletion. Previous studies have demonstrated that tissue-specific suppression of hsp-90 in neurones, intestine, or body wall muscle of *C. elegans* results in a developmental delay and the emergence of abnormal phenotypes (van Oosten-Hawle, Porter and Morimoto, 2013). Notably, these effects are also observed during non-cell-autonomous upregulation of a hsp-70p::mCherry reporter through the TCS pathway, which is particularly prominent in the body wall muscle. This leads to an overall increase in hsp-70 transcript expression and enhanced resistance to heat stress. It was hypothesised that the improved resistance to heat stress may be attributed to the increased expression of protective hsp-70 proteins.

5.1.3 TCS activated by Tissue-Specific *hsp-90* Knock Down

When genes are knocked down systemically in whole organisms there is potential for multiple signalling pathways to be activated or interrupted, complicating interpretation of the results. However, in the case of both systemic and tissue-specific knock down of *hsp-90*, nematodes exhibit developmental delays and aberrant phenotypes. Tissue-specific knockdown of HSP-90 in *C. elegans* activates cell-non-autonomous upregulation of hsp-70p::mCherry dependent on the transcription factor PHA-4. These strains also exhibit an increased resistance to heat stress, contrary to TCS activated by tissue-specific HSP-90 over-expression (van Oosten-Hawle, Porter and Morimoto, 2013). It is theorised this arises from either the increased expression of protective HSP-70, or from

differential expression of additional genes regulated by TCS. Systemic knock down of *hsp-90* results in the upregulation of HSP-90 co-chaperones, HSP-1, small heat shock proteins, and subunits of the TCP1 chaperonin complex (Eckl *et al.*, 2017), indicating *hsp-90* knock down supports increased expression of chaperones.

5.1.4 Overview of Aims

TCS activated by tissue-specific HSP-90 over-expression is regulated by the transcription factor PQM-1 (O'Brien *et al.*, 2018). The understanding of the intracellular and intercellular mechanisms that drive TCS activated by tissue-specific hsp-90 knockdown is limited (van Oosten-Hawle, Porter and Morimoto, 2013). Thus, the primary aim of this chapter is to delve deeper into the effects of TCS in strains harbouring integrated arrays of tissue-specific hsp-90 hairpin RNAi. To do this the aim was to explore whether the activation of TCS in these strains could confer benefits in terms of longevity, heat stress resistance, or the management of protein aggregation and to elucidate the mechanism by which this occurs.

5.2 Methods

5.2.1 *hsp-90* Knock Down *C. elegans* Strains Maintenance

Tissue-specific knock down of *hsp-90* in *C. elegans* is a viable but sensitive RNAi. HSP-90 plays an important role in slowing the occurrence of mutations, and *hsp-90* knock down strains accumulate cryptic mutations faster than wild-type *C. elegans*, altering the phenotypes observed in these strains, clouding data

interpretation. The strains were backcrossed into the original genetic background, *sid-1 (pk3321)* mutant strain (CGC), ten times prior to analyses to eradicate the unlinked cryptic mutations which accumulated during random mutagenesis.

When studying the stress response, reducing stress endured by tissue-specific *hsp-90* knock down *C. elegans* strains is essential for valid results. Bleaching is a common method of *C. elegans* population synchronisation, and while effective, the method induces starvation and potential oxidative stress if oxygen levels decrease. To avoid activating incorrect stress response pathways, strains were synchronised by egg-laying, where gravid adults were moved onto fresh NGM agar plates and allowed to lay eggs for 6 hours before being removed.

5.2.2 Gene Knock Down by RNAi

A *C. elegans* RNAi feeding library was obtained from The University of Cambridge containing RNAi vectors cloned into the L4440 destination vector transformed into HT115 *E. coli* (Kamath, 2003). Strains were synchronised by egg-laying on plates seeded with HT115 *E. coli* containing selected RNAi construct. Two generations were produced on RNAi plates before population synchronisation by egg-laying with F_2 gravid adults. The offspring of these egg-lays developed to adulthood on RNAi plates and were used in experiments at the appropriate age.

5.2.3 Thermotolerance Assay

Strains were synchronised by egg-laying. For each condition, three biological replicates of 50 L4 animals were plated onto fresh NGM agar plates and allowed to develop to day 1 of adulthood. Animals were either exposed to 37°C heat shock for 2 and 4 hours or 35°C for 4 and 6 hours and left at 20°C for 16 hours to recover. Plates were subsequently scored for survival based on movement, pharyngeal pumping, transparency, and head shape. Survival was calculated as a percentage and significance measured by two-way ANOVA.

5.2.4 RNA Extraction, cDNA Synthesis, and quantitative PCR (qPCR)

For each biological replicate, approximately 200 *C. elegans* synchronised to day 1 of adulthood were collected using pre-cooled RNAase-free water from NGM agar plates. Samples were washed three times in pre-cooled RNAase-free water and pelleted at 1000 x g for 1 minutes. The pellet was transferred to a clean Eppendorf and frozen at -80°C. 50 µL of TRIzol (guanidium thiocyanate) was added to each sample, and subsequently homogenized on ice for using a motorised pellet grinder.

The RNA was extracted from each sample using the Direct-zol RNA purification kit (Zymo Research), consequent RNA concentration and purification was measured by nanodrop. 100 ng of high-quality RNA, measured using a Qubit™ 4 Fluorometer (Invitrogen™), was reverse transcribed into cDNA using the iScript cDNA synthesis kit (Bio-Rad) and stored at 4°C. Quantitative PCR was executed in a real-time PCR detection system (Bio-Rad CFX Connect Real-Time System), using the equivalent of 5 ng of cDNA, 200 nM of the appropriate forward and

reverse primers, and 1X SYBR green super-mix (Bio-Rad). The expression level for each gene was determined using the delta-delta C_t method, and the significance of the results was measured by two-way ANOVA.

5.2.5 Primers Used for qPCR

cdc-42	F	5' TGTCGGTAAAACTTGTCTCCTG 3'
cdc-42	R	5' ATCCTAATGTGTATGGCTCGC 3'
hsf-1	F	5' GGACACAAATGGGCTCAATG 3'
hsf-1	R	5' CGCAAAAGTCTATTTCCAGCAC 3'
hsp-70	F	5' CGGTATTTATCAAAATGGAAAGGTT 3'
hsp-70	R	5' TACGAGCGGCTTGATCTTTT 3'
hsp-90	F	5' GACCAGAAACCCAGACGATATC 3'
hsp-90	R	5' GAAGAGCACGGAATTCAAGTTG 3'

The housekeeping gene *cdc-42* was used for these experiments, and F signifies forward primers while R indicates the reverse primers.

5.3 Results

5.3.1 HSP-90 Knock Down Induces TCS-mediated *hsp-70* upregulation

Endogenous levels of *hsp-90* mRNA are decreased when HSP-90 is knocked down in the intestine (hsp-90^{int}) compared to the control strain at 20°C; however, this decrease is not observed when HSP-90 is knocked down in the neurones (hsp-90^{neu}) at 20°C. Changes in relative *hsp-90* mRNA are only detectable in the hsp-90^{int} strain as the intestine is a larger tissue than the neurones, the change is likely so slight in the hsp-90^{neu} strain it is not detectable (Figure 37A). Following 4 hours of heat shock at 37°C, wild-type *C. elegans* N2 and hsp-90^{control} animals display reduced survival, approximately 5% and 8% respectively (Figure 37A). However, the survival of hsp-90^{int} animals was roughly double that of control animals, while hsp-90^{neu} animals did not show this improved survival (Figure 37B), supporting the relative *hsp-90* mRNA expression in this strain (Figure 37A). This data indicates that tissue-specific knockdown of *hsp-90* in the intestine could induce a systemic organismal protective effect, but not the method by which this occurs.

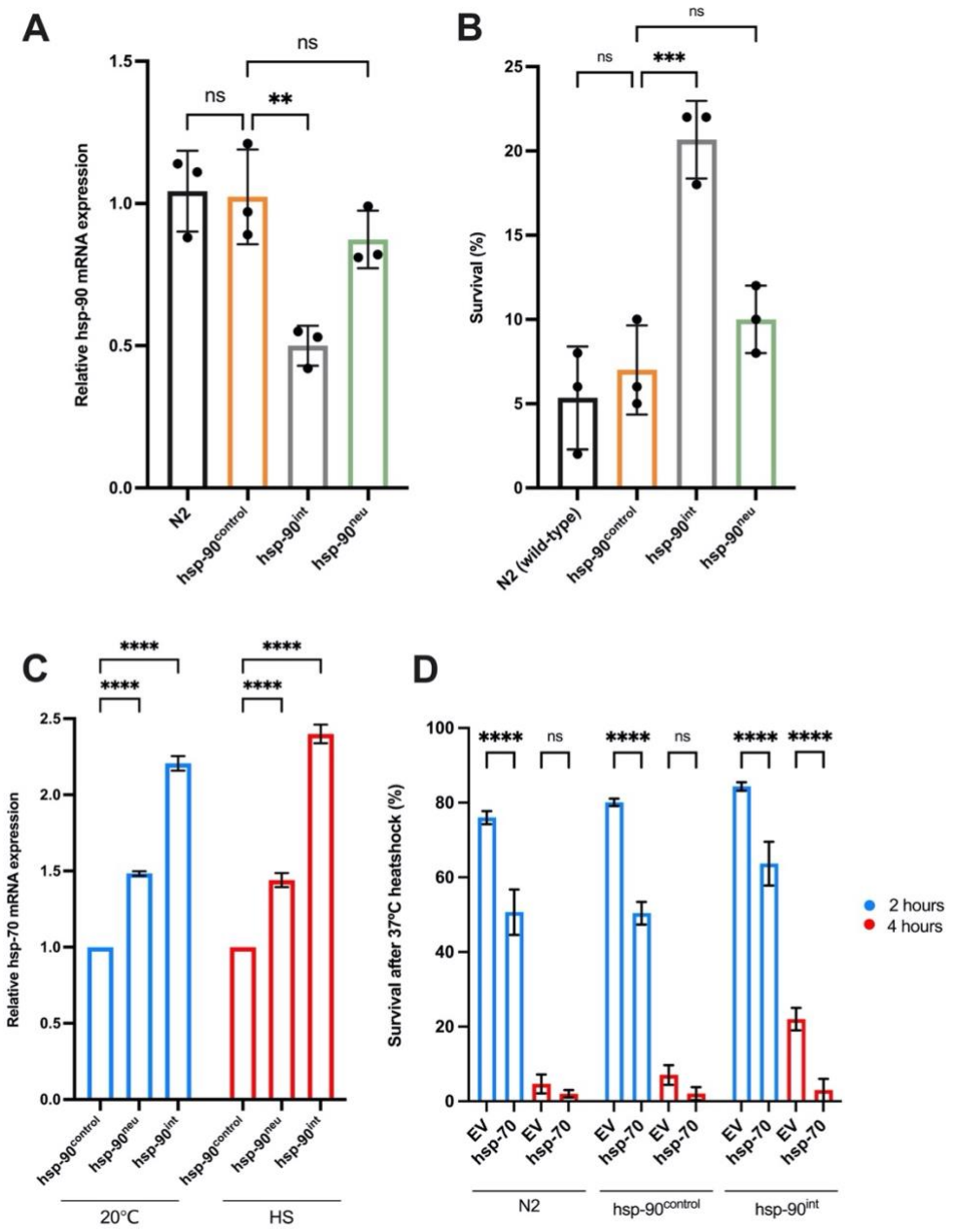

Figure 37. TCS induces *hsp-70* cell-non-autonomously in muscle cells and increases lifespan and stress resistance. (A) Whole-animal *hsp-90* mRNA levels in hsp-90^{int} and hsp-90^{neuro} animals compared to hsp-90^{control}. (B) Thermotolerance following 4 hours of heat shock at 37°C. (C) Whole-animal *hsp-70* mRNA levels of hsp-90^{int} and hsp-90^{neuro} animals compared to hsp-90^{control} nematodes at 20°C and after a 1 hour of heat shock at 35°C. (D) Thermotolerance of empty vector control (EV) RNAi and *hsp-70* RNAi treated

animals following 4 hours of heat shock at 37°C. (A, C) Bar graphs represent 3 biological replicates of 200 animals per strain and/or temperature condition. (B, D) Bar graphs represent 3 biological replicates of 50 animals per condition. (A – D) Significance compared to hsp-90^{control} and determined using two-way ANOVA * P < 0.05; ** P < 0.01; *** P < 0.001; **** P < 0.0001; ns = not significant. Error bars represent SEM of the 3 biological replicates.

Tissue-specific knockdown of *hsp-90* in the intestine or the neurones has been shown to increase the expression of *hsp-70* through cell-non-autonomous upregulation (Miles, Scherz-Shouval and Van Oosten-Hawle, 2019); this was confirmed by RT-qPCR of hsp-90^{int} and hsp-90^{neu} strains. Knocking down *hsp-90* in the neurones or intestine increased endogenous *hsp-70* mRNA 1.5-fold and 2.2-fold respectively at 20°C, additionally, transcription was unaffected by heat stress (Figure 37C). This indicated knocking down *hsp-90* in the intestine or neurones is upregulating *hsp-70* through cell-non-autonomous HSR mediated TCS. This hypothesis was further tested by measuring the thermotolerance of the animals which showed that hsp-90^{int} animals had a reduced survival after 4 hours of heat shock at 37ºC after knocking down *hsp-70* by RNAi feeding compared to empty vector control. This indicates that increased *hsp-70* levels are critical to survival (Figure 37D).

5.3.2 TCS is not Dependent on HSF-1

Cell-autonomous HSR is regulated by the transcription factor HSF-1, to elucidate a pathway it was beneficial to examine if the proposed method of HSR mediated TCS in hsp-90^{int} animals was dependent on HSF-1. In *C. elegans* the *hsf-*

1(sy441) allele is a loss-of-function point mutation in the *hsf-1* gene that inhibits the transcriptional activity of HSF-1. By arresting the function of HSF-1, researchers can investigate stress pathways independently of the canonical heat shock response. This strain was crossed with *hsp-90* knock down strains. Following heat shock at 37°C, hsf-1 (sy441) and hsf-1::hsp-90^{control} animals exhibited reduced survival rates of 55% and 65% respectively after 2 hours, and 5% and 10% after 4 hours (Figure 38A). The survival rate significantly improved in hsf-1::hsp-90^{int} to 85% after 2 hours and 35% after 4 hours (Figure 38A), a 15% increase compared to hsp-90^{int} (Figure 38B).

Knocking down *hsp-90* in the intestine and inactivating HSF-1 increases endogenous *hsp-70* mRNA expression 2.3-fold at 20°C and 3.0-fold after 1 hour of heat shock at 35°C (Figure 38B), compared to a 2.2-fold increase when HSF-1 is active (Figure 38B). When HSF-1 was active, hsp-90^{neu} animals did not show increased survival rates following heat shock (Figure 38A), however once HSF-1 transcription was inactive the survival rates of hsp-90^{neu} animals increases to 80% and 50% following heat shock at 37°C for 2 and 4 hours respectively (Figure 38A). Furthermore, knocking down *hsp-90* in the neurones induced *hsp-70* mRNA levels 2.5-fold and 3.3-fold at 20°C and following heat shock (Figure 38A). These results indicate that tissue specific knock down of *hsp-90* mediates up-regulation of *hsp-70* levels by TCS independent of HSF-1 activity. Furthermore, HSF-1 acts as a suppressor of this mechanisms of TCS indicating a separate mediating pathway distinct from the canonical HSF-1 mediated HSR.

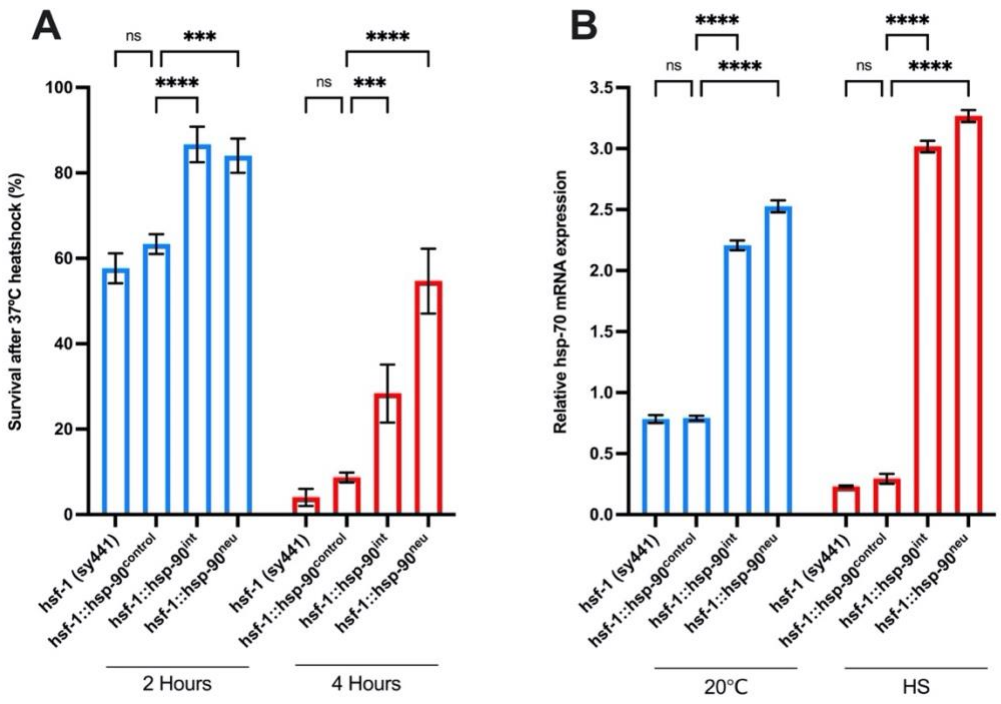

Figure 38. TCS-induced hsp-70 expression is regulated independently of HSF-1. (A) Survival of hsf-1::hsp-90^{int} and hsf-1::hsp-90^{neu} animals compared to hsf-1::hsp-90^{control} after a 2- and 4-hours of heat shock at 37°C. (B) Whole-animal *hsp-70* mRNA levels of hsf-1::hsp-90^{int} and hsf-1::hsp-90^{neu} animals compared to hsf-1::hsp-90^{control} before and after 1-hour of heat shock at 35°C. (A, B) Bar graphs represent the average of 3 biological replicates of (A) 50 and (B) 200 animals per condition. Error bars represent SEM of the 3 biological replicates. Significance compared to hsp-90^{control} was determined using two-way ANOVA * $P < 0.05$; ** $P < 0.01$; *** $P < 0.001$; **** $P < 0.0001$; ns = not significant.

5.3.3 *txt-1* is required for TCS-mediated *hsp-70*

To elucidate the pathway at play, Dr Jay Miles performed transcriptional profiling followed by a forward genetic mutagenesis screen to pinpoint candidate genes essential for TCS. The RNA-seq profiling of HSP-90 knockdown and control

strains identified 17 candidate genes that were up-regulated in hsp-90^{int} and hsp-90^{neu} compared to N2 and hsp-90^{control} which were named the *txt* genes. A tissue-specific candidate RNAi screen of the intestine and muscle was employed to determine in which tissue the *txt* candidate genes act to mediate TCS. The intestine-specific RNAi screen found four genes *txt-1, txt-21, txt-7,* and *rack-1* as intestine-specific suppressors of TCS-mediated *hsp-70* induction in the muscle**.** The body wall muscle specific RNAi screen found three genes functioning as muscle-specific suppressors txt-1*, ceh-58, and txt-4*. Furthermore, there were six genes functioning as enhancers of TCS-mediated *hsp-70* expression in the muscle: *txt-5, txt-8, txt-12, txt-13, txt-14* and *dlat-1*.

The *txt-1* gene raised specific interest as it seemed to play a role as a muscle-specific enhancer and an intestine-specific suppressor of TCS-mediated *hsp-70* expression (see Miles Fig 4B and 4C), suggesting a significant role for *txt-1* in TCS. Furthermore, the transcription factor *ceh-58* is a direct and known interactor of *txt-1 and* was selected as a potentially important candidate for this reason. To explore the role of *txt-1* and *ceh-58* in the mechanism of HSR mediated TCS in *hsp-90* knock down models, animals were subjected to tissue-specific single and double RNAi of *hsf-1*, *txt-1* and *ceh-58* genes to measure *hsp-70* induction at 20ºC and HS, and thermotolerance of hsp-90^{int} animals. As expected, the *hsp-70* mRNA levels of the *hsf-1* RNAi systemic control strain are reduced after heat shock (Figure 39A) and the survival rates are reduced to 5% after heat shock at 35°C for 6 hours (Figure 39B). Knocking down endogenous *txt-1* or *ceh-58* gene expression in the systemic control strain increases endogenous *hsp-70* mRNA levels 6-fold and 8-fold respectively, both before and after heat shock (Figure 39A). Additionally, knocking down *ceh-58* and *txt-1* genes

improves the survival rates of system control animals to 25% after 6 hours of heat shock at 35°C (Figure 39B). These results indicate that in a TCS inactive strain, canonical HSR is mediated by HSF-1 and supressed by TXT-1 and CEH-58.

Muscle-specific knock down of *txt-1* or *ceh-58* genes in hsp-90^{int} animals reduced thermotolerance by 50% (Figure 39D) and decreased endogenous *hsp-70* mRNA levels, both at permissive temperature and following heat shock (Figure 39C). Conversely, muscle-specific *hsf-1* RNAi increases *hsp-70* transcripts 1.5-fold and 6.5-fold in hsp-90^{int} animals, at 20°C and after heat shock respectively (Figure 39C) and improves heat shock survival rates to 50% (Figure 39D). This data corroborates the hypothesis that the transcellular signalling components TXT-1 and CEH-58 act as initiators of HSR-mediated, TCS-induced *hsp-70* expression in muscle cells that is critical for heat stress survival. Furthermore, while HSF-1 acts as a suppressor of TCS, when there is a simultaneous knock down of the *ceh-58* or *txt-1* genes the suppressive role of HSF-1 is eradicated. This implies the regulation of HSF-1 suppressive activity relies on interplay between the transcellular signalling components and HSF-1.

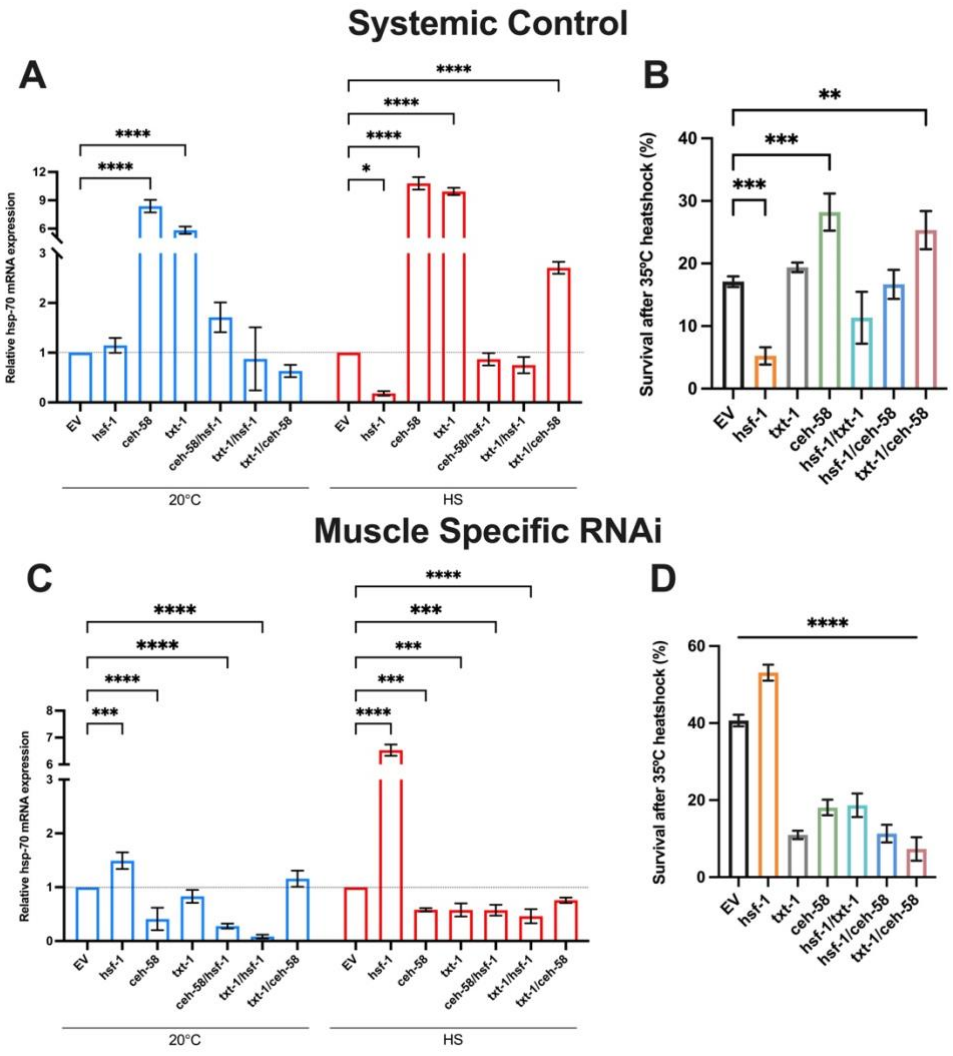

Figure 39. *txt-1* is required for TCS-mediated *hsp-70* induction during HS independent of HSF-1. (A) *txt-1* and *ceh-58* are suppressors of the HSR. Quantification of whole- animal *hsp-70* transcripts in control animals at 20 ℃ and HS (35 ℃), allowing for systemic RNAi against *hsf-1*, *ceh-58*, *txt-1*, and double RNAi of *hsf-1/ceh-58 hsf-1/txt-1*, *txt-1/ceh-58*. (C) TCS-mediated *hsp-70* induction is facilitated by *txt-1* and *ceh-58* in the muscle. Quantification of whole animal *hsp-70* transcripts in *hsp-90*^{int} animals at 20 ℃ and HS (35 ℃), during muscle-specific RNAi against *hsf-1*, *ceh-58*, *txt-1*, and double RNAi of *hsf-1/ceh-58 hsf-1/txt-1*, *txt- 1/ceh-58*. (B, D) Thermotolerance after 6-h of heat stress at 35 ℃ of TCS active strains during muscle-specific RNAi and intestine-

specific RNAi compared to a control strain during systemic RNAi against *hsf-1*, *ceh-58*, *txt-1*, and double RNAi of *hsf-1/ceh-58 hsf-1/txt-1*, *txt-1/ ceh-58*. (A – D) Bar graphs represent the average of 3 biological replicates of (B, D) 50 and (A, C) 200 animals per condition. Error bars represent SEM of the 3 biological replicates. Significance compared to EV control was determined using two-way ANOVA * P < 0.05; ** P < 0.01; *** P < 0.001; **** P < 0.0001; ns = not significant.

5.3.4 Extracellular Peptides are Involved in TCS Signalling

As described previously, Dr Jay Miles did a body wall muscle specific RNAi screen and found three genes functioning as muscle-specific suppressors (*txt-1*, *ceh-58*, and *txt-4*) and six genes functioning as enhancers of TCS-mediated hsp-70 expression in the muscle (*txt-5*, *txt-8*, *txt-12*, *txt-13*, *txt-14* and *dlat-1*). Dr Miles used the DeepLoc 1.0 web tool to estimate the subcellular localization of TXT-4, TXT-5, TXT-8, TXT-12, and TXT-14, which predicted the peptides ranging from 5 – 16 kDa could be present in the body wall muscle, as extracellular, soluble peptides.

To explore their role in mediating TCS in the hsp-90^{int} strain, thermotolerance and *hsp-70* mRNA levels were measured following intestine- and muscle-specific knock down of the extracellular peptides. Systemically, knocking down all the genes of extracellular peptides, except *txt-14*, decreased *hsp-70* transcript levels were following heat shock, indicating the extracellular peptides play a role in canonical HSR (Figure 40A). Opposing results are observed following intestine-specific knockdown of extracellular peptides.

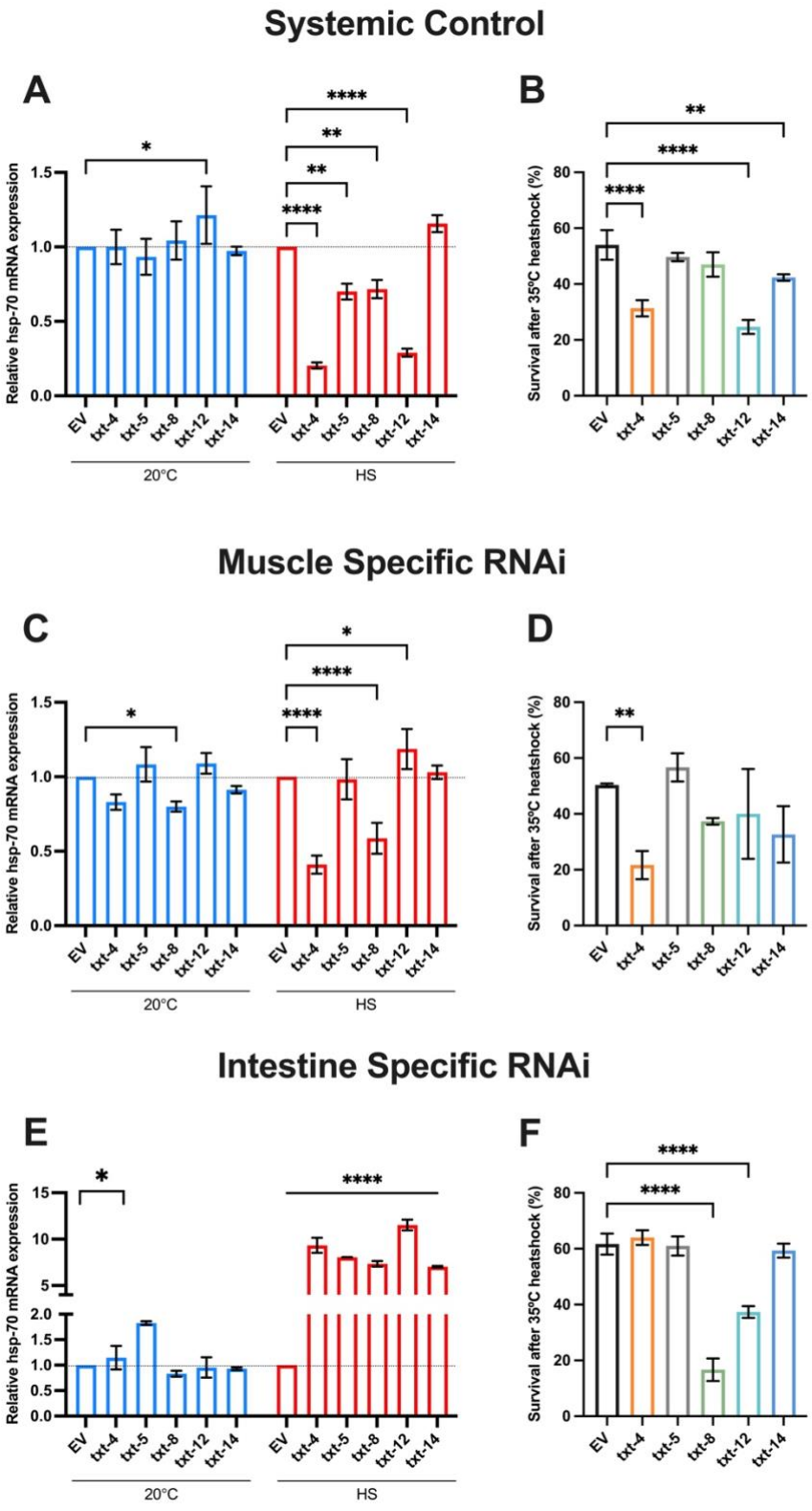

Figure 40. Extracellular peptides are involved in TCS signalling from the intestine to the muscle. (A, C, E) Whole-animal *hsp-70* mRNA levels of (A) systemic control animals, and hsp-90^{int} animals during (C) muscle- and (E)

intestine-specific RNAi against txt-4, txt-5, txt-8, txt- 12, and txt-14 compared to EV control RNAi. Day 1 adults were collected for transcript quantification before and after 1-hour of heat shock at 35°C. (B, D, F) Thermotolerance of (B) systemic control strain, hsp-90int during (D) muscle- and (F) intestine-specific RNAi against txt-4, txt-5, txt-8, txt- 12, and txt-14 compared to EV control RNAi. Day 1 adults were exposed to a 6-h heat shock at 35 ℃. (A – F) Bar graphs represent the average of 3 biological replicates of (B, D, F) 50 and (A, C, E) 200 animals per condition. Error bars represent SEM of the 3 biological replicates. Significance compared to EV control was determined using two-way ANOVA * P < 0.05; ** P < 0.01; *** P < 0.001; **** P < 0.0001; ns = not significant.

The hsp-70 mRNA levels are increased approximately 10-fold following the knock down of all extracellular peptides (Figure 40E), however knocking down *txt-8* and *txt-12* genes reduces the survival rate of hsp-90^{int} animals (Figure 40F). This suggests that the inhibitory function of TXT-1 and CEH-58 and extracellular peptides TXT-8 and TXT-12 in the intestine are required for TCS mediated regulation of survival but may also implicate the extracellular peptides in another stress response pathway, complicating interpretation of the results.

The mRNA levels of *hsp-70* are decreased in hsp-90^{int} animals upon muscle-specific knock down of *txt-4* and *txt-8* genes. This indicates the extracellular peptides TXT-4 and TXT-8 act as regulators of TCS-mediated *hsp-70* induction in the muscle of hsp-90^{int} (Figure 40C) and increase the survival rates of following animals following heat shock at 35°C for 6 hours (Figure 40D). This suggests that

both TXT-4 and TXT-8 could function as transmitters of TCS from the intestine to the muscle.

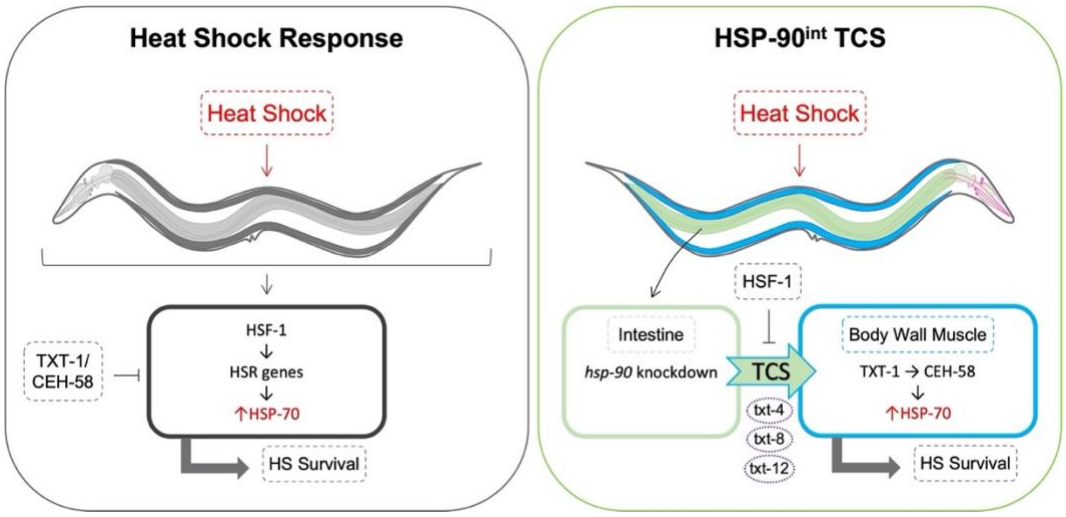

Figure 41. A schematic outlining the suggested mechanism for opposing HSP-70 regulation by HSR or TCS. Upon *hsp-90* RNAi in the intestine ("TCS-active") hsp-70 is induced in the muscle via an hsf-1-independent mechanism that depends on TXT-1/CEH-58 signalling in the muscle as well as extracellular peptides TXT-4, TXT-8, and TXT-12. HSF-1 functions as a suppressor of TCS-mediated hsp-70 expression and survival. (B) In control animals ("TCS-inactive"), cell nonautonomous hsp-70 induction and survival depends on HSF-1 and extracellular peptides TXT-4 and TXT-12 during HS; and is suppressed by TXT-1/CEH-58. HSF-1, heat shock factor 1; TCS, transcellular chaperone signalling.

These results describe the effect of knocking down *hsp-90* in the intestine of *C. elegans* initiates a novel pathway of intestine-to-muscle TCS signalling to improve heat stress survival and organismal health (Figure 41). Beyond the context of this work, the functions of extracellular peptides TXT-4, TXT-12, and TXT-14 are

not clear. However, in control strains, HSF-1 mediates the HSR with the assistance of extracellular peptides TXT-4, TXT-12, and TXT-14, however during the canonical HSR heat stress survival is supressed by TXT-1 and CEH-58. Conversely, when *hsp-90* is knocked down in the intestine of *C. elegans*, the gut sends transcellular signals to the muscle cells with the support of extracellular peptides TXT-4, TXT-8, and TXT-12. Once the signal is received by the body wall muscle, the membrane-associated TXT-1 signals to the transcription factor CEH-58 in the nucleus, which up-regulates the expression of HSP-70 to promote heat stress survival independent of HSF-1 activity. Taken together, this data determines that TCS and the HSF-1-mediated HSR are regulated in an antagonistic manner, where TCS supresses HSF-1 activity and HSF-1 inhibits TCS-induced TXT-1/CEH-58 signalling.

5.4 Discussion

Knocking down *hsp-90* in the intestine of *C. elegans* initiates a transcellular signal that triggers the expression of HSP-70 in the body wall muscle through via a novel signalling pathway. The transcellular-cross-tissue genes and the homeodomain transcription factor CEH-58 act as intermediaries in the transmission of signals from the gut to muscle cells. Notably, CEH-58 localised in the body wall muscle was identified to play a crucial role in the induction of *hsp-70* by TCS, while HSF-1, surprisingly, functions as a suppressor of this pathway. Conversely, CEH-58 suppresses the induction of *hsp-70* and the survival response to heat stress in control strains. From this data it can be concluded that the TCS signalling pathway and cell-autonomous HSR operate antagonistically, and there is a mechanism at play which can differentiate between intestine-specific *hsp-90* knockdown-induced stress, and environmental heat stress for organismal protection.

Inter-tissue signalling originating from the intestine can be initiated to establish communication with other tissues, whether in response to pathogenic infections (Chikka *et al.*, 2016; Ewbank and Pujol, 2016; Peterson *et al.*, 2019) or as part of the FOXO-to-FOXO signalling pathway, which extends lifespan through the release of lipid signals from the intestines (Zhang *et al.*, 2013). Intriguingly, the intestine's role in mediating such signalling has been relatively understudied in the context of cellular stress responses and the cell-non-autonomous induction of molecular chaperones. This data delves into the investigation of intestine induced inter-tissue signalling, leading to the enhanced expression of HSP-70 in muscle cells.

Small molecule drugs like Radicicol and Tanespimycin (Janssens *et al.*, 2019) induce HSP-90 inhibition in *C. elegans* improving the animal's resistance to heat stress and extended lifespan (Eckl *et al.*, 2017). Notably, these beneficial effects are only observed if HSP-90 is inhibited at or after the L4 larval stage of development. Earlier systemic *hsp-90* knockdown causes developmental arrest and dauer formation (Somogyvári, Gecse and Sőti, 2018; Janssens *et al.*, 2019) while in contrast, consistently knocking down *hsp-90* in the intestine by RNAi from the embryonic stages can function without any accompanying developmental abnormalities. This underscores the notable distinctions between systemic and tissue-specific *hsp-90* knock down and suggests that the intestinal function of *hsp-90* may not be necessary during the early stages of *C. elegans* development (Hajdu-Cronin, Chen and Sternberg, 2004; Gaiser *et al.*, 2011).

Remarkably, the knockdown of *hsp-90* in the intestine does not necessitate the involvement of HSF-1 for inducing HSP-70 expression in the body wall muscle of *C. elegans*. Typically, reducing HSP-90 activity triggers the HSF-1-mediated expression of heat-inducible HSP-70, however intestine-specific knockdown of hsp-90 induced HSP-70 expression is supressed by HSF-1 (Wu, 1995; Zou *et al.*, 1998). These observations suggest that achieving the appropriate response in the correct target tissue at an organismal level may necessitate more intricate layers of regulation, for example by adopting an alternative transcription factor, such as CEH-58. This underscores the importance that organismal proteostasis via cell-type-specific stress responses are likely regulated by a specific "tissue-code" in *C. elegans*. The presence of a tissue-code is highly probable, considering the distinctive expression patterns of molecular chaperones in various human tissues,

as well as the specialised chaperone networks designed to address specific conditions such as neurodegenerative diseases (Brehme *et al.*, 2014) and cancer (Hadizadeh Esfahani *et al.*, 2018).

Several transcription factors, apart from HSF-1, have been recognized for their role in regulating molecular chaperones and HSPs. These include SKN-1/NRF2, FOXO/DAF-16, PHA-4, and PQM-1 (Lindquist, 1986; Hsu, Murphy and Kenyon, 2003; Tepper *et al.*, 2013; Blackwell *et al.*, 2015; O'Brien *et al.*, 2018; Shpigel *et al.*, 2019). While CEH-58 has not been previously associated with chaperone expression, the data described in this chapter strongly suggests a genetic interaction between CEH-58 and HSF-1. These results, in conjunction with the presence of a CEH-58 predicted binding site within the *hsp-70* promoter should be explored further to verify if there is direct binding of CEH-58 to DNA elements in the promoters of HSPs. Future studies could endeavour to explore the prospective co-regulation of HSR genes by direct protein-protein interactions between both CEH-58 and HSF-1.

The TCS pathway differentiates itself from canonical HSF-1-mediated HSR on multiple fronts. Firstly, intestine-specific *hsp-90* knockdown induced TCS depends on CEH-58 for heat stress resistance in *C. elegans* but more significantly, the TCS-induced transcriptional profile is distinct from HSF-1 regulated HSR. When *C. elegans* experience external heat stress, HSF-1-dependent heat shock proteins typically rank among the most highly upregulated genes, however, induction of TCS in the intestine results in a notable upregulation of innate immune response genes (Brunquell *et al.*, 2016). Furthermore, HSF-1-mediated HSR seems to be deactivated upon induction of TCS in hsp-90^{int} animals opting

for the TXT-1/CEH-58 mediated induction of HSP-70 in the body wall muscle for organismal survival. These opposing effects could plausibly be attributed to an inherent negative regulatory mechanism designed to safeguard the organism during cellular stress

Alongside CEH-58, TXT-1 has been introduced another crucial player in the intestine-induced TCS signalling pathway. TXT-1 is predicted to be localised at the cell membrane of muscle and neuronal cells, mirroring the expression pattern of CEH-58. TXT-1 is a PDZ domain containing protein, which functions as a signalling scaffold, which binds multiple signalling components, and promotes their communication for efficient and specific signal transduction at defined subcellular sites (Nourry, Grant and Borg, 2003; Roh and Margolis, 2003). Here, TXT-1 is thought to receive extracellular signals and begin the intracellular pathway by interacting with CEH-58, aligning with earlier findings from a yeast-two-hybrid study that unveiled their direct interaction (Lenfant *et al.*, 2010). While this data is the first to establish a connection between TXT-1 and the heat stress response in *C. elegans*, DLG5, the closest human orthologue functions as a membrane-associated guanylate cyclase and contributes to the cellular response to heat stress as a component of the Hippo pathway (Zhu, Shang and Zhang, 2016; Luo *et al.*, 2020; Venugopal *et al.*, 2020).

Extracellular peptides can play a significant role in maintaining organismal proteostasis by facilitating intercellular communication (Melo and Ruvkun, 2012). Within the array of extracellular peptides identified as potential intestine-induced TCS mediators by Dr Jay Miles, TXT-4 stands out as a predicted extracellular lipase expressed in the intestine (Cao *et al.*, 2017), which plays a

pivotal role in the response to heat stress in both in control and TCS strains. TXT-4 acts as an enhancer of *hsp-70* upregulation in muscle cells, while it functions in the intestine as a suppressor, possibly serving as a negative feedback mechanism essential for the transmission of stress signals from the intestine to the body wall muscle in *C. elegans*. The extracellular peptide TXT-8 is a phospholipase previously identified as one of the 57 extracellular proteostasis regulators in *C. elegans*, implicated in autophagy and another noteworthy mediator of TCS (Gallotta *et al.*, 2020). Regarding their potential involvement in intercellular stress signalling, future investigations may be directed toward the roles of these extracellular peptides as proteostasis regulators of cell-non-autonomous stress responses (Gallotta *et al.*, 2020). Notably, lipid signals have previously been proposed as integral components of FOXO-to-FOXO signalling, linking the intestine to the body wall muscle (Zhang *et al.*, 2013). This suggests a broader role for lipases like TXT-4 and TXT-8 in mediating intercellular stress signalling.

In summary, this research underscores the significance of transcellular signalling between the intestine and muscle, which triggers a stress response in the body wall muscle of *C. elegans* independent of HSF-1. From these data it can be proposed that the contrasting effects observed between TCS and the HSF-1 mediated HSR are part of a negative regulatory system that ultimately enhances the likelihood of organismal survival by fine-tuning stress responses in the most effective way. Gaining deeper insights into the signalling components orchestrating global stress responses initiated in the intestine and communicating with other tissues becomes pivotal for potential interventions aimed at enhancing overall organismal health.

While this study primarily focused on signalling from the intestine to the body wall muscle, it is plausible, perhaps likely, that similar signalling mechanisms exist in intestine to brain communication, which could have profound implications for the treatment of neurodegenerative diseases. For instance, intestine-to-brain signalling in mammals plays a vital role in the development of age-related neurodegenerative conditions like Alzheimer's and Parkinson's disease. This occurs as a result of the influence of gut microbiota on the progression of these diseases (Jin *et al.*, 2019; Hertzberg *et al.*, 2022), along with the mammalian brain's ability to detect various stimuli from the intestine, whether they are mechanical, chemical, or related to bacteria. These signals are transmitted through intestine-released hormones and neurotransmitters (Kaelberer *et al.*, 2020). Consequently, the intestine can directly affect the evolutionarily conserved maintenance of organismal proteostasis. To fully leverage the potential therapeutic possibilities arising from this intercellular communication, future research should be done to identify the signals exchanged between the intestine and other organs.

Chapter 6. Final Discussion

6.1 Overview of Chapter Findings

Chapter 3: This chapter investigated the effects of HSP-90 over-expression on TCS activation to protect against neuronal or muscular $A\beta_{1-42}$ in *C. elegans*. In strains expressing fluorescently tagged $A\beta_{1-42}$ in the body wall muscle, over-expressing HSP-90 in the same or distal tissues significantly improves the motility, lifespan, and fecundity defects. This reflects the findings in previously published work, and further work would need to be done to explore the specific pathway. In strains expressing fluorescently tagged $A\beta_{1-42}$ in the neurones, over-expressing HSP-90 induces inter-tissue signalling from the intestine to neurons, thereby protecting against $A\beta_{1-42}$ aggregation. This is a novel pathway, which would require further work to identify the key components (see 6.21).

Chapter 4: This chapter presents a workflow for the sample preparation and cryogenic electron tomography on an adult *C. elegans* AD model. Adult *C. elegans* samples were vitrified for the first time by high pressure freezing and deposits were targeted for cryo-sectioning using cryo-CLEM. The resulting 3D reconstructions unveiled the macromolecular features of adult *C. elegans* tissue and offered insights into the molecular architecture of $A\beta_{1-42}$ fibrils. These fibrils were found to be organized into parallel bundles, in proximity to ribosomes and microtubules.

Chapter 5: When HSP-90 is depleted in the intestine TCS signalling to muscle cells is initiated, leading to the activation of HSP-70 expression, and aiding in

TCS-mediated heat stress resistance and lifespan extension. The RNA-seq profiling of HSP-90 knockdown and control strains identified 17 candidate genes that were up-regulated in hsp-90^{int} and hsp-90^{neu} compared to N2 and hsp-90^{control} which were named the *txt* genes. Using RNAi to knock down these specific genes to identify the pathway at play. The PDZ-domain guanylate cyclase TXT-1 and the homeobox transcription factor CEH-58 are pivotal signalling hubs, with extracellular peptides TXT-4 and TXT-8 serving as trans-tissue signals.

This research has highlighted the mechanisms by which two opposing HSP-90 TCS pathways function. Future research could investigate if, at any point, these two pathways converge and if the regulators of opposing mechanisms are affected in the different pathways. When HSP-90 is knocked down in the intestine, HSP-70 is upregulated by TCS via an hsf-1-independent mechanism that depends on TXT-1/CEH-58 signalling in the muscle as well as extracellular peptides TXT-4, TXT-8, and TXT-12 (Figure 41). In the future it would be interesting to explore how TXT-1 and CEH-58 are affected when HSP-90 is over-expressed in the intestine. When HSP-90 is overexpressed in the intestine of animals expressing $A\beta_{1-42}$ in the neurones, the toxic effects usually observed in this strain are ameliorated. The mechanism by which this occurs, and the potential role TXT-1 and CEH-58 play, is currently unknown. This could be investigated by knocking down the *txt*-1 and *ceh-58* genes by RNAi and measuring the chemotaxis of animals expressing HSP-90 in the intestine and $A\beta_{1-42}$ in the neurones. The same method could be used to find out if the extracellular peptides TXT-4, TXT-8, and TXT-12 are the transcellular signals in this pathway.

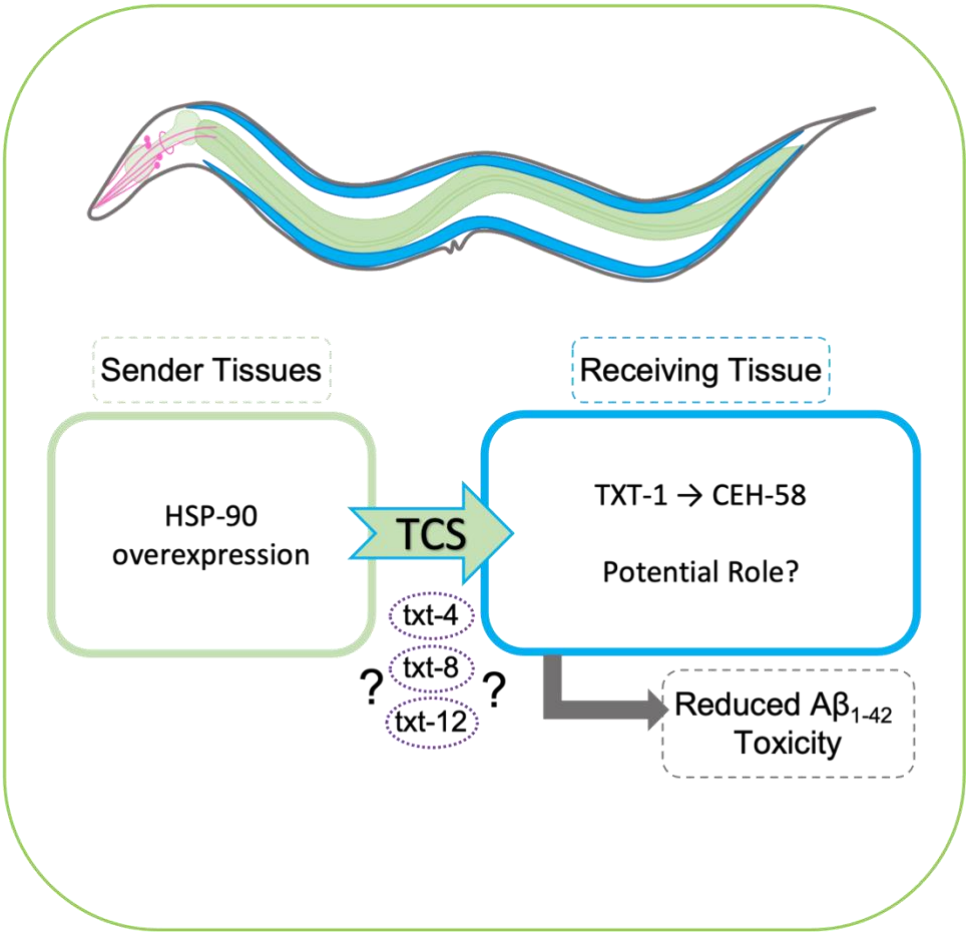

Figure 42. Potential convergence of opposing HSP-90 TCS pathways. A schematic proposing potential aspects of opposing HSP-90 TCS pathways for future exploration. Specifically highlighting the potential roles of extracellular peptides TXT-4, TXT-8, and TXT-12 in HSP-90 overexpression mediated TCS pathways. Additionally, it examines how overexpressing HSP-90 may affect TXT-1 and CEH-58 activity, and its implications on TCS and $A\beta_{1\text{-}42}$ toxicity.

6.2 Future Work

6.2.1 Transcellular Chaperone Signalling

While the mechanisms and pathways involved in TCS against toxic $A\beta_{1-42}$ have been explored in earlier *C. elegans* models of AD, this knowledge has yet to be translated into more up-to-date *C. elegans* AD models. In Chapter 3, the data demonstrated that the over-expression of HSP-90 induces inter-tissue signalling, originating from the intestine and extending to neurons, which effectively protects against $A\beta_{1-42}$ aggregation. Delving deeper into the intricacies of these intercellular signalling interactions, particularly focusing on the communication from the intestine to neurons, offers a promising avenue for future therapeutic strategies aimed at bolstering brain homeostasis as individuals age. To harness the full potential of these therapeutic possibilities emerging from intercellular communication, future research efforts should aim to identify the specific signals exchanged between the intestine and other organs. The RNA-seq profiling of HSP-90 knockdown and control strains identified 17 *txt* genes that were up-regulated in hsp-90^{int} and hsp-90^{neu} compared to N2 and hsp-$90^{control}$, however very little is known about these genes or proteins. Uncovering this information, perhaps by utilising bioinformatics and examining sequence similarity, may provide clues which help to identify the method by which transcellular signals are sent and received during TCS.

Chapter 5 explores how HSP-90 depletion in the intestine triggers TCS signalling to muscle cells, leading to the activation of HSP-70 expression, and playing a crucial role in TCS-mediated heat stress resistance and extended lifespan.

Although CEH-58's involvement in chaperone expression had not been previously established, the data presented in this chapter strongly suggests a genetic interaction between CEH-58 and HSF-1. These findings, coupled with the presence of a CEH-58 consensus sequence within the *hsp-70* promoter, warrant further exploration to confirm whether CEH-58 directly binds to DNA elements in the promoters of HSPs. Subsequent studies should endeavour to investigate the potential co-regulation of HSR genes through direct protein-protein interactions between CEH-58 and HSF-1 using co-immunoprecipitation (co-IP) or pull-down assays.

In the context of their potential roles in intercellular stress signalling, future investigations may be directed toward understanding the functions of extracellular peptides as regulators of proteostasis in cell-non-autonomous stress responses. It is worth noting that lipid signals have previously been proposed as integral components of FOXO-to-FOXO signalling, establishing connections between the intestine and body wall muscle. This hints at a broader role for lipases like TXT-4 and TXT-8 in mediating intercellular stress signalling which should be explored further in the future.

6.2.2 CEMOVIS and Cryo-ET of *C. elegans*

Chapter 4 describes a workflow for the sample preparation and cryo-ET on an adult *C. elegans* AD model, samples were vitrified by high pressure freezing and deposits were targeted for cryo-sectioning. HPF of adult *C. elegans* was a major bottle neck in the workflow, and while optimisation helped, further work should be done to improve the vitrification of adult *C. elegans*. Looking ahead, it is

possible that future advancements in tubing options rather than carriers, such as offering a wider range of diameters, could render this method more viable for freezing adult *C. elegans*. Additionally, HPF of *C. elegans* using the waffle method, opens the door for other methods of cryo-sectioning, such as FIB-milling, to increase the throughput of viable cryo-EM grids. Due to time constraints, optimisation of the freezing process for *C. elegans* using the waffle method was not possible. However, it remains a viable avenue for exploration in future research endeavours.

Due to time constraints, only one tomogram containing fibrils was collected. In the future, further tomograms, ideally data collected from the tissue of at least three animals, should be collected give insights into the native architecture of $A\beta_{1-42}$ aggregates in their native tissue environment. Through subtomogram averaging, tomograms containing tau fibrils have achieved resolutions of approximately 10 Å (Gilbert *et al.*, 2023). In the future, there is potential to apply this technique for advanced structural investigations involving adult *C. elegans*. However, it's important to note that only a limited number of research laboratories currently possess the necessary equipment and expertise to conduct such studies.

References

Al Adem, K. and Lee, S. (2023) 'Structural polymorphism and cytotoxicity of brain-derived ß-amyloid extracts', *Protein Science*, 32(5), p. e4639. Available at: https://doi.org/10.1002/pro.4639.

Al-Amoudi, A. *et al.* (2004) 'Cryo-electron microscopy of vitreous sections', *The EMBO Journal*, 23(18), pp. 3583–3588. Available at: https://doi.org/10.1038/sj.emboj.7600366.

Al-Amoudi, A., Norlen, L.P.O. and Dubochet, J. (2004) 'Cryo-electron microscopy of vitreous sections of native biological cells and tissues', *Journal of Structural Biology*, 148(1), pp. 131–135. Available at: https://doi.org/10.1016/j.jsb.2004.03.010.

Almeida, Z.L. and Brito, R.M.M. (2020) 'Structure and Aggregation Mechanisms in Amyloids', *Molecules*, 25(5), p. 1195. Available at: https://doi.org/10.3390/molecules25051195.

Alzheimer, A. (1906) 'Über einen eigenartigen schweren Erkrankungsprozeß der Hirnrincle', *Neurol. Central*, 25, p. 1134.

Alzheimer, A. (1907) 'Über eine eigenartige Erkrankung der Hirnrinde', *Allg. Z. Psychiatr. Psych.-Gerichtl. Med.*, 641, pp. 46–48.

Ananthan, J., Goldberg, A.L. and Voellmy, R. (1986) 'Abnormal Proteins Serve as Eukaryotic Stress Signals and Trigger the Activation of Heat Shock Genes', *Science*, 232(4749), pp. 522–524. Available at: https://doi.org/10.1126/science.3083508.

Anfinsen, C.B. *et al.* (1961) 'The Kinetics of Formation of Native Ribonuclease During Oxidation of the Reduced Polypeptide Chain', *Proceedings of the National Academy of Sciences*, 47(9), pp. 1309–1314. Available at: https://doi.org/10.1073/pnas.47.9.1309.

Bae, Y.-K. (2008) 'Sensory roles of neuronal cilia: Cilia development, morphogenesis, and function in C. elegans', *Frontiers in Bioscience*, Volume(13), p. 5959. Available at: https://doi.org/10.2741/3129.

Bai, X. *et al.* (2013) 'Ribosome structures to near-atomic resolution from thirty thousand cryo-EM particles', *eLife*, 2, p. e00461. Available at: https://doi.org/10.7554/eLife.00461.

Berger, C. *et al.* (2023) 'Cryo-electron tomography on focused ion beam lamellae transforms structural cell biology', *Nature Methods*, 20(4), pp. 499–511. Available at: https://doi.org/10.1038/s41592-023-01783-5.

Berkowitz, L.A. *et al.* (2008) 'Generation of Stable Transgenic C. elegans Using Microinjection', *Journal of Visualized Experiments*, (18), p. 833. Available at: https://doi.org/10.3791/833.

Bernstein, S.L. *et al.* (2009) 'Amyloid-ß protein oligomerization and the importance of tetramers and dodecamers in the aetiology of Alzheimer's disease', *Nature Chemistry*, 1(4), pp. 326–331. Available at: https://doi.org/10.1038/nchem.247.

Betzig, E. *et al.* (2006) 'Imaging Intracellular Fluorescent Proteins at Nanometer Resolution', *Science*, 313(5793), pp. 1642–1645. Available at: https://doi.org/10.1126/science.1127344.

Billings, L.M. *et al.* (2005) 'Intraneuronal Aβ Causes the Onset of Early Alzheimer's Disease-Related Cognitive Deficits in Transgenic Mice', *Neuron*, 45(5), pp. 675–688. Available at: https://doi.org/10.1016/j.neuron.2005.01.040.

Birnby, D.A. *et al.* (2000) 'A Transmembrane Guanylyl Cyclase (DAF-11) and Hsp90 (DAF-21) Regulate a Common Set of Chemosensory Behaviors in *Caenorhabditis elegans*', *Genetics*, 155(1), pp. 85–104. Available at: https://doi.org/10.1093/genetics/155.1.85.

Blackwell, T.K. *et al.* (2015) 'SKN-1/Nrf, stress responses, and aging in Caenorhabditis elegans', *Free Radical Biology and Medicine*, 88, pp. 290–301. Available at: https://doi.org/10.1016/j.freeradbiomed.2015.06.008.

Brehme, M. *et al.* (2014) 'A Chaperome Subnetwork Safeguards Proteostasis in Aging and Neurodegenerative Disease', *Cell Reports*, 9(3), pp. 1135–1150. Available at: https://doi.org/10.1016/j.celrep.2014.09.042.

Brenner, S. (1974) 'THE GENETICS OF *CAENORHABDITIS ELEGANS*', *Genetics*, 77(1), pp. 71–94. Available at: https://doi.org/10.1093/genetics/77.1.71.

Brenner, S. (1988) *The Nematode Caenorhabditis elegans*. Cold Spring Harbor Laboratory Press.

Briggs, J.A. (2013) 'Structural biology in situ—the potential of subtomogram averaging', *Current Opinion in Structural Biology*, 23(2), pp. 261–267. Available at: https://doi.org/10.1016/j.sbi.2013.02.003.

Brunquell, J. *et al.* (2016) 'The genome-wide role of HSF-1 in the regulation of gene expression in Caenorhabditis elegans', *BMC Genomics*, 17(1), p. 559. Available at: https://doi.org/10.1186/s12864-016-2837-5.

Buckingham, S.D. and Sattelle, D.B. (2009) 'Fast, automated measurement of nematode swimming (thrashing) without morphometry', *BMC Neuroscience*, 10(1), p. 84. Available at: https://doi.org/10.1186/1471-2202-10-84.

Buzzard, E. *et al.* (2023) *Cryo-electron tomography of* C. elegans *mitochondria reveals how the ATP synthase dimer interface shapes crista membranes*. preprint. Biochemistry. Available at: https://doi.org/10.1101/2023.02.02.526626.

Callaway, E. (2020) 'Revolutionary cryo-EM is taking over structural biology', *Nature*, 578(7794), pp. 201–201. Available at: https://doi.org/10.1038/d41586-020-00341-9.

Cao, J. *et al.* (2017) 'Comprehensive single-cell transcriptional profiling of a multicellular organism', *Science*, 357(6352), pp. 661–667. Available at: https://doi.org/10.1126/science.aam8940.

Chaudhuri, J., Parihar, M. and Pires-daSilva, A. (2011) 'An Introduction to Worm Lab: from Culturing Worms to Mutagenesis', *Journal of Visualized Experiments*, (47), p. 2293. Available at: https://doi.org/10.3791/2293.

Chikka, M.R. *et al.* (2016) 'The Mitochondria-Regulated Immune Pathway Activated in the C. elegans Intestine Is Neuroprotective', *Cell Reports*, 16(9), pp. 2399–2414. Available at: https://doi.org/10.1016/j.celrep.2016.07.077.

Chiti, F. and Dobson, C.M. (2009) 'Amyloid formation by globular proteins under native conditions', *Nature Chemical Biology*, 5(1), pp. 15–22. Available at: https://doi.org/10.1038/nchembio.131.

Chlanda, P. and Sachse, M. (2014) 'Cryo-electron Microscopy of Vitreous Sections', in J. Kuo (ed.) *Electron Microscopy*. Totowa, NJ: Humana Press (Methods in

Molecular Biology), pp. 193–214. Available at: https://doi.org/10.1007/978-1-62703-776-1_10.

Chow, V.W. *et al.* (2010) 'An Overview of APP Processing Enzymes and Products', *NeuroMolecular Medicine*, 12(1), pp. 1–12. Available at: https://doi.org/10.1007/s12017-009-8104-z.

Conte, D. *et al.* (2015) 'RNA Interference in *Caenorhabditis elegans*', *Current Protocols in Molecular Biology*, 109(1). Available at: https://doi.org/10.1002/0471142727.mb2603s109.

Cotella, D. *et al.* (2012) 'Toxic Role of K^+ Channel Oxidation in Mammalian Brain', *The Journal of Neuroscience*, 32(12), pp. 4133–4144. Available at: https://doi.org/10.1523/JNEUROSCI.6153-11.2012.

Cras, P. *et al.* (1991) 'Senile plaque neurites in Alzheimer disease accumulate amyloid precursor protein.', *Proceedings of the National Academy of Sciences*, 88(17), pp. 7552–7556. Available at: https://doi.org/10.1073/pnas.88.17.7552.

Cruts, M., Theuns, J. and Van Broeckhoven, C. (2012) 'Locus-specific mutation databases for neurodegenerative brain diseases', *Human Mutation*, 33(9), pp. 1340–1344. Available at: https://doi.org/10.1002/humu.22117.

Cuanalo-Contreras, K. *et al.* (2023) 'Extensive accumulation of misfolded protein aggregates during natural aging and senescence', *Frontiers in Aging Neuroscience*, 14, p. 1090109. Available at: https://doi.org/10.3389/fnagi.2022.1090109.

Da Silva, V.C.H. and Ramos, C.H.I. (2012) 'The network interaction of the human cytosolic 90kDa heat shock protein Hsp90: A target for cancer therapeutics',

Journal of Proteomics, 75(10), pp. 2790–2802. Available at: https://doi.org/10.1016/j.jprot.2011.12.028.

Dearborn, A.D. *et al.* (2016) 'α-Synuclein Amyloid Fibrils with Two Entwined, Asymmetrically Associated Protofibrils', *Journal of Biological Chemistry*, 291(5), pp. 2310–2318. Available at: https://doi.org/10.1074/jbc.M115.698787.

Diomede, L. *et al.* (2012) 'C. elegans Expressing Human ß2-Microglobulin: A Novel Model for Studying the Relationship between the Molecular Assembly and the Toxic Phenotype', *PLoS ONE*. Edited by E.M.C. Skoulakis, 7(12), p. e52314. Available at: https://doi.org/10.1371/journal.pone.0052314.

Divan, A. and Royds, J. (eds) (2013) *Tools and techniques in biomolecular science*. Oxford: Oxford University Press.

Dobro, M.J. *et al.* (2010) 'Plunge Freezing for Electron Cryomicroscopy', in *Methods in Enzymology*. Elsevier, pp. 63–82. Available at: https://doi.org/10.1016/S0076-6879(10)81003-1.

Dobson, C.M. (2004) 'Principles of protein folding, misfolding and aggregation', *Seminars in Cell & Developmental Biology*, 15(1), pp. 3–16. Available at: https://doi.org/10.1016/j.semcdb.2003.12.008.

Dubey, A. *et al.* (2015) 'Heat shock proteins: a therapeutic target worth to consider', *Veterinary World*, 8(1), pp. 46–51. Available at: https://doi.org/10.14202/vetworld.2015.46-51.

Dubochet, J. *et al.* (1988) 'Cryo-electron microscopy of vitrified specimens', *Quarterly Reviews of Biophysics*, 21(2), pp. 129–228. Available at: https://doi.org/10.1017/S0033583500004297.

Duff, K. *et al.* (1996) 'Increased amyloid-β42(43) in brains of mice expressing mutant presenilin 1', *Nature*, 383(6602), pp. 710–713. Available at: https://doi.org/10.1038/383710a0.

Eckl, J. *et al.* (2017) 'Hsp90-downregulation influences the heat-shock response, innate immune response and onset of oocyte development in nematodes', *PLOS ONE*. Edited by D. Picard, 12(10), p. e0186386. Available at: https://doi.org/10.1371/journal.pone.0186386.

Egelman, E.H. (2015) 'Three-dimensional reconstruction of helical polymers', *Archives of Biochemistry and Biophysics*, 581, pp. 54–58. Available at: https://doi.org/10.1016/j.abb.2015.04.004.

Eichner, T. *et al.* (2011) 'Conformational Conversion during Amyloid Formation at Atomic Resolution', *Molecular Cell*, 41(2), pp. 161–172. Available at: https://doi.org/10.1016/j.molcel.2010.11.028.

Eisenmann, D.M. (2005) 'Wnt signaling', *WormBook* [Preprint]. Available at: https://doi.org/10.1895/wormbook.1.7.1.

Englander, S.W. and Mayne, L. (2017) 'The case for defined protein folding pathways', *Proceedings of the National Academy of Sciences*, 114(31), pp. 8253–8258. Available at: https://doi.org/10.1073/pnas.1706196114.

European Alzheimer's Disease Initiative (EADI) *et al.* (2013) 'Meta-analysis of 74,046 individuals identifies 11 new susceptibility loci for Alzheimer's disease', *Nature Genetics*, 45(12), pp. 1452–1458. Available at: https://doi.org/10.1038/ng.2802.

Ewbank, J.J. and Pujol, N. (2016) 'Local and long-range activation of innate immunity by infection and damage in C. elegans', *Current Opinion in Immunology*, 38, pp. 1–7. Available at: https://doi.org/10.1016/j.coi.2015.09.005.

Fatt, H.V. and Dougherty, E.C. (1963) 'Genetic Control of Differential Heat Tolerance in Two Strains of the Nematode *Caenorhabditis elegans*', *Science*, 141(3577), pp. 266–267. Available at: https://doi.org/10.1126/science.141.3577.266.

Fonte, V. *et al.* (2002) 'Interaction of intracellular ß amyloid peptide with chaperone proteins', *Proceedings of the National Academy of Sciences*, 99(14), pp. 9439–9444. Available at: https://doi.org/10.1073/pnas.152313999.

Fonte, V. *et al.* (2008) 'Suppression of in Vivo ß-Amyloid Peptide Toxicity by Overexpression of the HSP-16.2 Small Chaperone Protein', *Journal of Biological Chemistry*, 283(2), pp. 784–791. Available at: https://doi.org/10.1074/jbc.M703339200.

Frauenfelder, H., Sligar, S.G. and Wolynes, P.G. (1991) 'The Energy Landscapes and Motions of Proteins', *Science*, 254(5038), pp. 1598–1603. Available at: https://doi.org/10.1126/science.1749933.

Freeman, B.C. and Morimoto, R.I. (no date) 'The human cytosolic molecular chaperones hsp90, hsp70 (hsc70) and hdj-1 have distinct roles in recognition of a non-native protein and protein refolding.', *The EMBO Journal*, 15(12), pp. 2969–2979.

Friedreich, N. and Kekulé, A. (1859) 'Zur amyloidfrage', *Virchows Arch*, 16(50), pp. 50–65.

Gaiser, A.M. *et al.* (2011) 'Downregulation of the Hsp90 System Causes Defects in Muscle Cells of Caenorhabditis Elegans', *PLoS ONE*. Edited by E.A.A. Nollen, 6(9), p. e25485. Available at: https://doi.org/10.1371/journal.pone.0025485.

Gallotta, I. *et al.* (2020) 'Extracellular proteostasis prevents aggregation during pathogenic attack', *Nature*, 584(7821), pp. 410–414. Available at: https://doi.org/10.1038/s41586-020-2461-z.

Gallrein, C. *et al.* (2021) 'Novel amyloid-beta pathology C. elegans model reveals distinct neurons as seeds of pathogenicity', *Progress in Neurobiology*, 198, p. 101907. Available at: https://doi.org/10.1016/j.pneurobio.2020.101907.

Garwood, C.J. *et al.* (2017) 'Review: Astrocytes in Alzheimer's disease and other age-associated dementias: a supporting player with a central role', *Neuropathology and Applied Neurobiology*, 43(4), pp. 281–298. Available at: https://doi.org/10.1111/nan.12338.

Ge, P. and Zhou, Z.H. (2011) 'Hydrogen-bonding networks and RNA bases revealed by cryo electron microscopy suggest a triggering mechanism for calcium switches', *Proceedings of the National Academy of Sciences*, 108(23), pp. 9637–9642. Available at: https://doi.org/10.1073/pnas.1018104108.

Geddes, A.J. *et al.* (1968) '"Cross-ß" conformation in proteins', *Journal of Molecular Biology*, 32(2), pp. 343–358. Available at: https://doi.org/10.1016/0022-2836(68)90014-4.

Ghosh, U. *et al.* (2021) 'Structural differences in amyloid-ß fibrils from brains of nondemented elderly individuals and Alzheimer's disease patients', *Proceedings of the National Academy of Sciences*, 118(45), p. e2111863118. Available at: https://doi.org/10.1073/pnas.2111863118.

Gilbert, M.A.G. *et al.* (2023) In situ *cryo-electron tomography of β-amyloid and tau in post-mortem Alzheimer's disease brain*. preprint. Pathology. Available at: https://doi.org/10.1101/2023.07.17.549278.

Golden, J.W. and Riddle, D.L. (1984) 'The Caenorhabditis elegans dauer larva: Developmental effects of pheromone, food, and temperature', *Developmental Biology*, 102(2), pp. 368–378. Available at: https://doi.org/10.1016/0012-1606(84)90201-X.

Gómez-Orte, E. *et al.* (2018) 'Effect of the diet type and temperature on the *C. elegans* transcriptome', *Oncotarget*, 9(11), pp. 9556–9571. Available at: https://doi.org/10.18632/oncotarget.23563.

Gremer, L. *et al.* (2017) 'Fibril structure of amyloid-ß(1–42) by cryo–electron microscopy', *Science*, 358(6359), pp. 116–119. Available at: https://doi.org/10.1126/science.aao2825.

Ha, N.M. *et al.* (2022) 'Caenorhabditis elegans as a powerful tool in natural product bioactivity research', *Applied Biological Chemistry*, 65(1), p. 18. Available at: https://doi.org/10.1186/s13765-022-00685-y.

Hadizadeh Esfahani, A. *et al.* (2018) 'A systematic atlas of chaperome deregulation topologies across the human cancer landscape', *PLOS Computational Biology*. Edited by E. Wang, 14(1), p. e1005890. Available at: https://doi.org/10.1371/journal.pcbi.1005890.

Hajdu-Cronin, Y.M., Chen, W.J. and Sternberg, P.W. (2004) 'The L-Type Cyclin CYL-1 and the Heat-Shock-Factor HSF-1 Are Required for Heat-Shock-Induced Protein Expression in Caenorhabditis elegans', *Genetics*, 168(4), pp. 1937–1949. Available at: https://doi.org/10.1534/genetics.104.028423.

Hampel, H. *et al.* (2021) 'The Amyloid-ß Pathway in Alzheimer's Disease', *Molecular Psychiatry*, 26(10), pp. 5481–5503. Available at: https://doi.org/10.1038/s41380-021-01249-0.

Hampton, C.M. *et al.* (2017) 'Correlated fluorescence microscopy and cryo-electron tomography of virus-infected or transfected mammalian cells', *Nature Protocols*, 12(1), pp. 150–167. Available at: https://doi.org/10.1038/nprot.2016.168.

Han, R., Zhang, F. and Gao, X. (2018) 'A fast fiducial marker tracking model for fully automatic alignment in electron tomography', *Bioinformatics*. Edited by R. Murphy, 34(5), pp. 853–863. Available at: https://doi.org/10.1093/bioinformatics/btx653.

Harding, H.P. *et al.* (2000) 'Regulated Translation Initiation Controls Stress-Induced Gene Expression in Mammalian Cells', *Molecular Cell*, 6(5), pp. 1099–1108. Available at: https://doi.org/10.1016/S1097-2765(00)00108-8.

Hartl, F.U., Bracher, A. and Hayer-Hartl, M. (2011) 'Molecular chaperones in protein folding and proteostasis', *Nature*, 475(7356), pp. 324–332. Available at: https://doi.org/10.1038/nature10317.

van Oosten-Hawle, P., Porter, R.S. and Morimoto, R.I. (2013) 'Regulation of Organismal Proteostasis by Transcellular Chaperone Signaling', *Cell*, 153(6), pp. 1366–1378. Available at: https://doi.org/10.1016/j.cell.2013.05.015.

Haynes, C.M. *et al.* (2010) 'The Matrix Peptide Exporter HAF-1 Signals a Mitochondrial UPR by Activating the Transcription Factor ZC376.7 in C. elegans', *Molecular Cell*, 37(4), pp. 529–540. Available at: https://doi.org/10.1016/j.molcel.2010.01.015.

Hell, S.W. and Wichmann, J. (1994) 'Breaking the diffraction resolution limit by stimulated emission: stimulated-emission-depletion fluorescence microscopy', *Optics Letters*, 19(11), p. 780. Available at: https://doi.org/10.1364/OL.19.000780.

Henderson, R. *et al.* (1990) 'Model for the structure of bacteriorhodopsin based on high-resolution electron cryo-microscopy', *Journal of Molecular Biology*, 213(4), pp. 899–929. Available at: https://doi.org/10.1016/S0022-2836(05)80271-2.

Hertzberg, V.S. *et al.* (2022) 'Gut microbiome differences between amyotrophic lateral sclerosis patients and spouse controls', *Amyotrophic Lateral Sclerosis and Frontotemporal Degeneration*, 23(1–2), pp. 91–99. Available at: https://doi.org/10.1080/21678421.2021.1904994.

Hetz, C. and Papa, F.R. (2018) 'The Unfolded Protein Response and Cell Fate Control', *Molecular Cell*, 69(2), pp. 169–181. Available at: https://doi.org/10.1016/j.molcel.2017.06.017.

Hipp, M.S., Kasturi, P. and Hartl, F.U. (2019) 'The proteostasis network and its decline in ageing', *Nature Reviews Molecular Cell Biology*, 20(7), pp. 421–435. Available at: https://doi.org/10.1038/s41580-019-0101-y.

Hipp, M.S., Park, S.-H. and Hartl, F.U. (2014) 'Proteostasis impairment in protein-misfolding and -aggregation diseases', *Trends in Cell Biology*, 24(9), pp. 506–514. Available at: https://doi.org/10.1016/j.tcb.2014.05.003.

Hooli, B.V. *et al.* (2012) 'Role of common and rare APP DNA sequence variants in Alzheimer disease', *Neurology*, 78(16), pp. 1250–1257. Available at: https://doi.org/10.1212/WNL.0b013e3182515972.

Hornsten, A. *et al.* (2007) 'APL-1, a *Caenorhabditis elegans* protein related to the human ß-amyloid precursor protein, is essential for viability', *Proceedings of the National Academy of Sciences*, 104(6), pp. 1971–1976. Available at: https://doi.org/10.1073/pnas.0603997104.

Hover, S. *et al.* (2023) 'Organisation of the orthobunyavirus tripodal spike and the structural changes induced by low pH and K+ during entry', *Nature Communications*, 14(1), p. 5885. Available at: https://doi.org/10.1038/s41467-023-41205-w.

Hsu, A.-L., Murphy, C.T. and Kenyon, C. (2003) 'Regulation of Aging and Age-Related Disease by DAF-16 and Heat-Shock Factor', *Science*, 300(5622), pp. 1142–1145. Available at: https://doi.org/10.1126/science.1083701.

Iadanza, M.G. *et al.* (2018) 'A new era for understanding amyloid structures and disease', *Nature Reviews Molecular Cell Biology*, 19(12), pp. 755–773. Available at: https://doi.org/10.1038/s41580-018-0060-8.

Imanikia, S. *et al.* (2019) 'Neuronal XBP-1 Activates Intestinal Lysosomes to Improve Proteostasis in C. elegans', *Current Biology*, 29(14), pp. 2322-2338.e7. Available at: https://doi.org/10.1016/j.cub.2019.06.031.

Jansen, I.E. *et al.* (2019) 'Genome-wide meta-analysis identifies new loci and functional pathways influencing Alzheimer's disease risk', *Nature Genetics*, 51(3), pp. 404–413. Available at: https://doi.org/10.1038/s41588-018-0311-9.

Janssens, G.E. *et al.* (2019) 'Transcriptomics-Based Screening Identifies Pharmacological Inhibition of Hsp90 as a Means to Defer Aging', *Cell Reports*, 27(2), pp. 467-480.e6. Available at: https://doi.org/10.1016/j.celrep.2019.03.044.

Jin, M. *et al.* (2019) 'Analysis of the Gut Microflora in Patients With Parkinson's Disease', *Frontiers in Neuroscience*, 13, p. 1184. Available at: https://doi.org/10.3389/fnins.2019.01184.

Johnstone, I.L. (1994) 'The cuticle of the nematodeCaenorhabditis elegans: A complex collagen structure', *BioEssays*, 16(3), pp. 171–178. Available at: https://doi.org/10.1002/bies.950160307.

Jovaisaite, V., Mouchiroud, L. and Auwerx, J. (2014) 'The mitochondrial unfolded protein response, a conserved stress response pathway with implications in health and disease', *Journal of Experimental Biology*. Edited by S.A. Davies, J.A.T. Dow, and K. Lukowiak, 217(1), pp. 137–143. Available at: https://doi.org/10.1242/jeb.090738.

Jun, S. *et al.* (2019) 'Advances in Cryo-Correlative Light and Electron Microscopy: Applications for Studying Molecular and Cellular Events', *The Protein Journal*, 38(6), pp. 609–615. Available at: https://doi.org/10.1007/s10930-019-09856-1.

Kaelberer, M.M. *et al.* (2020) 'Neuropod Cells: The Emerging Biology of Gut-Brain Sensory Transduction', *Annual Review of Neuroscience*, 43(1), pp. 337–353. Available at: https://doi.org/10.1146/annurev-neuro-091619-022657.

Kamath, R. (2003) 'Genome-wide RNAi screening in Caenorhabditis elegans', *Methods*, 30(4), pp. 313–321. Available at: https://doi.org/10.1016/S1046-2023(03)00050-1.

Kampinga, H.H. and Craig, E.A. (2010) 'The HSP70 chaperone machinery: J proteins as drivers of functional specificity', *Nature Reviews Molecular Cell Biology*, 11(8), pp. 579–592. Available at: https://doi.org/10.1038/nrm2941.

Kawamura, K. and Maruyama, I.N. (2019) 'Forward Genetic Screen for *Caenorhabditis elegans* Mutants with a Shortened Locomotor Healthspan', *G3 Genes|Genomes|Genetics*, 9(8), pp. 2415–2423. Available at: https://doi.org/10.1534/g3.119.400241.

Kim, D.H. (2018) 'Signaling in the innate immune response', *WormBook*, pp. 1–35. Available at: https://doi.org/10.1895/wormbook.1.83.2.

Kirstein, J. *et al.* (2017) '*In vivo* properties of the disaggregase function of J-proteins and Hsc70 in *Caenorhabditis elegans* stress and aging', *Aging Cell*, 16(6), pp. 1414–1424. Available at: https://doi.org/10.1111/acel.12686.

Kobro-Flatmoen, A., Nagelhus, A. and Witter, M.P. (2016) 'Reelin-immunoreactive neurons in entorhinal cortex layer II selectively express intracellular amyloid in early Alzheimer's disease', *Neurobiology of Disease*, 93, pp. 172–183. Available at: https://doi.org/10.1016/j.nbd.2016.05.012.

Kohler, V. and Andréasson, C. (2020) 'Hsp70-mediated quality control: should I stay or should I go?', *Biological Chemistry*, 401(11), pp. 1233–1248. Available at: https://doi.org/10.1515/hsz-2020-0187.

Kollmer, M. *et al.* (2019) 'Cryo-EM structure and polymorphism of Aß amyloid fibrils purified from Alzheimer's brain tissue', *Nature Communications*, 10(1), p. 4760. Available at: https://doi.org/10.1038/s41467-019-12683-8.

Kramer, J.M. *et al.* (1990) 'The Caenorhabditis elegans rol-6 gene, which interacts with the sqt-1 collagen gene to determine organismal morphology, encodes a collagen.', *Molecular and Cellular Biology*, 10(5), pp. 2081–2089. Available at: https://doi.org/10.1128/MCB.10.5.2081.

Kremer, J.R., Mastronarde, D.N. and McIntosh, J.R. (1996) 'Computer Visualization of Three-Dimensional Image Data Using IMOD', *Journal of Structural Biology*, 116(1), pp. 71–76. Available at: https://doi.org/10.1006/jsbi.1996.0013.

Kuwahara, T. *et al.* (2008) 'A systematic RNAi screen reveals involvement of endocytic pathway in neuronal dysfunction in α-synuclein transgenic C . elegans', *Human Molecular Genetics*, 17(19), pp. 2997–3009. Available at: https://doi.org/10.1093/hmg/ddn198.

Labbadia, J. and Morimoto, R.I. (2015) 'The Biology of Proteostasis in Aging and Disease', *Annual Review of Biochemistry*, 84(1), pp. 435–464. Available at: https://doi.org/10.1146/annurev-biochem-060614-033955.

Lackie, R.E. *et al.* (2017) 'The Hsp70/Hsp90 Chaperone Machinery in Neurodegenerative Diseases', *Frontiers in Neuroscience*, 11, p. 254. Available at: https://doi.org/10.3389/fnins.2017.00254.

Lam, V. and Villa, E. (2021) 'Practical Approaches for Cryo-FIB Milling and Applications for Cellular Cryo-Electron Tomography', in T. Gonen and B.L. Nannenga (eds) *cryoEM*. New York, NY: Springer US (Methods in Molecular Biology), pp. 49–82. Available at: https://doi.org/10.1007/978-1-0716-0966-8_3.

Lambert, M.P. *et al.* (1998) 'Diffusible, nonfibrillar ligands derived from Aß $_{1–42}$ are potent central nervous system neurotoxins', *Proceedings of the National Academy of Sciences*, 95(11), pp. 6448–6453. Available at: https://doi.org/10.1073/pnas.95.11.6448.

Langer, T. *et al.* (1992) 'Successive action of DnaK, DnaJ and GroEL along the pathway of chaperone-mediated protein folding', *Nature*, 356(6371), pp. 683–689. Available at: https://doi.org/10.1038/356683a0.

Lau, W.C.Y. and Rubinstein, J.L. (2013) 'Single Particle Electron Microscopy', in I. Schmidt-Krey and Y. Cheng (eds) *Electron Crystallography of Soluble and Membrane Proteins*. Totowa, NJ: Humana Press (Methods in Molecular Biology), pp. 401–426. Available at: https://doi.org/10.1007/978-1-62703-176-9_22.

Le Breton, L. and Mayer, M.P. (2016) 'A model for handling cell stress', *eLife*, 5, p. e22850. Available at: https://doi.org/10.7554/eLife.22850.

Leistner, C. *et al.* (2023) 'The in-tissue molecular architecture of ß-amyloid pathology in the mammalian brain', *Nature Communications*, 14(1), p. 2833. Available at: https://doi.org/10.1038/s41467-023-38495-5.

Lenfant, N. *et al.* (2010) 'A genome-wide study of PDZ-domain interactions in C. elegans reveals a high frequency of non-canonical binding', *BMC Genomics*, 11(1), p. 671. Available at: https://doi.org/10.1186/1471-2164-11-671.

Li, D. and Wang, M. (2012) 'Construction of a bicistronic vector for the co-expression of two genes in *Caenorhabditis elegans* using a newly identified IRES', *BioTechniques*, 52(3), pp. 173–176. Available at: https://doi.org/10.2144/000113821.

Lindquist, S. (1986) 'The Heat Shock Response', *Annual Review of Biochemistry*, 55(1), pp. 1151–1191. Available at: https://doi.org/10.1146/annurev.bi.55.070186.005443.

Link, C. (2003) 'Gene expression analysis in a transgenic Caenorhabditis elegans Alzheimer's disease model', *Neurobiology of Aging*, 24(3), pp. 397–413. Available at: https://doi.org/10.1016/S0197-4580(02)00224-5.

Link, C.D. (1995) 'Expression of human beta-amyloid peptide in transgenic Caenorhabditis elegans.', *Proceedings of the National Academy of Sciences*, 92(20), pp. 9368–9372. Available at: https://doi.org/10.1073/pnas.92.20.9368.

Link, C.D. *et al.* (2001) 'Visualization of fibrillar amyloid deposits in living, transgenic Caenorhabditis elegans animals using the sensitive amyloid dye, X-34', *Neurobiology of Aging*, 22(2), pp. 217–226. Available at: https://doi.org/10.1016/S0197-4580(00)00237-2.

Liu, C.-C. *et al.* (2013) 'Apolipoprotein E and Alzheimer disease: risk, mechanisms and therapy', *Nature Reviews Neurology*, 9(2), pp. 106–118. Available at: https://doi.org/10.1038/nrneurol.2012.263.

López-Otín, C. *et al.* (2023) 'Hallmarks of aging: An expanding universe', *Cell*, 186(2), pp. 243–278. Available at: https://doi.org/10.1016/j.cell.2022.11.001.

Lučić, V., Förster, F. and Baumeister, W. (2005) 'STRUCTURAL STUDIES BY ELECTRON TOMOGRAPHY: From Cells to Molecules', *Annual Review of Biochemistry*, 74(1), pp. 833–865. Available at: https://doi.org/10.1146/annurev.biochem.73.011303.074112.

Luo, M. *et al.* (2020) 'Heat stress activates YAP/TAZ to induce the heat shock transcriptome', *Nature Cell Biology*, 22(12), pp. 1447–1459. Available at: https://doi.org/10.1038/s41556-020-00602-9.

Madhivanan, K. *et al.* (2018) 'Cellular clearance of circulating transthyretin decreases cell-nonautonomous proteotoxicity in *Caenorhabditis elegans*', *Proceedings of the National Academy of Sciences*, 115(33). Available at: https://doi.org/10.1073/pnas.1801117115.

Mawuenyega, K.G. *et al.* (2010) 'Decreased Clearance of CNS ß-Amyloid in Alzheimer's Disease', *Science*, 330(6012), pp. 1774–1774. Available at: https://doi.org/10.1126/science.1197623.

McColl, G. *et al.* (2009) 'The Caenorhabditis elegans Aß1–42 Model of Alzheimer Disease Predominantly Expresses Aß3–42', *Journal of Biological Chemistry*, 284(34), pp. 22697–22702. Available at: https://doi.org/10.1074/jbc.C109.028514.

McColl, G. *et al.* (2012) 'Utility of an improved model of amyloid-beta (Aß1-42) toxicity in Caenorhabditis elegans for drug screening for Alzheimer's disease', *Molecular Neurodegeneration*, 7(1), p. 57. Available at: https://doi.org/10.1186/1750-1326-7-57.

McDonald, K.L. and Auer, M. (2006) 'High-Pressure Freezing, Cellular Tomography, and Structural Cell Biology', *BioTechniques*, 41(2), pp. 137–143. Available at: https://doi.org/10.2144/000112226.

Melo, J.A. and Ruvkun, G. (2012) 'Inactivation of Conserved C. elegans Genes Engages Pathogen- and Xenobiotic-Associated Defenses', *Cell*, 149(2), pp. 452–466. Available at: https://doi.org/10.1016/j.cell.2012.02.050.

Miles, J. *et al.* (2023) 'Transcellular chaperone signaling is an intercellular stress-response distinct from the HSF-1–mediated heat shock response', *PLOS Biology*. Edited by U.H. Jakob, 21(2), p. e3001605. Available at: https://doi.org/10.1371/journal.pbio.3001605.

Miles, J., Scherz-Shouval, R. and Van Oosten-Hawle, P. (2019) 'Expanding the Organismal Proteostasis Network: Linking Systemic Stress Signaling with the Innate Immune Response', *Trends in Biochemical Sciences*, 44(11), pp. 927–942. Available at: https://doi.org/10.1016/j.tibs.2019.06.009.

Minnerly, J. *et al.* (2017) 'The cell non-autonomous function of ATG-18 is essential for neuroendocrine regulation of Caenorhabditis elegans lifespan', *PLOS Genetics*. Edited by C.T. Murphy, 13(5), p. e1006764. Available at: https://doi.org/10.1371/journal.pgen.1006764.

Mogk, A., Kummer, E. and Bukau, B. (2015) 'Cooperation of Hsp70 and Hsp100 chaperone machines in protein disaggregation', *Frontiers in Molecular Biosciences*, 2. Available at: https://doi.org/10.3389/fmolb.2015.00022.

Morán Luengo, T., Mayer, M.P. and Rüdiger, S.G.D. (2019) 'The Hsp70–Hsp90 Chaperone Cascade in Protein Folding', *Trends in Cell Biology*, 29(2), pp. 164–177. Available at: https://doi.org/10.1016/j.tcb.2018.10.004.

Morley, J.F. *et al.* (2002) 'The threshold for polyglutamine-expansion protein aggregation and cellular toxicity is dynamic and influenced by aging in *Caenorhabditis elegans*', *Proceedings of the National Academy of Sciences*, 99(16), pp. 10417–10422. Available at: https://doi.org/10.1073/pnas.152161099.

Mu, H., Wang, L. and Zhao, L. (2017) 'HSP 90 inhibition suppresses inflammatory response and reduces carotid atherosclerotic plaque formation in ApoE mice', *Cardiovascular Therapeutics*, 35(2), p. e12243. Available at: https://doi.org/10.1111/1755-5922.12243.

Mullaney, B.C. and Ashrafi, K. (2009) 'C. elegans fat storage and metabolic regulation', *Biochimica et Biophysica Acta (BBA) - Molecular and Cell Biology of*

Lipids, 1791(6), pp. 474–478. Available at: https://doi.org/10.1016/j.bbalip.2008.12.013.

Muñoz-Carvajal, F. and Sanhueza, M. (2020) 'The Mitochondrial Unfolded Protein Response: A Hinge Between Healthy and Pathological Aging', *Frontiers in Aging Neuroscience*, 12, p. 581849. Available at: https://doi.org/10.3389/fnagi.2020.581849.

Neupert, W. and Herrmann, J.M. (2007) 'Translocation of Proteins into Mitochondria', *Annual Review of Biochemistry*, 76(1), pp. 723–749. Available at: https://doi.org/10.1146/annurev.biochem.76.052705.163409.

Nillegoda, N.B. *et al.* (2015) 'Crucial HSP70 co-chaperone complex unlocks metazoan protein disaggregation', *Nature*, 524(7564), pp. 247–251. Available at: https://doi.org/10.1038/nature14884.

Nillegoda, N.B., Wentink, A.S. and Bukau, B. (2018) 'Protein Disaggregation in Multicellular Organisms', *Trends in Biochemical Sciences*, 43(4), pp. 285–300. Available at: https://doi.org/10.1016/j.tibs.2018.02.003.

Njume, F.N. *et al.* (2022) 'A lipid transfer protein ensures nematode cuticular impermeability', *iScience*, 25(11), p. 105357. Available at: https://doi.org/10.1016/j.isci.2022.105357.

Nourry, C., Grant, S.G.N. and Borg, J.-P. (2003) 'PDZ Domain Proteins: Plug and Play!', *Science's STKE*, 2003(179). Available at: https://doi.org/10.1126/stke.2003.179.re7.

O'Brien, D. *et al.* (2018) 'A PQM-1-Mediated Response Triggers Transcellular Chaperone Signaling and Regulates Organismal Proteostasis', *Cell Reports*, 23(13), pp. 3905–3919. Available at: https://doi.org/10.1016/j.celrep.2018.05.093.

Ochiishi, T. *et al.* (2016) 'Development of new fusion proteins for visualizing amyloid-ß oligomers in vivo', *Scientific Reports*, 6(1), p. 22712. Available at: https://doi.org/10.1038/srep22712.

van Oosten-Hawle, P. (2023) 'Organismal Roles of Hsp90', *Biomolecules*, 13(2), p. 251. Available at: https://doi.org/10.3390/biom13020251.

Owusu-Ansah, E., Song, W. and Perrimon, N. (2013) 'Muscle Mitohormesis Promotes Longevity via Systemic Repression of Insulin Signaling', *Cell*, 155(3), pp. 699–712. Available at: https://doi.org/10.1016/j.cell.2013.09.021.

Parmenter, C.D. and Nizamudeen, Z.A. (2021) 'Cryo-FIB-lift-out: practically impossible to practical reality', *Journal of Microscopy*, 281(2), pp. 157–174. Available at: https://doi.org/10.1111/jmi.12953.

Perry, M.D. *et al.* (1993) 'Molecular characterization of the her-1 gene suggests a direct role in cell signaling during Caenorhabditis elegans sex determination.', *Genes & Development*, 7(2), pp. 216–228. Available at: https://doi.org/10.1101/gad.7.2.216.

Peterson, N.D. *et al.* (2019) 'The nuclear hormone receptor NHR-86 controls anti-pathogen responses in C. elegans', *PLOS Genetics*. Edited by D.A. Garsin, 15(1), p. e1007935. Available at: https://doi.org/10.1371/journal.pgen.1007935.

Pickett, C.L. and Kornfeld, K. (2013) 'Age-related degeneration of the egg-laying system promotes matricidal hatching in *Caenorhabditis elegans*', *Aging Cell*, 12(4), pp. 544–553. Available at: https://doi.org/10.1111/acel.12079.

Pierson, J. *et al.* (2010) 'Improving the technique of vitreous cryo-sectioning for cryo-electron tomography: Electrostatic charging for section attachment and implementation of an anti-contamination glove box', *Journal of Structural Biology*, 169(2), pp. 219–225. Available at: https://doi.org/10.1016/j.jsb.2009.10.001.

Pinotsi, D. *et al.* (2014) 'Direct Observation of Heterogeneous Amyloid Fibril Growth Kinetics via Two-Color Super-Resolution Microscopy', *Nano Letters*, 14(1), pp. 339–345. Available at: https://doi.org/10.1021/nl4041093.

Porta-de-la-Riva, M. *et al.* (2012) 'Basic Caenorhabditis elegans Methods: Synchronization and Observation', *Journal of Visualized Experiments*, (64), p. 4019. Available at: https://doi.org/10.3791/4019.

Prahlad, V. and Morimoto, R.I. (2011) 'Neuronal circuitry regulates the response of *Caenorhabditis elegans* to misfolded proteins', *Proceedings of the National Academy of Sciences*, 108(34), pp. 14204–14209. Available at: https://doi.org/10.1073/pnas.1106557108.

Prodromou, C. (2016) 'Mechanisms of Hsp90 regulation', *Biochemical Journal*, 473(16), pp. 2439–2452. Available at: https://doi.org/10.1042/BCJ20160005.

Puchtler, H., Sweat, F. and Levine, M. (1962) 'ON THE BINDING OF CONGO RED BY AMYLOID', *Journal of Histochemistry & Cytochemistry*, 10(3), pp. 355–364. Available at: https://doi.org/10.1177/10.3.355.

Pukkila-Worley, R. and Ausubel, F.M. (2012) 'Immune defense mechanisms in the Caenorhabditis elegans intestinal epithelium', *Current Opinion in Immunology*, 24(1), pp. 3–9. Available at: https://doi.org/10.1016/j.coi.2011.10.004.

Pulak, R. and Anderson, P. (1993) 'mRNA surveillance by the Caenorhabditis elegans smg genes.', *Genes & Development*, 7(10), pp. 1885–1897. Available at: https://doi.org/10.1101/gad.7.10.1885.

Pyne, J.D. and Brickman, A.M. (2021) 'The Impact of the COVID-19 Pandemic on Dementia Risk: Potential Pathways to Cognitive Decline', *Neurodegenerative Diseases*, 21(1–2), pp. 1–23. Available at: https://doi.org/10.1159/000518581.

Queitsch, C., Sangster, T.A. and Lindquist, S. (2002) 'Hsp90 as a capacitor of phenotypic variation', *Nature*, 417(6889), pp. 618–624. Available at: https://doi.org/10.1038/nature749.

Raizen, D.M. *et al.* (2008) 'Lethargus is a Caenorhabditis elegans sleep-like state', *Nature*, 451(7178), pp. 569–572. Available at: https://doi.org/10.1038/nature06535.

Read, A. and Schröder, M. (2021) 'The Unfolded Protein Response: An Overview', *Biology*, 10(5), p. 384. Available at: https://doi.org/10.3390/biology10050384.

Ritossa, F. (1962) 'A new puffing pattern induced by temperature shock and DNP in drosophila', *Experientia*, 18(12), pp. 571–573. Available at: https://doi.org/10.1007/BF02172188.

Roh, M.H. and Margolis, B. (2003) 'Composition and function of PDZ protein complexes during cell polarization', *American Journal of Physiology-Renal*

Physiology, 285(3), pp. F377–F387. Available at: https://doi.org/10.1152/ajprenal.00086.2003.

Rose, A.M. and Baillie, D.L. (1979) 'A mutation in Caenorhabditis elegans that increases recombination frequency more than threefold', *Nature*, 281(5732), pp. 599–600. Available at: https://doi.org/10.1038/281599a0.

Rousseau, F., Serrano, L. and Schymkowitz, J.W.H. (2006) 'How Evolutionary Pressure Against Protein Aggregation Shaped Chaperone Specificity', *Journal of Molecular Biology*, 355(5), pp. 1037–1047. Available at: https://doi.org/10.1016/j.jmb.2005.11.035.

Rüdiger, S., Buchberger, A. and Bukau, B. (1997) 'Interaction of Hsp70 chaperones with substrates', *Nature Structural & Molecular Biology*, 4(5), pp. 342–349. Available at: https://doi.org/10.1038/nsb0597-342.

Rust, M.J., Bates, M. and Zhuang, X. (2006) 'Sub-diffraction-limit imaging by stochastic optical reconstruction microscopy (STORM)', *Nature Methods*, 3(10), pp. 793–796. Available at: https://doi.org/10.1038/nmeth929.

Rutherford, S.L. and Lindquist, S. (1998) 'Hsp90 as a capacitor for morphological evolution', *Nature*, 396(6709), pp. 336–342. Available at: https://doi.org/10.1038/24550.

Satyal, S.H. *et al.* (1998) 'Negative regulation of the heat shock transcriptional response by HSBP1', *Genes & Development*, 12(13), pp. 1962–1974. Available at: https://doi.org/10.1101/gad.12.13.1962.

Schaffer, M. *et al.* (2015) 'Cryo-focused Ion Beam Sample Preparation for Imaging Vitreous Cells by Cryo-electron Tomography', *BIO-PROTOCOL*, 5(17). Available at: https://doi.org/10.21769/BioProtoc.1575.

Schaffer, M. *et al.* (2019) 'A cryo-FIB lift-out technique enables molecular-resolution cryo-ET within native Caenorhabditis elegans tissue', *Nature Methods*, 16(8), pp. 757–762. Available at: https://doi.org/10.1038/s41592-019-0497-5.

Schenk, A.D. *et al.* (2010) '3D Reconstruction from 2D Crystal Image and Diffraction Data', in *Methods in Enzymology*. Elsevier, pp. 101–129. Available at: https://doi.org/10.1016/S0076-6879(10)82004-X.

Schindelin, J. *et al.* (2012) 'Fiji: an open-source platform for biological-image analysis', *Nature Methods*, 9(7), pp. 676–682. Available at: https://doi.org/10.1038/nmeth.2019.

Schröder, M. and Kaufman, R.J. (2005) 'The Mammalian Unfolded Protein Response', *Annual Review of Biochemistry*, 74(1), pp. 739–789. Available at: https://doi.org/10.1146/annurev.biochem.73.011303.074134.

Schur, F.K.M. *et al.* (2015) 'The Structure of Immature Virus-Like Rous Sarcoma Virus Gag Particles Reveals a Structural Role for the p10 Domain in Assembly', *Journal of Virology*. Edited by W.I. Sundquist, 89(20), pp. 10294–10302. Available at: https://doi.org/10.1128/JVI.01502-15.

Schwabe, T., Srinivasan, K. and Rhinn, H. (2020) 'Shifting paradigms: The central role of microglia in Alzheimer's disease', *Neurobiology of Disease*, 143, p. 104962. Available at: https://doi.org/10.1016/j.nbd.2020.104962.

Scior, A. *et al.* (2018) 'Complete suppression of Htt fibrilization and disaggregation of Htt fibrils by a trimeric chaperone complex', *The EMBO Journal*, 37(2), pp. 282–299. Available at: https://doi.org/10.15252/embj.201797212.

Selkoe, D.J. (2008) 'Soluble oligomers of the amyloid ß-protein impair synaptic plasticity and behavior', *Behavioural Brain Research*, 192(1), pp. 106–113. Available at: https://doi.org/10.1016/j.bbr.2008.02.016.

Sexton, D.L. *et al.* (2022) 'Super-resolution confocal cryo-CLEM with cryo-FIB milling for in situ imaging of Deinococcus radiodurans', *Current Research in Structural Biology*, 4, pp. 1–9. Available at: https://doi.org/10.1016/j.crstbi.2021.12.001.

Shi, Y., Mosser, D.D. and Morimoto, R.I. (1998) 'Molecularchaperones as HSF1-specific transcriptional repressors', *Genes & Development*, 12(5), pp. 654–666. Available at: https://doi.org/10.1101/gad.12.5.654.

Shore, J. *et al.* (2023) 'Health economic analysis of the integrated cognitive assessment tool to aid dementia diagnosis in the United Kingdom', *Frontiers in Public Health*, 11, p. 1240901. Available at: https://doi.org/10.3389/fpubh.2023.1240901.

Shpigel, N. *et al.* (2019) 'Dietary restriction and gonadal signaling differentially regulate post-development quality control functions in *Caenorhabditis elegans*', *Aging Cell*, 18(2), p. e12891. Available at: https://doi.org/10.1111/acel.12891.

Sibert, B.S. *et al.* (2021) *Whole-cell cryo-electron tomography of cultured and primary eukaryotic cells on micropatterned TEM grids*. preprint. Cell Biology. Available at: https://doi.org/10.1101/2021.06.06.447251.

Sidrauski, C. and Walter, P. (1997) 'The Transmembrane Kinase Ire1p Is a Site-Specific Endonuclease That Initiates mRNA Splicing in the Unfolded Protein Response', *Cell*, 90(6), pp. 1031–1039. Available at: https://doi.org/10.1016/S0092-8674(00)80369-4.

Sinnige, T. *et al.* (2019) 'Expression of the amyloid-ß peptide in a single pair of C. elegans sensory neurons modulates the associated behavioural response', *PLOS ONE*. Edited by M.K. Lakshmana, 14(5), p. e0217746. Available at: https://doi.org/10.1371/journal.pone.0217746.

Sipe, J.D. and Cohen, A.S. (2000) 'Review: History of the Amyloid Fibril', *Journal of Structural Biology*, 130(2–3), pp. 88–98. Available at: https://doi.org/10.1006/jsbi.2000.4221.

Sollars, V. *et al.* (2003) 'Evidence for an epigenetic mechanism by which Hsp90 acts as a capacitor for morphological evolution', *Nature Genetics*, 33(1), pp. 70–74. Available at: https://doi.org/10.1038/ng1067.

Somogyvári, M., Gecse, E. and Sőti, C. (2018) 'DAF-21/Hsp90 is required for C. elegans longevity by ensuring DAF-16/FOXO isoform A function', *Scientific Reports*, 8(1), p. 12048. Available at: https://doi.org/10.1038/s41598-018-30592-6.

Somogyvári, M., Khatatneh, S. and Sőti, C. (2022) 'Hsp90: From Cellular to Organismal Proteostasis', *Cells*, 11(16), p. 2479. Available at: https://doi.org/10.3390/cells11162479.

St George-Hyslop, P.H. *et al.* (1987) 'The Genetic Defect Causing Familial Alzheimer's Disease Maps on Chromosome 21', *Science*, 235(4791), pp. 885–890. Available at: https://doi.org/10.1126/science.2880399.

Taipale, M., Jarosz, D.F. and Lindquist, S. (2010) 'HSP90 at the hub of protein homeostasis: emerging mechanistic insights', *Nature Reviews Molecular Cell Biology*, 11(7), pp. 515–528. Available at: https://doi.org/10.1038/nrm2918.

Taylor, R.C. (2016) 'Aging and the UPR(ER)', *Brain Research*, 1648, pp. 588–593. Available at: https://doi.org/10.1016/j.brainres.2016.04.017.

Teixeira-Castro, A. *et al.* (2011) 'Neuron-specific proteotoxicity of mutant ataxin-3 in C. elegans : rescue by the DAF-16 and HSF-1 pathways', *Human Molecular Genetics*, 20(15), pp. 2996–3009. Available at: https://doi.org/10.1093/hmg/ddr203.

Tepper, R.G. *et al.* (2013) 'PQM-1 Complements DAF-16 as a Key Transcriptional Regulator of DAF-2-Mediated Development and Longevity', *Cell*, 154(3), pp. 676–690. Available at: https://doi.org/10.1016/j.cell.2013.07.006.

Theer, P. *et al.* (2006) 'Two-photon Microscopy and Imaging', in R.A. Meyers (ed.) *Encyclopedia of Molecular Cell Biology and Molecular Medicine*. Weinheim, Germany: Wiley-VCH Verlag GmbH & Co. KGaA, p. mcb.200500019. Available at: https://doi.org/10.1002/3527600906.mcb.200500019.

Thompson, R.F. *et al.* (2016) 'An introduction to sample preparation and imaging by cryo-electron microscopy for structural biology', *Methods*, 100, pp. 3–15. Available at: https://doi.org/10.1016/j.ymeth.2016.02.017.

Tipping, K.W. *et al.* (2015) 'Amyloid Fibres: Inert End-Stage Aggregates or Key Players in Disease?', *Trends in Biochemical Sciences*, 40(12), pp. 719–727. Available at: https://doi.org/10.1016/j.tibs.2015.10.002.

Tittelmeier, J., Nachman, E. and Nussbaum-Krammer, C. (2020) 'Molecular Chaperones: A Double-Edged Sword in Neurodegenerative Diseases', *Frontiers in*

Aging Neuroscience, 12, p. 581374. Available at: https://doi.org/10.3389/fnagi.2020.581374.

Tong, Y.-G. and Bürglin, T.R. (2010) 'Conditions for dye-filling of sensory neurons in Caenorhabditis elegans', *Journal of Neuroscience Methods*, 188(1), pp. 58–61. Available at: https://doi.org/10.1016/j.jneumeth.2010.02.003.

Treusch, S. *et al.* (2011) 'Functional Links Between Aß Toxicity, Endocytic Trafficking, and Alzheimer's Disease Risk Factors in Yeast', *Science*, 334(6060), pp. 1241–1245. Available at: https://doi.org/10.1126/science.1213210.

Tyedmers, J., Mogk, A. and Bukau, B. (2010) 'Cellular strategies for controlling protein aggregation', *Nature Reviews Molecular Cell Biology*, 11(11), pp. 777–788. Available at: https://doi.org/10.1038/nrm2993.

Uno, M. *et al.* (2021) 'Neuronal DAF-16-to-intestinal DAF-16 communication underlies organismal lifespan extension in C. elegans', *iScience*, 24(7), p. 102706. Available at: https://doi.org/10.1016/j.isci.2021.102706.

Van Ham, T.J. *et al.* (2008) 'C. elegans Model Identifies Genetic Modifiers of α-Synuclein Inclusion Formation During Aging', *PLoS Genetics*. Edited by S.K. Kim, 4(3), p. e1000027. Available at: https://doi.org/10.1371/journal.pgen.1000027.

Vartiainen, S. *et al.* (2006) 'Identification of gene expression changes in transgenic C. elegans overexpressing human α-synuclein', *Neurobiology of Disease*, 22(3), pp. 477–486. Available at: https://doi.org/10.1016/j.nbd.2005.12.021.

Venugopal, P. *et al.* (2020) 'Multiple functions of the scaffold protein Discs large 5 in the control of growth, cell polarity and cell adhesion in Drosophila

melanogaster', *BMC Developmental Biology*, 20(1), p. 10. Available at: https://doi.org/10.1186/s12861-020-00218-0.

Virchow, R. (1854) 'Zur Cellulose —Frage', *Archiv für Pathologische Anatomie und Physiologie und für Klinische Medicin*, 6(3), pp. 416–426. Available at: https://doi.org/10.1007/BF02116546.

Walsh, J.D., Boivin, O. and Barr, M.M. (2020) 'What about the males? the *C. elegans* sexually dimorphic nervous system and a CRISPR-based tool to study males in a hermaphroditic species', *Journal of Neurogenetics*, 34(3–4), pp. 323–334. Available at: https://doi.org/10.1080/01677063.2020.1789978.

Wälti, M.A. *et al.* (2016) 'Atomic-resolution structure of a disease-relevant Aß(1–42) amyloid fibril', *Proceedings of the National Academy of Sciences*, 113(34). Available at: https://doi.org/10.1073/pnas.1600749113.

Wasmer, C. *et al.* (2008) 'Amyloid Fibrils of the HET-s(218–289) Prion Form a ß Solenoid with a Triangular Hydrophobic Core', *Science*, 319(5869), pp. 1523–1526. Available at: https://doi.org/10.1126/science.1151839.

Webb, R.H. (1996) 'Confocal optical microscopy', *Reports on Progress in Physics*, 59(3), pp. 427–471. Available at: https://doi.org/10.1088/0034-4885/59/3/003.

Wilkinson, M. *et al.* (2023) 'Disease-relevant ß2-microglobulin variants share a common amyloid fold', *Nature Communications*, 14(1), p. 1190. Available at: https://doi.org/10.1038/s41467-023-36791-8.

Williams, K.W. *et al.* (2014) 'Xbp1s in Pomc Neurons Connects ER Stress with Energy Balance and Glucose Homeostasis', *Cell Metabolism*, 20(3), pp. 471–482. Available at: https://doi.org/10.1016/j.cmet.2014.06.002.

Winston, W.M., Molodowitch, C. and Hunter, C.P. (2002) 'Systemic RNAi in *C. elegans* Requires the Putative Transmembrane Protein SID-1', *Science*, 295(5564), pp. 2456–2459. Available at: https://doi.org/10.1126/science.1068836.

Wisniewski, K.E. *et al.* (1985) 'Alzheimer's disease in Down's syndrome: Clinicopathologic studies', *Neurology*, 35(7), pp. 957–957. Available at: https://doi.org/10.1212/WNL.35.7.957.

Wu, C. (1995) 'Heat Shock Transcription Factors: Structure and Regulation', *Annual Review of Cell and Developmental Biology*, 11(1), pp. 441–469. Available at: https://doi.org/10.1146/annurev.cb.11.110195.002301.

Wu, Y. *et al.* (2006) 'Amyloid-ß-Induced Pathological Behaviors Are Suppressed by *Ginkgo biloba* Extract EGb 761 and Ginkgolides in Transgenic *Caenorhabditis elegans*', *The Journal of Neuroscience*, 26(50), pp. 13102–13113. Available at: https://doi.org/10.1523/JNEUROSCI.3448-06.2006.

Wu, Y. *et al.* (2010) 'Heat shock treatment reduces beta amyloid toxicity in vivo by diminishing oligomers', *Neurobiology of Aging*, 31(6), pp. 1055–1058. Available at: https://doi.org/10.1016/j.neurobiolaging.2008.07.013.

Xu, Y.-M. *et al.* (2012) 'Post-Translational Modification of Human Heat Shock Factors and Their Functions: A Recent Update by Proteomic Approach', *Journal of Proteome Research*, 11(5), pp. 2625–2634. Available at: https://doi.org/10.1021/pr201151a.

Yahara, I. (1999) 'The role of HSP90 in evolution: HSP90 in evolution', *Genes to Cells*, 4(7), pp. 375–379. Available at: https://doi.org/10.1046/j.1365-2443.1999.00271.x.

Yamamoto, M. *et al.* (2005) 'Regulation of Oxidative Stress by the Anti-aging Hormone Klotho', *Journal of Biological Chemistry*, 280(45), pp. 38029–38034. Available at: https://doi.org/10.1074/jbc.M509039200.

Yang, Y. *et al.* (2022) 'Cryo-EM structures of amyloid-ß 42 filaments from human brains', *Science*, 375(6577), pp. 167–172. Available at: https://doi.org/10.1126/science.abm7285.

Young, L.J., Kaminski Schierle, G.S. and Kaminski, C.F. (2017) 'Imaging Aß(1–42) fibril elongation reveals strongly polarised growth and growth incompetent states', *Phys. Chem. Chem. Phys.*, 19(41), pp. 27987–27996. Available at: https://doi.org/10.1039/C7CP03412A.

Younkin, S.G. (1995) 'Evidence that A?42 is the real culprit in alzheimer's disease', *Annals of Neurology*, 37(3), pp. 287–288. Available at: https://doi.org/10.1002/ana.410370303.

Zhang, P. *et al.* (2013) 'Direct and Indirect Gene Regulation by a Life-Extending FOXO Protein in C. elegans: Roles for GATA Factors and Lipid Gene Regulators', *Cell Metabolism*, 17(1), pp. 85–100. Available at: https://doi.org/10.1016/j.cmet.2012.12.013.

Zhang, S. *et al.* (2020) 'Caenorhabditis elegans as a Useful Model for Studying Aging Mutations', *Frontiers in Endocrinology*, 11, p. 554994. Available at: https://doi.org/10.3389/fendo.2020.554994.

Zhang, X. *et al.* (2008) 'Near-atomic resolution using electron cryomicroscopy and single-particle reconstruction', *Proceedings of the National Academy of Sciences*, 105(6), pp. 1867–1872. Available at: https://doi.org/10.1073/pnas.0711623105.

Zheng, S. *et al.* (2022) 'AreTomo: An integrated software package for automated marker-free, motion-corrected cryo-electron tomographic alignment and reconstruction', *Journal of Structural Biology: X*, 6, p. 100068. Available at: https://doi.org/10.1016/j.yjsbx.2022.100068.

Zheng, S.Q. *et al.* (2017) 'MotionCor2: anisotropic correction of beam-induced motion for improved cryo-electron microscopy', *Nature Methods*, 14(4), pp. 331–332. Available at: https://doi.org/10.1038/nmeth.4193.

Zhu, J., Shang, Y. and Zhang, M. (2016) 'Mechanistic basis of MAGUK-organized complexes in synaptic development and signalling', *Nature Reviews Neuroscience*, 17(4), pp. 209–223. Available at: https://doi.org/10.1038/nrn.2016.18.

Zou, J. *et al.* (1998) 'Repression of Heat Shock Transcription Factor HSF1 Activation by HSP90 (HSP90 Complex) that Forms a Stress-Sensitive Complex with HSF1', *Cell*, 94(4), pp. 471–480. Available at: https://doi.org/10.1016/S0092-8674(00)81588-3.